Development, Characterization and Application of a novel X-ray Imaging Laboratory

Zur Erlangung des akademischen Grades eines
Doktors der Naturwissenschaften (Dr. rer. nat.)
von der KIT-Fakultät für Physik des Karlsruher Instituts für Technologie (KIT)
genehmigte
Dissertation
von
M. Sc. Marcus Zuber
geboren in Heidelberg

Referent: Prof. Dr. Tilo Baumbach
Korreferent: Prof. Dr. Michael Fiederle

Tag der mündlichen Prüfung: 16.12.2022

Abstract

A versatile X-ray imaging laboratory is build up at the Institute for Photon Science and Synchrotron Radiation (CL/CT-Laboratory) with the aim to be a modular platform for method development, the characterization of components for X-ray imaging, evaluation of existing methods and optimization of methods for specific tasks.

In the frame of this work the CL/CT-Laboratory has been commissioned, multiple components were characterized with the focus on novel photon counting detectors, and a diverse set of X-ray imaging methods were implemented and applied. With these detectors and the laboratories features I examined the limitations of existing imaging methods. I optimized X-ray imaging methods for certain tasks and also used the unique features of the laboratory to develop new imaging methods.

The laboratory is organized in a modular design (in hard and software) enabling possibilities to realize versatile setups in a reproducible and easy way.

After I established the CL/CT-Laboratory as a versatile framework for X-ray imaging, I employed its features by optimizing the setup for various scientific fields, where X-ray imaging enabled new insights.

Zusammenfassung

Am Institut für Photonenforschung und Synchrotronstrahlung wurde ein vielseitiges Labor für Bildgebungsmethoden mit Röntgenstrahlung aufgebaut (CL/CT-Laboratorium). Ziel dabei war es eine modulare Platform für Methodenentwicklung, Komponentencharakterisierung für verschiedene Röntgenbildgebungsverfahren, Untersuchungen von verschiedenen etablierten Methoden und die Optimierung von Methoden für spezifische Anwendungsfälle zu entwickeln.

Im Rahmen dieser Arbeit wurde das CL/CT-Laboratorium in Betrieb genommen, eine Vielzahl an Komponenten, mit dem Fokus auf energieselektiven photonenzählenden Detektoren, wurden charakterisiert und Bildgebungsmethoden implementiert und angewendet. Mit Hilfe der neuartigen Detektoren und der einzigartigen Möglichkeiten des Labors wurden bestehende Bildgebungsmethoden auf deren Anwendbarkeit und deren Limitierungen untersucht. Verschiedene Röntgenbildgebungsmethoden wurden für spezielle Anwendungen optimiert und neuartige Methoden wurden entwickelt.

Das Labor ist modular (in Hard- und Software) konzipiert um vielfältige Aufbauten in einfacher und wiederholbarer Form zu realisieren.

Nachdem ich das CL/CT-Laboratorium als Framework für Röntgenbildgebung aufgebaut habe, habe ich es für vielfältige Anwendungen aus verschiedenen Wissenschaftsgebieten erfolgreich angewendet.

Contents

1. Introduction

In the frame of this work I commissioned a modular and flexible X-ray imaging platform, implemented established as well as new imaging methods and evaluated the performance of the system with multiple application examples. New detector systems, featuring not only a high spatial resolution but also giving the possibility to measure the X-ray energy spectrum are promising to extend the possibilities of X-ray imaging. Therefore, I performed a detailed characterization of the new detector systems with the focus on spectroscopic X-ray imaging.

Directly after its discovery X-ray were used in medical application. Over the time, they also became more and more popular in many other scientific fields and technologies. With these methods, scientific questions from many fields, like biology, material science, cultural heritage can be addressed. Since imaging objects in 3D (or 2D projection) does not significantly influence the sample, this even allows in-situ or operando experiments.

While the use of the X-ray attenuation was mostly used in the first hundred years after the discovery, new detector system allow to measure the spectral composition of the incoming beam. This enables to measure the energy dependent attenuation coefficients of a volumetric sample (without destroying it) to get a deeper knowledge of the internal composition and even material concentrations and distribution can be extracted from the recorded data.

For typical sample materials, the difference of the refractive index compared to air and vacuum is tiny for X-rays, compared to visible light. This results in tiny angles for refractive and interference effects of X-rays with matter. However, technological developments of different X-ray detectors, sources, optics and mechanics made it possible in the last decades to measure not only the X-ray attenuation, but also the refraction, scattering and interference.

For any imaging experiment many components are contributing to the imaging process. The source, the detector, possible optics and the positioning of the sample and the other objects play an important role.

With the aim to develop new imaging methods, to optimize and to translate existing methods from other fields (like synchrotron X-ray imaging) to more available laboratory source, a laboratory at the Institute for Photon Science and Synchrotron Radiation (IPS) has been set up (CL/CT-Laboratory). The laboratory is designed and structured in a way to be as flexible, modular and broad in its parameter space as possible. This work aims to establish a powerful tool to test, verify, characterize different components for X-ray imaging as well as to implement and test full new imaging methods. The complete setup is custom-made for its task and all the different componentes where included by me into a versatile framework for X-ray imaging.

Well established methods like computed tomography were implemented (and op-

timized) to compare new methods with the established ones as well as allowing to extend the existing ones.

All these implementations, and the overall design in general, is intended to be as modular and extendable (in hard and software) to realize a test bed for application tests, method development and characterization of new X-ray imaging methods.

While many X-ray imaging systems, optimized for specific tasks, methods or applications are established and available (e.g. [XXLCT; But+09; Bir+16; SKY]) I did not find any imaging system covering such a large range of methods, applications and parameters.

Starting from acceptance tests of the mechanical system over implementing different subcomponents in the framework of a control system I finally established a complete, versatile and modular imaging system.

1.1. Structure of this Work

In chapter 2 the technical features and requirements of the laboratory setup are described and compared to other systems. A publication about these features and the laboratories capabilities is currently under preparation.

Chapter 3 features a detailed characterization of different types of energy sensitive imaging detectors, that can be employed for spectroscopic imaging in 2D and 3D. These detectors allow counting only photons with certain energy criteria which can be used to examine the energy dependence of the attenuation coefficient.

How the different interactions of the samples with the X-rays form an image is shown in chapter 4. This also includes examinations about the creation of the different contrasts using refraction, scatter and interference.

In chapter 5 I will move from single projection imaging in 2D to the methods, allowing to get three-dimensional data. Different, well established, methods are described there and my implementations in the laboratory are demonstrated. Also, a new method, called *augmented laminography*, that allows to fuse data from two different methods and combining the benefits from both is introduced there as an example to implement and test new methods with this setup.

In the last chapter, different application examples from various scientific fields are shown in the chapter 6 to demonstrate how I applied and optimized the unique features of the CL/CT-Laboratory.

1.2. Publications Related to this Thesis

1.2.1. Published parts of this thesis

The following publications feature parts of this thesis.

[Koe+14a] T. Koenig, M. Zuber, E. Hamann, A. Cecilia, R. Ballabriga, M. Campbell, M. Ruat, L. Tlustos, A. Fauler, M. Fiederle, and T. Baumbach. “How spectroscopic x-ray imaging benefits from inter-pixel communication”. In: *Phys. Med. Biol.* 59.20 (Oct. 21, 2014), p. 6195.

[Koe+14b] T. Koenig, M. Zuber, E. Hamann, A. Runz, M. Fiederle, and T. Baumbach. "Pooling optimal combinations of energy thresholds in spectroscopic CT". In: *SPIE Medical Imaging*. Vol. 9033. 2014, 90331A–90331A–12.

[Zub+14] M. Zuber, T. Koenig, E. Hamann, A. Cecilia, M. Fiederle, and T. Baumbach. "Characterization of a 2x3 Timepix assembly with a 500 µm thick silicon sensor". In: *J. Inst.* 9.5 (2014), p. C05037.

[Tri+15] B. Trimborn, P. Meyer, D. Kunka, M. Zuber, F. Albrecht, S. Kreuer, T. Volk, T. Baumbach, and T. Koenig. "Imaging properties of high aspect ratio absorption gratings for use in preclinical x-ray grating interferometry". In: *Physics in Medicine & Biology* 61.2 (2015), p. 527.

[Zub+15a] M. Zuber, E. Hamann, R. Ballabriga, M. Campbell, M. Fiederle, T. Baumbach, and T. Koenig. "An investigation into the temporal stability of CdTe-based photon counting detectors during spectral micro-CT acquisitions". In: *Biomedical Physics & Engineering Express* 1.2 (2015), p. 025205.

[Zub+15b] M. Zuber, T. Koenig, R. Hussain, E. Hamann, R. Ballabriga, M. Campbell, A. Fauler, M. Fiederle, and T. Baumbach. "Reducing the formation of image artifacts during spectroscopic micro-CT acquisitions". In: *SPIE Medical Imaging*. International Society for Optics and Photonics, 2015, pp. 94124X–94124X.

[Bal+16] R. Ballabriga, J. Alozy, M. Campbell, E. Frojdh, E. Heijne, T. Koenig, X. Llopart, J. Marchal, D. Pennicard, T. Poikela, L. Tlustos, P. Valerio, W. Wong, and M. Zuber. "Review of hybrid pixel detector readout ASICs for spectroscopic X-ray imaging". In: *Journal of Instrumentation* 11.01 (2016), P01007.

[Koe+16] T. Koenig, M. Zuber, B. Trimborn, T. Farago, P. Meyer, D. Kunka, F. Albrecht, S. Kreuer, T. Volk, M. Fiederle, et al. "On the origin and nature of the grating interferometric dark-field contrast obtained with low-brilliance x-ray sources". In: *Physics in medicine and biology* 61.9 (2016), p. 3427.

[Zub+17] M. Zuber, M. Laaß, E. Hamann, S. Kretschmer, N. Hauschke, T. Van De Kamp, T. Baumbach, and T. Koenig. "Augmented laminography, a correlative 3D imaging method for revealing the inner structure of compressed fossils". In: *Scientific reports* 7.1 (2017), pp. 1–11.

[Far+22] T. Faragó, S. Gasilov, I. Emslie, M. Zuber, L. Helfen, M. Vogelgesang, and T. Baumbach. "Tofu: a fast, versatile and user-friendly image processing toolkit for computed tomography". In: *Journal of Synchrotron Radiation* 29.3 (2022).

1.2.2. Publications Enabled by the Presented Work

In the following publications the here presented setup was used to investigate different topics, but the findings are not presented within this thesis.

[Bro+14] A. S. Brogna, M. Balzer, S. Smale, J. Hartmann, D. Bormann, E. Hamann, A. Cecilia, M. Zuber, T. Koenig, A. Zwerger, et al. "A fast embedded readout system for large-area Medipix and Timepix systems". In: *J. Inst.* 9.5 (2014), p. C05047.

[Sch+17a] T. J. Schröter, F. Koch, P. Meyer, M. Baumann, D. Münch, D. Kunka, S. Engelhardt, M. Zuber, T. Baumbach, and J. Mohr. "Large area gratings by x-ray LIGA dynamic exposure for x-ray phase-contrast imaging". In: *Journal of Micro/Nanolithography, MEMS, and MOEMS* 16.1 (2017), p. 013501.

[Sch+17b] T. J. Schröter, F. J. Koch, D. Kunka, P. Meyer, S. Tietze, S. Engelhardt, M. Zuber, T. Baumbach, K. Willer, L. Birnbacher, et al. "Large-area full field x-ray differential phase-contrast imaging using 2D tiled gratings". In: *Journal of Physics D: Applied Physics* 50.22 (2017), p. 225401.

[Dzi+19] M. Dziadek, R. Kudlackova, A. Zima, A. Slosarczyk, M. Ziabka, P. Jelen, S. Shkarina, A. Cecilia, M. Zuber, T. Baumbach, et al. "Novel multicomponent organic–inorganic WPI/gelatin/CaP hydrogel composites for bone tissue engineering". In: *Journal of Biomedical Materials Research Part A* 107.11 (2019), pp. 2479–2491.

[Sie+19a] T. Siebert, M. Zuber, S. Engelhardt, T. Baumbach, H. P. Karbstein, and V. Gaukel. "Visualization of crust formation during hot-air-drying via micro-CT". In: *Drying Technology* 37.15 (2019), pp. 1881–1890.

[Sie+19b] T. Siebert, M. Zuber, E. Hamann, T. Baumbach, H. P. Karbstein, and V. Gaukel. "Micro-CT visualization of structure development during freeze-drying processes". In: *Drying Technology* (2019).

[Zak+19] M. Zakharova, S. Reich, A. Mikhaylov, V. Vlnieska, M. Zuber, S. Engelhardt, T. Baumbach, and D. Kunka. "A comparison of customized Hartmann and newly introduced inverted Hartmann masks for single-shot phase-contrast X-ray imaging". In: *EUV and X-ray Optics: Synergy between Laboratory and Space VI*. Vol. 11032. International Society for Optics and Photonics. 2019, 110320U.

[Mes+20a] H. Mescher, F. Schackmar, H. Eggers, T. Abzieher, M. Zuber, E. Hamann, T. Baumbach, B. S. Richards, G. Hernandez-Sosa, U. W. Paetzold, et al. "Flexible inkjet-printed triple cation perovskite X-ray detectors". In: *ACS applied materials & interfaces* 12.13 (2020), pp. 15774–15784.

[Mes+20b] H. Mescher, F. Schackmar, H. Eggers, T. Abzieher, M. Zuber, E. Hamann, T. Baumbach, B. S. Richards, G. Hernandez-Sosa, U. W. Paetzold, et al. "Inkjet-printed triple cation perovskite absorbers for mechanically flexible high performance X-ray detectors". In: *Hard X-Ray, Gamma-Ray, and Neutron Detector Physics XXII*. Vol. 11494. SPIE. 2020, 114940A.

[Pog+20] P. Pogoda, M. Zuber, T. Baumbach, R. R. Schoch, and A. Kupfer. "Cranial shape evolution of extant and fossil crocodile newts and its relation to reproduction and ecology". In: *Journal of Anatomy* (2020).

[Sie+20] T. Siebert, A. Becker, M. Bunzel, M. Zuber, E. Hamann, T. Baumbach, H. P. Karbstein, and V. Gaukel. "Evaluation of the usefulness of serial combination processes for drying of apples". In: *Drying Technology* 38.10 (2020), pp. 1274–1290.

[Pog+21] P. Pogoda, M. Zuber, T. Baumbach, and A. Kupfer. "Clasp and dance: Mating mode promotes variable sexual size and shape dimorphism trajectories in crocodile newts (Caudata: Salamandridae)". In: *Authorea Preprints* (2021).

[Mes+22] H. Mescher, F. Schackmar, R. Huber, H. Eggers, M. Zuber, E. Hamann, G. Gramlich, J. Dangelmaier, Q. Zhang, A. Rösch, et al. "Folded perovskite X-ray detector with high sensitivity and high spatial resolution". In: *Hard X-Ray, Gamma-Ray, and Neutron Detector Physics XXIV*. SPIE. 2022, PC122410F.

[Mik+22] A. Mikhaylov, M. Zakharova, V. Vlnieska, A. Khanda, S. Bremer, M. Zuber, S. H. Pezzin, and D. Kunka. "Inverted Hartmann mask made by deep X-ray lithography for single-shot multi-contrast X-ray imaging with laboratory setup". In: *Optics Express* 30.6 (2022), pp. 8494–8509.

2. The novel 3D X-ray Imaging Laboratory at IPS

With in this work a novel X-ray imaging laboratory has been set up at the IPS. The main purpose of this setup is to have a sophisticated system, allowing developing new methods for X-ray imaging, evaluating current and new methods, optimizing existing methods for specific applications, transferring methods from synchrotron X-ray imaging and characterizing components for X-ray imaging applications. The wide parameter space, that can be realized in the laboratory allows optimizing and 'simulate' imaging modalities for other systems with a more dedicated task.

The setup consists of different components, grouped to submodules. Each of the sub-mudules contributes to the imaging process in a different way. Each of them can be configured in multiple ways, allowing to realize a wide range of imaging modalities. In this part I will describe these single components, their main features and the resulting possibilities for the employment in different X-ray methods.

A typical X-ray imaging setup consists of an X-ray tube, that generates a polychromatic spectrum of X-rays, a detector for X-rays and a positioning system, that defines the geometry between the relevant components. In addition, also optical elements can be part of the system.

In a system for pure attenuation projection measurements, typically a 2D flat panel detector is employed, resulting in pixel-wise attenuation measurements. When moving to 3D imaging, projections of the sample from different sample orientations need to be acquired and afterwards the 3D volume reconstructed. For the well known computed tomography case, the sample rotates around an axis of rotation perpendicular to the main beam direction and parallel to the detector plane and projections are sampled over a sufficient angular range (see section 5.1). This geometry can be generalized to computed laminography (see section 5.2), where the axis of rotation can be placed also inclined with respect to the beam direction. This can be beneficial especially for flat laterally extended specimens.

When moving from pure attenuation measurements to examining the complete refractive index of a specimen, special features for the source are required or optical elements are needed, that allow precise measurements of the local deflection of the beam.

For all the employed components the geometrical positioning accuracy and repeatability is important. A wrong position of a component directly results in a displaced measurement or, in case, when multiple measurements are processed lead to a loss of resolution or artefacts in the resulting processed data.

X-ray sources X-ray tubes create X-rays from accelerated electrons that are decelerated on a solid or liquid target material. In the deceleration process the kinetic energy is creates X-ray photons due to the Bremsstrahlung effect (see section 2.2).

The spectrum of the X-ray source is mostly defined by the acceleration voltage or the kinetic energy of the electrons. Typically, an X-ray tube features voltages up to approximately 200 keV with one high voltage generator, or up to approximately 400 keV with two generators for newer X-ray tubes. For higher energies linear accelerators can be employed, resulting in energies up to a few MeV.

In addition to the continuous polychromatic spectrum, the used target material introduces characteristic lines from fluorescences. The most common target material is tungsten, that features a high melting temperature and good thermal conductivity, which is required for handling the created heat in the target.

The effective size of the source is defined by the area of the target, onto which the electron beam is focused and the minimal size is given by the thermal properties of the target material and the focusing mechanisms.

X-ray detectors The most obvious parameters of an X-ray imaging detector are the pixel size and the number of pixels.

Typical X-ray detectors (so-called flat panel detectors) feature a scintillating layer, that converts X-rays to visible light, and a detection system for the visible light. In the most cases these are CCD or CMOS sensor directly coupled to the scintillator. While the noise is given by the employed CCD or CMOS, the scintillator defines the efficiency (spectrum dependent attenuation) and spatial resolution (due to the spread of the visible light into multiple readout pixels).

Another approach to detect X-rays are so-called direct converting X-ray detectors. These utilize a semiconductor layer and measure the created free charge, that is created by the X-ray interaction with the sensor layer. A readout can integrate the amount of free charge or count the number of current pulses. In the latter case, the detectors are single photon counting detectors (see section 2.3.4 and chapter 3). By introducing a threshold to the amount of charge of a single interaction, the detectors can be energy selective.

Stability For the most components one can assume, that a positioning accuracy and repeatability similar to the effective (magnified) pixel size and source size. For the projection of a point of the sample should be significantly more stable than a pixel pitch. This is also valid for nested geometrical parameters like how a rotation axis is located (and stable). When optical elements are introduced, these requirements become stricter. For an X-ray grating with small feature sizes must be stable in the magnitude order of its feature size.

(Projection) Geometry For all imaging applications the relative position of the source, the specimen the detector, and maybe optical elements are crucial for the resulting image (that is formed by the line integral along the X-rays). In addition, the projections need to be performed while scanning one or multiple of the motorized axes (e.g. rotation of the sample for CT). With the aim of high flexibility of the system, degrees of freedom are over determined, allowing multiple position implementations with the same resulting projection geometry, which can be an issue with fragile specimen that can not be positioned in arbitrary orientations. In this case the inclinations can be done by other degrees of freedom.

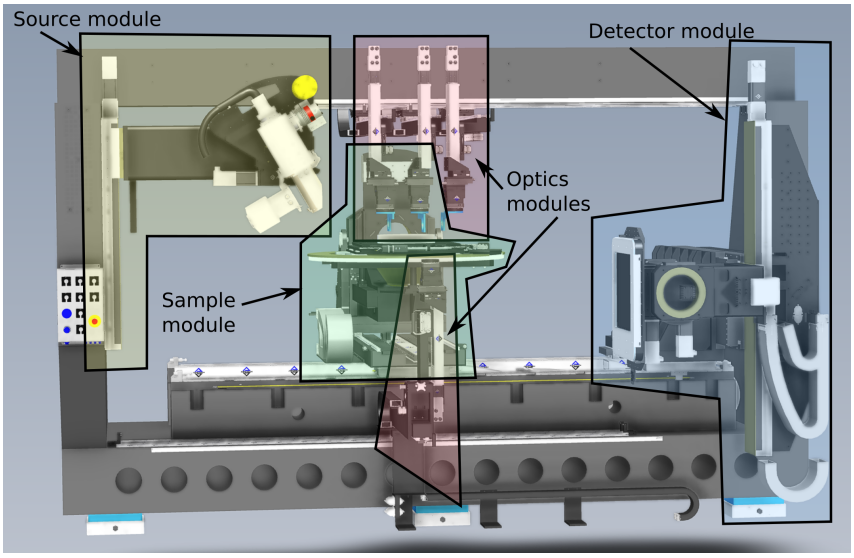

Figure 2.1.: Overview of the different modules of the CL/CT-Laboratory.

2.1. Overview of the CL/CT-Laboratory

The initial concept of the laboratory was created within the IPS imaging group. I implemented the different components of the system to build a complete framework for X-ray imaging.

Many new developments in the field of X-ray imaging lead to the idea of a dedicated laboratory for development of new methods in X-ary imaging at the IPS . The laboratory should be as flexible as possible to allow the implementation of as many methods as possible. Therefore, a complex mechanical manipulator for the positioning of different detectors, sources, samples and optical elements was designed.

The complete laboratory was designed in a modular way and all the components are embedded in a mechanical manipulator. The different components can be grouped into a source module, featuring a modular X-ray tube that can be moved in two degrees of freedom, a detector module with multiple detectors (indirect and direct converting) with a total of three translation and two rotational degrees of freedoms and a complex sample positioning system for sample alignment and arbitrary projection geometries. In addition, four completely independent sets of optical components (like X-ray gratings) can be mounted in the beam path. The mountings feature six motorized degrees of freedom for alignment.

Everything is implemented in an as much as possible generalized imaging setup, where the different components are chosen to be modular, exchangeable and feature a deep level of control. Such a setup can be used for developing and evaluating new X-ray imaging methods, to characterize components employed for imaging applications as well as to perform application tests.

The system was designed to be suitable for Computed Tomography, Computed Laminography and grating interferometry. However, it was intended to not lose any generality of the whole system.

The mechanical system is mostly consisting of the mechanical positioners for the X-ray tubes, one positioner for the detectors, four positioners for optical elements

as gratings, and different possible sample positioners. All mechanical elements are completely controllable over our in-house developed control system. It is possible on all motors (except one piezo stage for stepping of optical elements) to issue either motions with a fixed velocity (continuous motion) or to issue a move to a target position. The controller features multiple parameters and state values of the motors, allowing reading if the target position or velocity is reached as well the measured values of the current position and velocity. All motors are operated in closed loop feedback to automatically compensate for any drifts. In the case of any unexpected faults on the hardware, all participating motors are disabled and the state and error message are passed to the control system.

For safety reasons all vertical axes and the large sample pitch axes are equipped with brakes, that are activated by the control system or in case of an emergency stop or power failure. Also, all motions can be stopped by an emergency stop and all axes without breaks are free to move manually.

The given precisions are the bidirectional repeatability, measured by the manufacturer (Aerotech GmbH[1]) of the mechanical system. The measured accuracy is in the same order of magnitude. However, in the most times, the repeatability is more important than the accuracy of a motion. The off-axis deviations were also measured. The reproducible deviations are learned by the controller of the mechanical manipulator and the corresponding perpendicular motors are able to compensate for these errors.

The repeatability is the deviation, when a positioning system tries to reach the same point. It is called bidirectional, when the point is reached from both directions. The accuracy is the error of the position relative to a global measure of the position. The off-axis deviation is the amount a positioning system moves in a direction perpendicular to its intended motion direction.

The large granite block and the damping feet provide a sufficient damping against external vibrations onto the system.

The whole experimental setup is housed in an accessible radiation protection hutch, fulfilling all required radiation protection rules. The whole setup can be controlled from a working area outside the radiation protection. The ambient temperature within the experimental hutch is stabilized to 1 K, to prevent instabilities due to thermal expansions. A wide range of infrastructure (like power sockets, network connections, water cooling and the availability of multiple gases) is present all in the laboratory.

A sketch of the overall system is shown in figure 2.1. The different main parts are grouped in the source module (highlighted in orange), detector module (blue), sample module (green), optics modules (purple). These submodules are described in detail in the next sections.

The coordinate system for all further descriptions is defined as the beam direction y, the direction upwards to be z and horizontal direction perpendicular to the beam x. The rotation are called pitch around x, roll around y and yaw around z.

[1] https://de.aerotech.com

2.2. X-ray Source Module

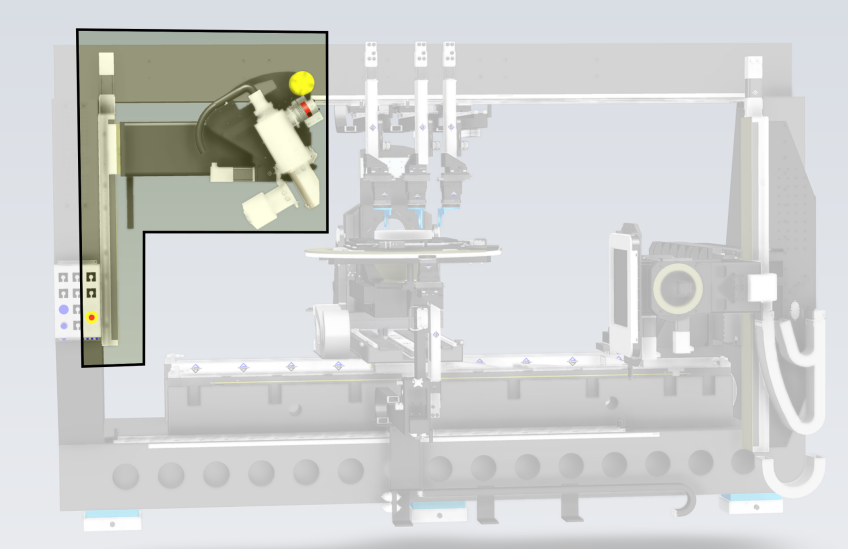

Figure 2.2.: Source module of the imaging setup, featuring the two X-ray tube configurations and the mechanical alignment degrees-of-freedom (DOF) for the X-ray tube.

The source module incorporates the X-ray source (with its different configurations as described below) and the motorized alignment axes. It allows to adjust the height of the source as well as to tilt the source to achieve an inclined optical axis within the system (in particular for laminographic imaging geometries, see section 5.2). The main direction of the X-ray beam can be adjusted from horizontal to directly pointing downwards.

The X-ray source is a custom modified X-Ray WorX, consisting of two different tube heads. The ability to exchange the tube head allows to use two different X-ray target geometries described below.

While the controller of the X-ray tube performs many automatized calibration and alignment procedures, all parameters like heating current and the currents of the focusing and steering coils are exposed via the control system for the experiment. This allows many possibilities like intentionally enlarging the focal spot size or moving the source position on a trajectory on the target.

2.2.1. Mechanical Alignment

The motorized degrees of freedom for alignment of the X-ray source submodule are shown in figure 2.3. With this mechanical module the X-ray tube can be adjusted in the height (SZ1) and can be rotated in the pitch direction (SP1). The height adjustment is required to choose the exposed vertical position of the sample and to sample different height positions of a sample. The pitch adjustment is to align the orientation of the optical axis and to correct for the different orientations of the X-ray tube head. Since one of the tube heads is a reflection geometry and the other one a transmission geometry, the tube needs to be rotated by 60° to maintain a

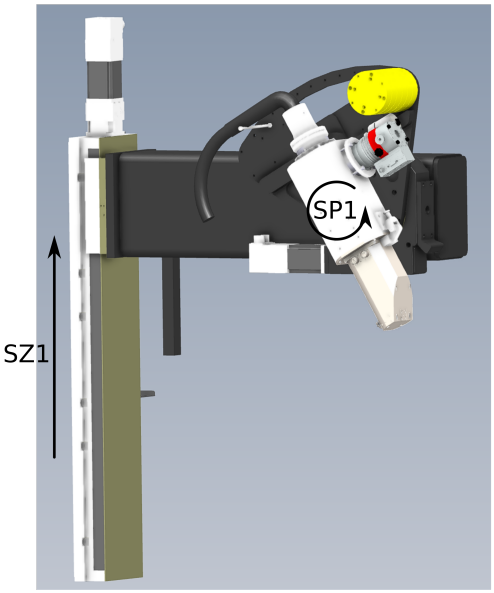

Figure 2.3.: Outline of the alignment motors for the source manipulation submodule. Here the direct tube head is mounted.

Table 2.1.: Degrees of freedom for the source positioning

DOF	x	y	z	pitch	roll	yaw
axis name	-	-	SZ1	SP1	-	-
travel	-	-	900 mm	150°	-	-
precision	-	-	1.1 µm	20.5″	-	-

horizontal orientation main beam direction.

To allow operating the tube in a down faced orientation, the tube is mounted on a long lever. This gives the possibility to put the sample stage and the detector below the X-ray source (see laminography in section 5.2) and to rotate the source in a way that the beak is pointing downwards.

In addition, the possibility of positioning the X-ray tube in arbitrary positions helps a lot fot the exchange of the tube heads and for maintenance of the X-ray tube.

The degrees of freedom and the corresponding accuracies are shown in table 2.1.

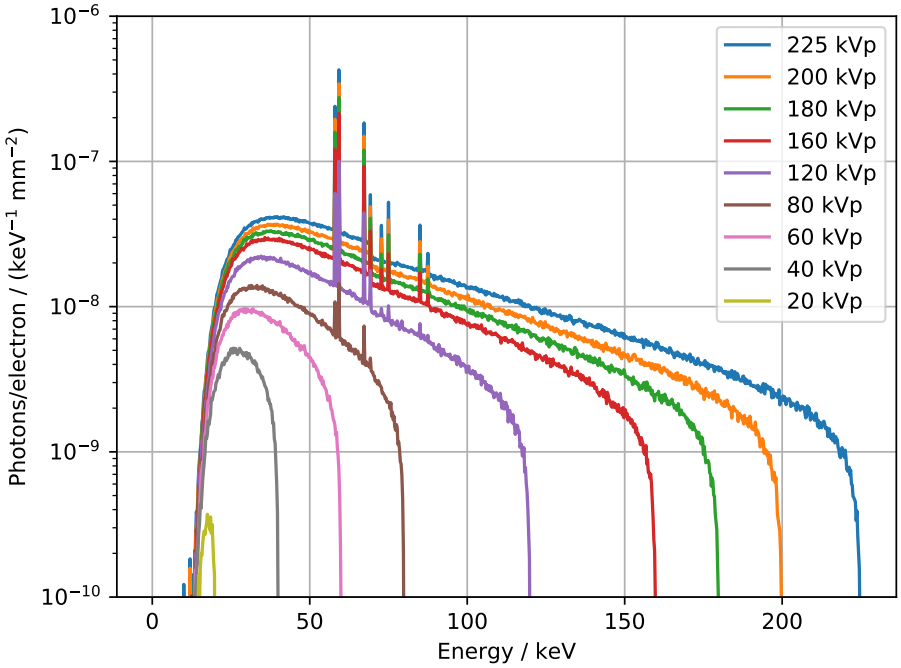

Figure 2.4.: Spectrum of the direct tube head for different acceleration voltages. The spectra are normalized to one electron of the electron beam. The spectra are sampled 1 m after the X-ray tube.

2.2.2. Direct Target Configuration

In this X-ray tube configuration, the electron beam is steered onto a solid, water cooled, tungsten target. The surface is inclined, resulting in a classical reflection geometry. The beam is collimated to an opening angle of 30°, featuring a homogeneous intensity within this region. The source size varies from 7 µm to 200 µm, depending on the impinging power on the target. The acceleration voltage can be set from 20 keV to 225 keV. Spectra of the different acceleration voltages without any additional external filters are shown in figure 2.4. The spectra are Monte-Carlo simulated with BEAMnrc [KRW04].

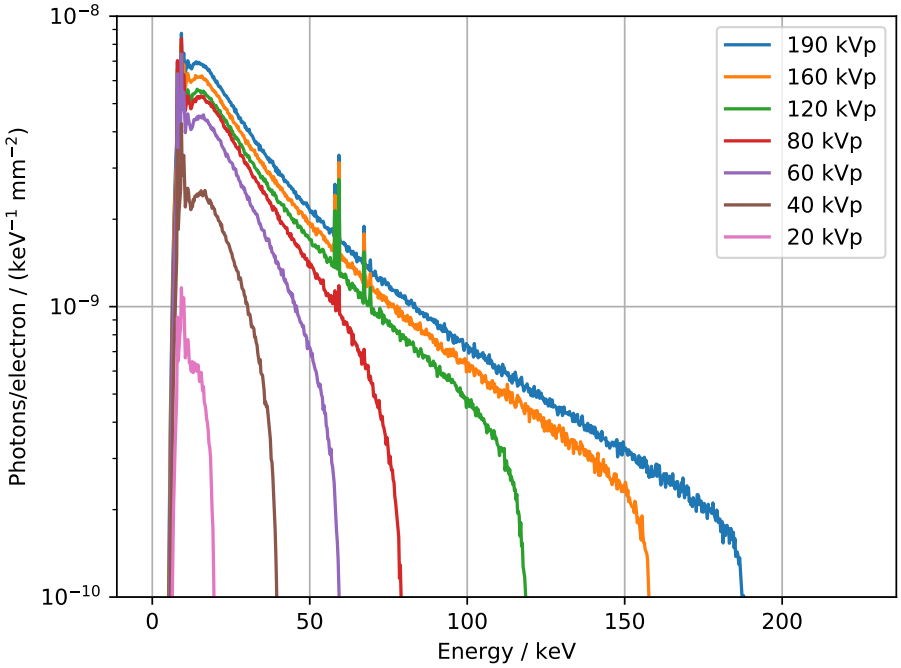

Figure 2.5.: Spectra of the transmission tube head for different acceleration voltages. The spectra are normalized to one electron of the electron beam. The spectra are sampled 1 m after the X-ray tube.

2.2.3. Transmission Target Configuration

In the second possible setting, the electron beam hits the target perpendicular with respect to its surface. The target is composed of a thin diamond substrate with a thin layer of tungsten. The X-rays are mostly leaving the target in the same direction the electron beam was headed. The mounting of the substrate is cooled, allowing a high power while keeping the source spot stable and small. With this target spot sizes below 0.8 µm are feasible. The substrate also acts as the exit window. Therefore, the spectrum is not filtered by any additional exit window, allowing a very soft xray spectrum. Spectra, without any additional filters, are shown in the figures 2.5. The spectra are Monte-Carlo simulated with BEAMnrc [KRW04].

Internally two sets of focusing and alignment coils (x and y direction) are located. These can be used to focus and center the point on the target, that is hit by the electron beam. The possibility to adjust these online is used in section 5.7. Internal water cooling helps to stabilize the temperature of those devices.

2.3. Detector Module

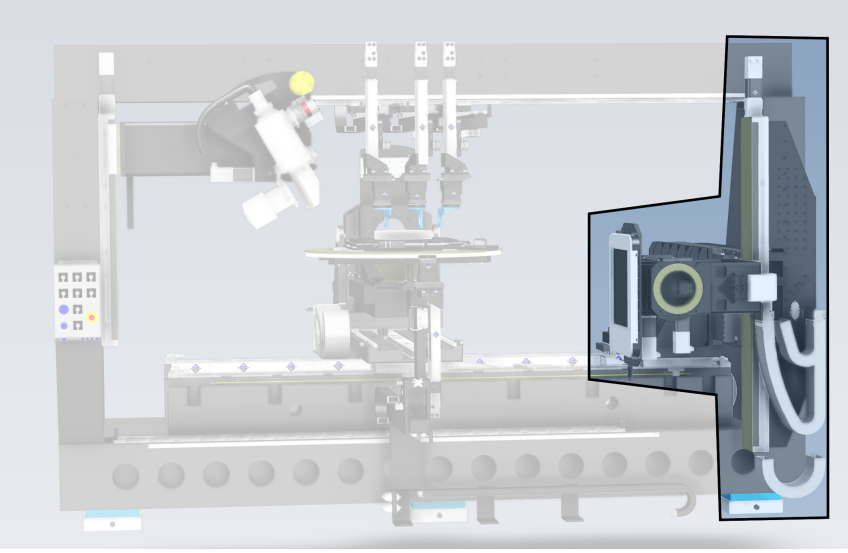

Figure 2.6.: Detector module of the CL/CT-Laboratory

The detector module can be equipped with multiple detectors and allows to position the detector precisely. The detector can be translated in all three degrees of freedom and can be rotated around two degrees of freedom. On the module power connections and different network connections are present (moving along with the whole module), for an easy integration of detector systems.

2.3.1. Mechanical Alignment

The detector stage can be translated in all three translation degrees of freedoms (DX1, DY1, DZ1). The translations in x and z direction are used for alignment and tiling multiple detector images, allowing to increase the field of view in the detector plane. The translation in y direction is used to select the geometrical magnification in combination with the sample position. In a typical horizontal configuration the distance between the detector and the source can vary between 0 mm to 1700 mm. The detector can be also moved in pitch (DP1) and roll direction (DR1). The roll is used for alignment and to switch between different orientations of the detector for detectors that do not feature a square-like field of view. The pitch is mostly used, if the optical axis is not chosen to be horizontal. Then the detector can be inclined to be still perpendicular to the central beam. The degrees of freedom and the corresponding accuracies are shown in table 2.2. The submodule is denoted in figure 2.7.

2.3.2. Indirect Detectors

As detector systems for the image formation mostly two indirect converting flat panel detectors are employed and direct converting detectors of the Medipix family are used. The effective pixel size of a projection image is only dependent on

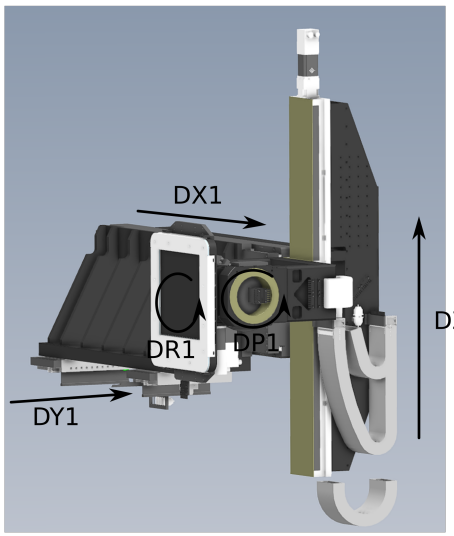

Figure 2.7.: Detector manipulator for alignment of the detector. Here the PerkinElmer XRD 1621 detector is mounted.

Table 2.2.: Degrees of freedom for the detector positioning

DOF	x	y	z	pitch	roll	yaw
travel	430 mm	2155 mm	1500 mm	90°	180°	-
precision	1.9 µm	2 µm	0.8 µm	45″	31″	-
axis name	DX1	DY1	DZ1	DP1	DR1	-

the magnification. Therefore, the source size and the number of pixels define the resolution in a well-designed imaging experiment.

These detectors are commercially available detectors and are widely used in medical applications and non-destructive testing.

The first indirect detector is a PerkinElmer XRD 1621 CN14 ES, featuring 2048×2048 pixels with a pitch of 200 µm. This results in an active area of 40 cm×40 cm.

As a scintillating layer DRZ+, consisting of a 208 µm layer of gadolinium oxysulfide, is used. For converting the visible light into an electrical signal a CCD is employed. The manufacturer reports a modulation transfer function of 25% at $2\,\mathrm{lp\,mm^{-1}}$ which corresponds to 80% of the Nyquist frequency at the given pixel size of 200 µm (a detailed introduction into the MTF is shown in section 3.2).

The second indirect detectors are a Dexela 1512CL and a Dexela 1207 (Varex Imaging) with a pixel pitch of 74.8 µm and 1944×1536 pixels resulting in an active area of 145.4 mm × 114.9 mm. The scintillating layer is composed of caesium iodine (CsI). The readout is CMOS based. A detailed examination of the imaging properties of such a detector is shown in [Kon+12]. There 50% MTF is reported to be at $1.2\,\mathrm{lp\,mm^{-1}}$ for photon energies of 50 keV and 70 keV and $3.3\,\mathrm{lp\,mm^{-1}}$ for 28 keV. $1.2\,\mathrm{lp\,mm^{-1}}$ and $3.3\,\mathrm{lp\,mm^{-1}}$ correspond to 18% and 50% of the Nyquist frequency of the pixel size of the detector.

The absorption of the scintillator in dependence of the energy is shown in figure 2.8. When optimizing the contrast in an imaging system, this is important (together with the source spectrum) as it will be described in section 4.1.

For both indirect detectors drivers were developed using the libuca framework[2] for fast image access and fixed interfaces to the detector parameters and functions.

2.3.3. Direct Converting Photon Counting Detectors

With new X-ray detectors it is possible to measure the spectral composition of the X-ray beam. This allows to determine the energy dependent X-ray mass attenuation coefficient which then allows to distinguish different materials. These detectors have a great potential for applications, but also are complicated systems. Therefore, I characterized such detectors in detail in chapter 3 for X-ray imaging with the aim of spectroscopic imaging and demonstrated the possibility to detect multiple contrast agents in test measurements by implementing a machine learning algorithm that decomposes single material images out of multiple images acquired with different energies. In addition, the use of a setup, capable of producing material decomposed CT slices, allows to optimize the imaging system in total. The method of spectroscopic CT is shown in detail in section 5.4. In particular, I examined the influences of temperature changes onto the sensor materials and different methods to handle these effects.

In imaging methods, based on X-ray absorption, a linear mass attenuation coefficient integrated along one ray is measured. Therefore, in projection imaging the integral over $\bar{\mu}\rho$ (product of averaged linear mass attenuation coefficient and the density) is measured, while CT allows to measure the voxel wise $\bar{\mu}\rho$. Therefore, a specific attenuation value cannot directly be correlated with a specific material. The detailed image formation process is described in detail in section 4.1.

[2] https://github.com/ufo-kit/libuca

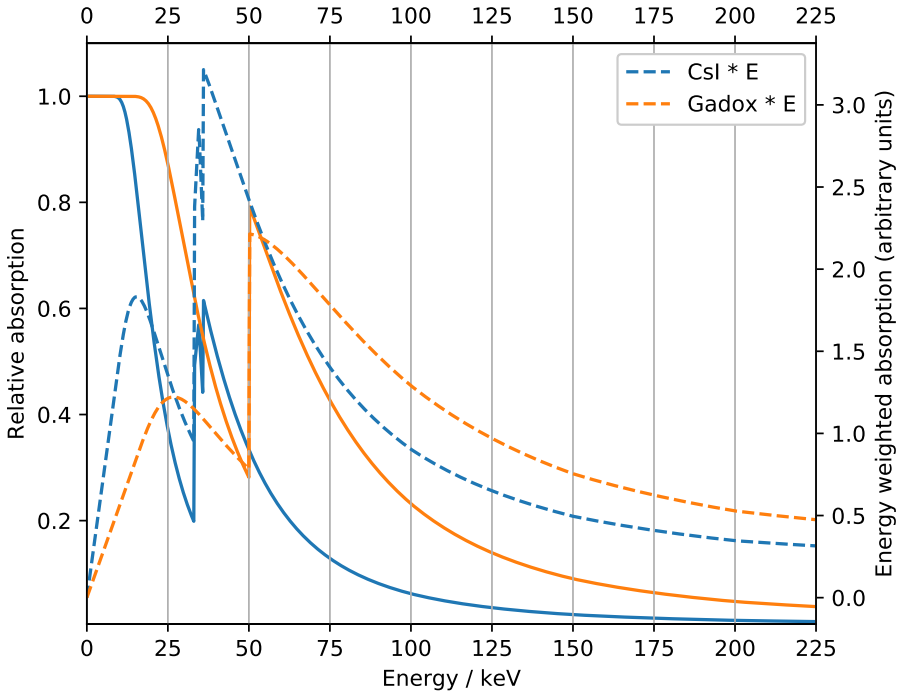

Figure 2.8.: Attenuation of X-rays within the scintillating layer of the two detector types depending on the energy. The dotted lines show energy weighted attenuation (weighted with the light yield that is approximately proportional to the energy).

While the commonly used methods for spectroscopic imaging use different photon spectra, detectors were developed that are able to detect the spectral information of the X-rays when interacting with the detector. X-ray spectrometers without spatial resolution, based on semiconductor sensors as germanium counters, widely used, but the possibility to include the energy discrimination within single pixel cells started in the 1990s. An intermediate development step were silicon-strip detectors that were used for high energy particle tracking, resulting in a 1D detector. Later, due to improvements in the electronics, 2D detectors became available.

2.3.4. Imaging Properties of Medipix

Photon counting detectors are an implementation of spectroscopic sensitive detectors. They also feature other unique properties, that are relevant for X-ray imaging. All interacting photons are counted equally, resulting in a different attenuation contrast then energy resolving detectors. They have a very high spatial resolution, that is almost only defined by the pixel size. In this part the basic functionality of photon counting detectors (in particular of the Medipix-Family) is explained and how these features' interplay with X-ray imaging. The broad parameter space of the photon counting detectors (hardware choices like sensor materials and pixel sizes as well as operation parameters that can be changed in runtime) has been examined to include this new detector technology into this laboratory setup.

The detailed properties of medipix detectors are characterized in the section 3. Here I will only give a brief summary of the main features of these types of X-ray detectors employed for imaging.

The detectors including the sensors feature extremely sharp images. Usually, the blurring, introduced by the sensor can be neglected for the resolution, resulting in point-like point-spread functions that are significantly smaller than the pixel size. But this also leads to the presence of aliasing. This issue needs to be suppressed in some applications.

The cut-off of the low energy noise by introducing an energy threshold gives these detectors almost ideal noise properties. A dark-current, as present in integrating detectors, is completely suppressed and the counting of the photons results in noise levels close to the Poisson noise limit. This makes these detectors well suited for low flux applications.

For high-flux applications the detectors imaging quality suffers from so called pile-up, when photons interact in shorter time steps than the readout can detect single photons. This limits the flux rates, where still a linear detector response is present, to typical values in the range $10 \times 10^6\,\mathrm{s}^{-1}\,\mathrm{mm}^{-2}$ to $10 \times 10^7\,\mathrm{s}^{-1}\,\mathrm{mm}^{-2}$, depending on the detector operation and pixel size[Fro+14; Ham+15].

The use of different sensor materials like CdTe, CZT, Si and GaAs allows implementing detector assemblies optimized for different energy ranges.

2.4. Sample Module

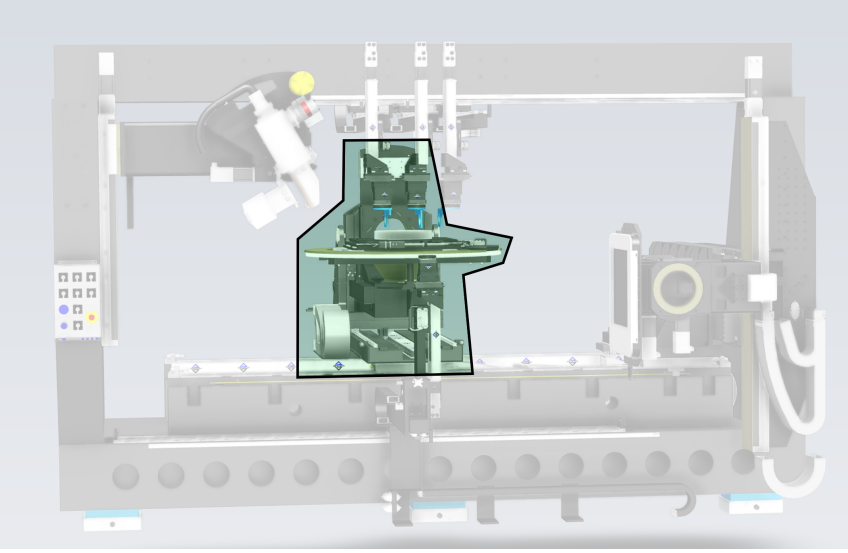

Figure 2.9.: Sample module of the CL/CT-Laboratory in the 'flat sample alignment' configuration.

All X-ray imaging methods are composed of the acquisition of different projections of the sample onto the detector plane. Therefore, the sample needs to be placed in a defined way within the X-ray beam. The sample module, that can be configured in multiple ways as described below, features the purpose to position the sample or to move it dynamically on a defined trajectory. The different configurations allow to optimize the sample positioning and alignment for different imaging methods and sample types.

The sample can be moved in the x and y direction (OX1, OY1). The y motion is used to select the geometrical magnification in combination with the y position of the detector. With the x translation the sample can be moved out of the beam in order to acquire images without any sample for compensations of the beam profile and for detector inhomogeneities. To align the axis of rotation, the sample stage can rotate in the pitch and roll motion. On top is a rotary stage with endless motion possibilities to perform tomographic measurements. In addition to the angular accuracy and repeatability, the tomographic axis requires a small so-called sphere-of-confusion. This denotes the radial and axial error motion of the axis when the axis is moved and should be smaller than the desired effective pixel/voxel size.

The radial and axial error has been measured 25 cm above the surface of the stage to be 0.867 µm and 0.602 µm, respectively. Therefore, the sphere-of-confusion allows tomographic measurements down to a resolution around 1 µm without significantly influencing the total spatial resolution.

The degrees of freedom and the corresponding accuracies are shown in table 2.3. This bare tomographic axis (and its alignment DOFs) are shown in figure 2.10. The tomography axis can carry up to 50 kg with a sphere of confusion below 5 µm.

These degrees of freedom, combined with the features of the source and detector module allow many geometrical configurations for computed tomography, computed

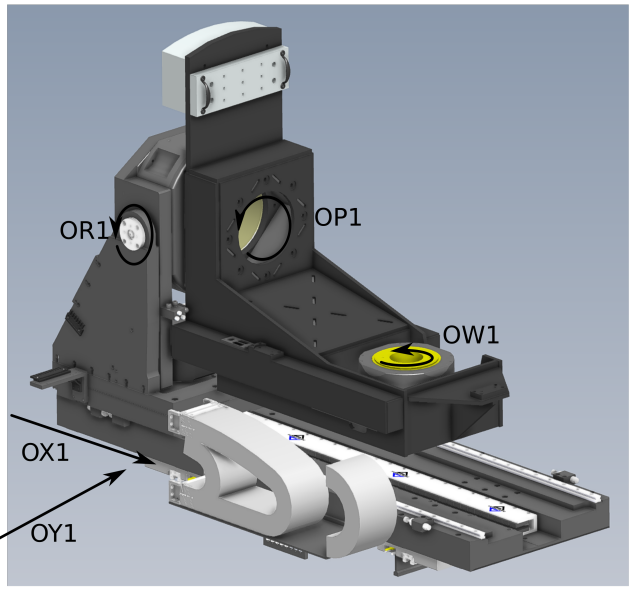

Figure 2.10.: Sample manipulator featuring the rotation stage for tomography and its alignment DOFs.

Table 2.3.: Degrees of freedom for the positioning of the tomographic axis.

DOF	x	y	z	pitch	roll	yaw
travel	1200 mm	2155 mm	-	95°	±2°	-
precision	2 µm	0.75 µm	-	0.8″	17.3″	-
axis name	OX1	OY1	-	OP1	OR1	OW1

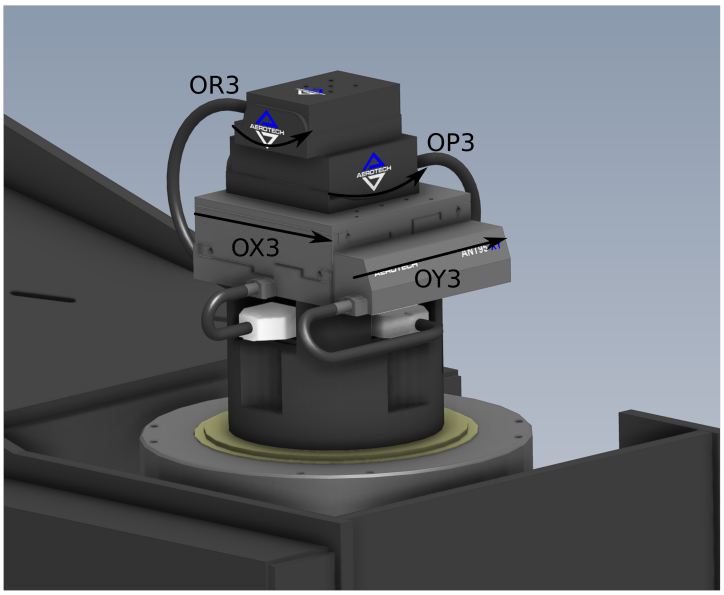

Figure 2.11.: High precision sample manipulator featuring 4 DOF for precise sample alignment.

Table 2.4.: Degrees of freedom for the high precision sample positioning on top of the tomographic axis.

DOF	x	y	z	pitch	roll	yaw
axis name	OX3	OY3	-	OP3	OR3	-
travel	±25 mm	±25 mm	-	±10°	±10°	-
precision	0.86 µm	0.76 µm	-	3.1″	3.1″	-

laminography and radiography imaging applications, e.g. to keep the sample horizontal and incline the rest of the components to realize a computed laminography setup.

2.4.1. High Precision Sample Alignment

In order to align a small sample on top of the tomographic axis, a high precision sample stage can be placed on top of the tomographic axis in x (OX3), y (OY3), roll (OR3) and pitch (OP3) direction. This allows a precise positioning of the sample on top of the tomographic axis. It is attached with a slip-ring and a following motor that steers the slip ring. The slip ring provides the necessary contacts for power and data connections of the four degrees of freedom stages. The two rotation degrees of freedom, allow to align long elongated samples precisely along the axis of the tomography motion. It is also possible to mount multiple samples stacked and to automatized scan them at different height positions. This gives the possibility to scan multiple samples directly after each other without a physical interaction of a scientist at sight. The degrees of freedom and the corresponding accuracies are shown in table 2.4.

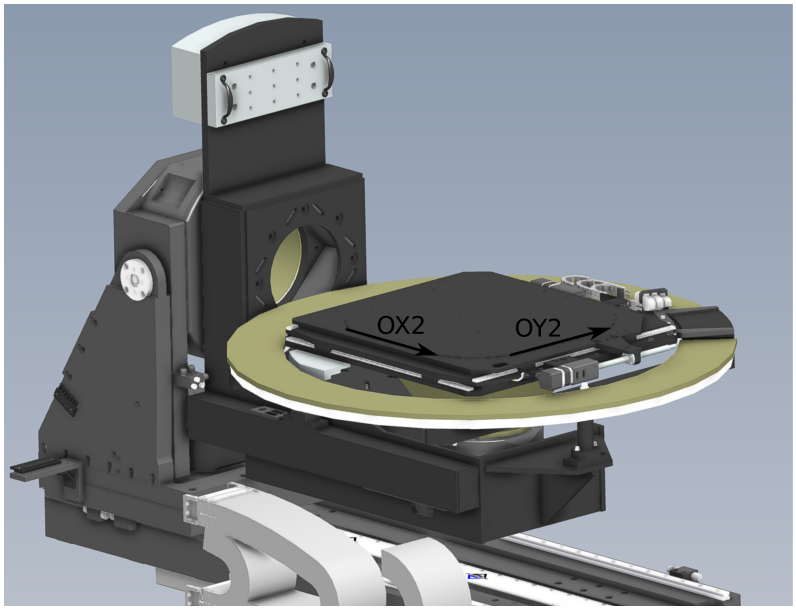

Figure 2.12.: Sample module for laterally extended samples. This module configuration is typically used for laminography experiments (see section 5.2).

Table 2.5.: Degrees of freedoms for the sample positioning in the laminography case on top of the tomographic axis.

DOF	x	y	z	pitch	roll	yaw
axis name	OX3	OY3	-	-	-	-
travel	±100 mm	±100 mm	-	-	-	-
precision	1.8 µm	1.1 µm	-	-	-	-

2.4.2. Flat Samples Alignment

To move a flat sample in a plane perpendicular to the tomographic axis, a large sample holder can be attached on top of the tomographic axis. It allows to move the sample 20 cm in both directions in its plane. This can be used in laminography to select the region of interest and to tile multiple laminographic scans. These motors are connected via a large slip ring, allowing continuous unlimited rotation. In addition, this slip ring features additional connections, that can be used for special applications, where power or data connections are required at the sample, like special sample environments. The total sphere-of-confusion suffers from the large sample holder, the slip ring and the inclination of the tomographic axis with respect to the pure tomographic axis. The SOC has been verified at inclinations of 20° and 45° to be 4.65 µm 5.58 µm, respectively. However, the error motion are quite reproducible, allowing to compensate for the radial error by an online correction motion of the two translation stages. This procedure reduces the SOC by at least a factor for two for all inclinations.

The degrees of freedom and the corresponding accuracies are shown in table 2.5.

2.5. Optics Module

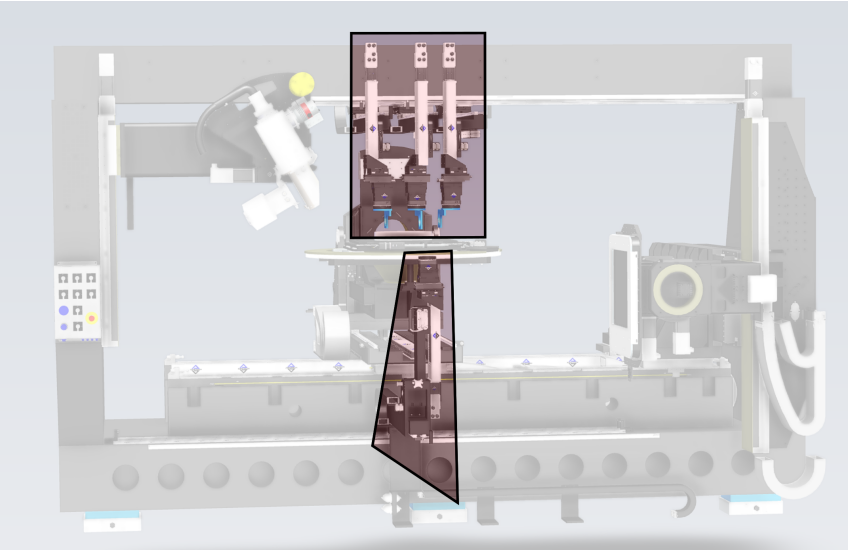

Figure 2.13.: The four modules for the placement of optical elements.

To place optical elements (like X-ray gratings, see section 4.2) for X-rays in the beam path, four motorized holders can be positioned in the beam path. One is attached to the bottom granite basement of the system and three are hanging from the top. Each of them features all six degrees of freedom. Each of them can be manually moved along a rail over the full range of the system. In order to fix them, they can be clamped with pressurized air brakes. An arbitrary pivot point of all rotations can be defied via the control system. This allows to always rotate around a specified point, e.g. if an off-centered holder is used. The corresponding adjustment motions are automatically performed in real time by the controller, keeping the virtual pivot always point at its fixed position in space while a rotation is performed. The degrees of freedom and the corresponding accuracies are shown in table 2.6.

A large set of different X-ray gratings are available to implement different types of interferometers.

Table 2.6.: Degrees of freedom for the optic holders. In addition the stacks can be individually position manually along a rail that covers the whole optical axis.

DOF	x	y	z	pitch	roll	yaw
travel	100 mm	50 mm	150 mm	±10°	±10°	±90°
precision	2.8 mm	3.5 µm	1.5 µm	3.5″	6.2″	7.2″
axis name	GX[1..4]	GY[1..4]	GZ[1..4]	GP[1..4]	GR[1..4]	GW[1..4]

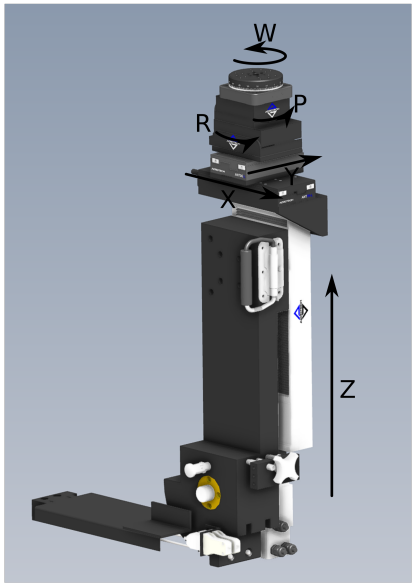

Figure 2.14.: One of the three sub-modules for the placement of optical elements with markings for the motorized alignment axes.

2.6. Control System

The whole instrument can be controlled via the control system *concert*, which has been developed at KIT in cooperation between IPS and IPE and is available as open source software[3]. The control system is based on python and features template implementations of devices and processes. For this system I implemented all the specific devices in the control system like the motors, detectors.

The control system allows easy control over asynchronous tasks, running in the background, and their synchronisation (e.g. performing multiple motions simultaneously).

I also implemented a set of 'standard' experiments to cover the most common imaging techniques, like different implementations of computed tomography, computed laminography, grating interferometry, fast radiography and tiled scans of samples.

The flexibility of the control system makes it easy to extend or change parts of the already existing experiment controls.

Also, the control system has full access to the image data of the detectors. This allows to process the image data online and also to use this data in feedback loops in the experiment (e.g. online check if the image data makes sense.). The image data can also be processed online or offline with the functions provided by the ufo-framework[4]. The 3D reconstructions can be performed with the tofu software[5], a collection of helper scripts for tomographic reconstructions with the ufo framework.

I implemented automized experiments, that are optimized for this particular setup, that are using all the possible features and information. Scans for computed

[3]https://github.com/ufo-kit/concert
[4]https://github.com/ufo-kit/ufo-core & https://github.com/ufo-kit/ufo-filters
[5]https://github.com/ufo-kit/tofu

tomography, laminography, grating interferometry were implemented. They feature an online check of the relevant parameters of the X-ray tube and can correct simple malfunctions automatically. This helps in long scans of multiple hours, where issues with the high voltage supply of the X-ray tube are quite common. Laminography and computed tomography can be run in stepped scans, where the sample is oriented in the correct angular position of the tomographic axis and afterwards an image is acquired. This then loops over all tomographic angles. Also, a continuous scan is implemented, where the tomography axis moves with a constant velocity and frames are acquired continuously. This scanning mode is preferred in fast scans to minimize the dead time between frames (e.g. for checking if the motor reached its position). For long scans the stepped mode is preferred. In this mode it is also easier to resume a scan, that stopped due to an unhandled fault in one of the components.

2.7. Resulting Parameter Space

Resulting from the previous characterizations and technical descriptions of the single components, this section will highlight how these results lead to parameters relevant for X-ray imaging. Such parameters are possible propagation distances, magnifications, resolutions in the sample plane etc.

Distance between source and detector The distance between the source and the detector is relevant for the magnification of the sample due to the cone beam. In the case of a horizontal central beam, the maximum distance between the source and the detector plane is 172 cm for the direct tube head and 20 cm less for the transmission tube head. The detector can be moved so close to the source, that the surface of the detector touches the exit window, resulting in a distance of 7 mm for the direct tube head and almost zero for the transmission tube head, where the target substrate also works as the exit window.

Effective pixel sizes and resolution The effective pixel p_{eff} size is given by the physical pixel size of the detector p_{det} and the magnification M. The magnification is defined by the fraction between the distance between source and sample (SOD) and source and detector (SOD) $M = \frac{SDD}{SOD}$.

For the laminographic setup (at an inclination of 30°), this results in a maximum magnification of 28.5, due to the shortest source sample distance of 60 mm for the direct tube head. In the CT geometry, the resolution is limited by the source size ($\approx$ 7 µm for the direct tube head and 1 µm for the transmission tube head). The blurring of the source (resulting in a penumbra in the detector plane), if given by $s(M-1)$ with the source size s.

Maximum sample size The maximum sample size is given by the field of view that can be covered by the detector and the corresponding magnifications. The detector can be translated in its plane by 43 cm and the images can be stitched afterwards. With the detector width of 40 cm, this results in an effective width of 83 cm.

The largest volume for a CT scan, that can be covered by the X-rays is given by the incircle (see figure 2.15).

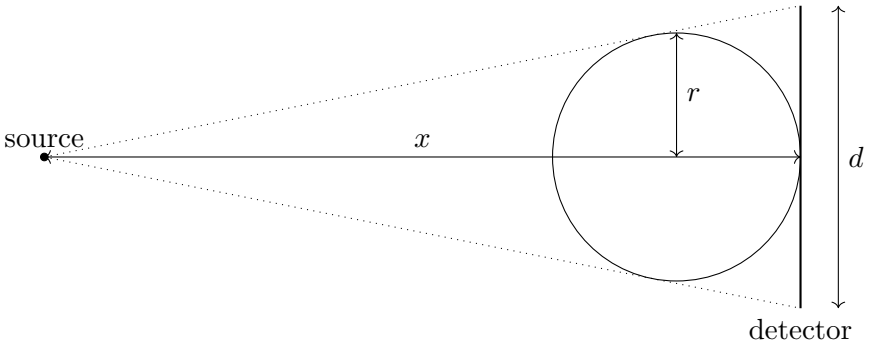

Figure 2.15.: Largest possible reconstructed volume for a source detector distance x and a detector size d.

The radius of the incircle is given by

$$r = \frac{xd}{2\sqrt{\left(\frac{d}{2}\right)^2 + x^2} + d}. \tag{2.1}$$

The resulting lowest magnification is then $M = \frac{x}{x-r}$.

For the 83 cm width, that can be achieved by stitching the largest detector and the largest distance between source and detector 172 cm, this results in a larges field of view of 65 cm with a 1.235-fold magnification.

In the laminography case, the largest field of view is not so important, since the sample can be tiled in the sample plan.

For grating interferometry the sample sizes are technologically limited by the size of the available gratings.

Energy range The X-ray tube, and external filters, that can be attached to the X-ray tube, allow to shape the energy spectrum. The possible acceleration voltages range from 20 keV to 225 keV. The resulting spectra for multiple settings (without external filters) are shown in figure 2.4 and 2.5.

Source size The minimal size of the source of the X-ray tube is dependent on the heat-load, that is created on the target. The X-ray tube controller automatically enlarges the target spot to keep the local heat-load on an acceptable level. This results in a minimal source size from 7 µm to 250 µm for the direct tube head. This minimal source size grows linear with the target power. However, since all the focusing and steering coil currents are exposed to the control system, it is always possible to intentionally enlarge the size of the source. The use of the special transmission tube head allows to realize source sizes even below 1 µm. Also with this tube configuration one can de-focus the source size intentionally to realize larger source sizes, which is an interesting feature for method development and to mimic other imaging systems.

2.8. Comparison of the newly Developed System with Other X-ray Imaging Setups

In this section other X-ray tube based systems are compared to this setup. All other systems, that were found during an extensive literature search ath the time of writing this thesis, are optimized for special tasks and often outperform our imaging laboratory for these special tasks. However, since the other systems are most of the time highly optimized to single tasks they do cover only small ranges of parameters and therefore lack the generality of this imaging system. Since our setup is intended to be very flexible it covers the largest volume in the parameter space. So far, no other system, that feature such a general approach is published in literature. The comparison with other imaging systems can also only be done in a qualitative way, since there is no general quality metric for X-ray imaging and the comparison is highly dependent on the application.

2.8.1. Large Samples

The Frauenhofer Institute IIS operates the *XXL-CT* in Fürth [XXLCT]. This setup is optimized for extremely large samples. Its largest possible field of view is given by 5 m for a full CT scan and the tomographic axis can handle up to 10 000 kg.

For penetrating such large and high absorbing objects, and linear accelerator is used to generate the X-ray beam. The acceleration energy can be selected from 4.6 MeV to 9 MeV. The source size is given by approximately 3 mm and the possible effective pixel sizes can vary from 800 µm to 4000 µm.

This setup makes it ideal to investigate large and dense object (e.g. full cars for crash tests).

2.8.2. High Sensitivity Grating Based Phase Contrast

A highly optimized laboratory setup for grating based phase contrast computed tomography is demonstrated here by Birnbacher et al [Bir+16].

This setup optimized the detector, the source (spectrum and size) and the grating shape to achieve the highest possible phase and visibility contrast. This limits the setup to fixed propagation distances and grating types.

The X-ray tube operates at an acceleration voltage of 40 keV and 70 mA current with a talbot laue grating interferometer, that is designed for 27 keV. The distances between the gratings of the symmetrical grating setup is given by 85.7 cm and all gratings feature periods of 5.4 µm. The magnification, that results from optimizing the sample position for the highest phase sensitivity, which is close to the phase grating, results in 1.72 fold with an effective pixel size of 100 µm.

2.8.3. High Resolution Compact CT Scanner

For high resolution CT scans small commercial table-top scanners are available like the Bruker Skyscan 1272 [SKY]. This system allows CT scans down to voxel sizes below 1 µm.

These systems are highly optimized for performing CT scans including a user-friendly software, that also includes the 3D reconstruction of the data. This hides

a lot of complexity from the user, but also does not allow extending or change the system behaviour for new methods (or to use it for tasks not intended by the manufacturer).

2.8.4. Imaging with Photon Counting Detectors

The Freiburg Materials Research Center (FMF) operates a laboratory setup for computed tomography with photon counting detectors [Pro+13].

In this setup the full potential of the Medipix detector family is included and samples with sizes up to 100 mm can be examined. Also the limited size of the currently available photon counting detectors is addressed with the possibility to combine stitched detector images.

This laboratory setup is clearly focused on the photon counting detectors.

2.9. Summary

In this chapter I described which components are relevant for X-ray imaging, how they contribute to the imaging system and how they are implemented in the here presented CL/CT-Laboratory. The features of all the subcomponents will be used in the following chapters. Some other, much more specialized and less general, X-ray imaging laboratories are presented for comparison and to show the uniqueness of the CL/CT-Laboratory.

3. Characterization of Energy Sensitive Photon Counting Detectors

Energy sensitive photon counting detectors are a promising new technology in the field of X-ray imaging. However, these detector systems are complex systems allowing optimizations for various tasks. Therefore, I will show a detailed characterization of such devices with the focus on parameters relevant for X-ray imaging. In section 3.1 the spectroscopic parameters are evaluated. The spatial resolution and its dependence to the energy settings is examined in section 3.2. How noise is propagated through the detector is characterized by the means of the detective quantum efficiency in section 3.3. In the last section 3.4 of this chapter, temperature influences are examined by evaluating the quality of spectroscopic CT (see 5.4).

In a pixelated spectroscopic detector each pixel cell acts as a spectrometer. However, it is currently not technological feasible to process a full spectrum per pixel in a large detector for large photon fluxes as used in X-ray imaging methods. Only the new Timepix3[Poi+14] and Timepix4[Llo+22] are giving these possibilities for a limited amount of X-ray flux. Therefore, counting detectors feature a discriminator logic within one pixel cell, as well as counters and count only the amount of events, that fulfill certain criteria. This results in a 2D image of counter values, or multiple of these, if more counters, and discriminators are present. The basic design of hybrid pixel detectors, composed of a semiconductor sensor, and a read-out electronics is mostly the same for all detector families.

This basic design of a single pixel cell is shown in figure 3.1. On the top there is a semiconductor with an applied bias voltage. Without an interacting photon the semiconductor is almost completely isolating (depending on the sensor material a constant leakage current is present, that needs to be addressed by the readout electronics) and therefore only a constant current is flowing. Since every pixel needs to be connected to a readout logic, all pixels feature a bump bond, allowing to connect the sensor material with its corresponding readout cell, that is located below the sensor material. When a photon interacts in the sensor volume a cloud of free charge carriers (electrons and holes) are created. These charge carriers are accelerated by the applied electric field and therefore drift towards the two electrodes of the sensor and are inducing a current pulse in the readout electronics. The amount of free movable charge carriers is proportional to the deposited energy, therefore also the amount of induced charge (time integral over the current pulse) is proportional to the photon energy.

The sensor material defines many properties of the detector system. The X-ray attenuation (see figure 3.2) defines the probability of a photon to interact with the sensor material. If such an interaction takes place, the created charge carriers must be detectable by the readout. With a given bias voltage the created signal is proportional to the product of the lifetime and the mobility of the charge carriers (the so

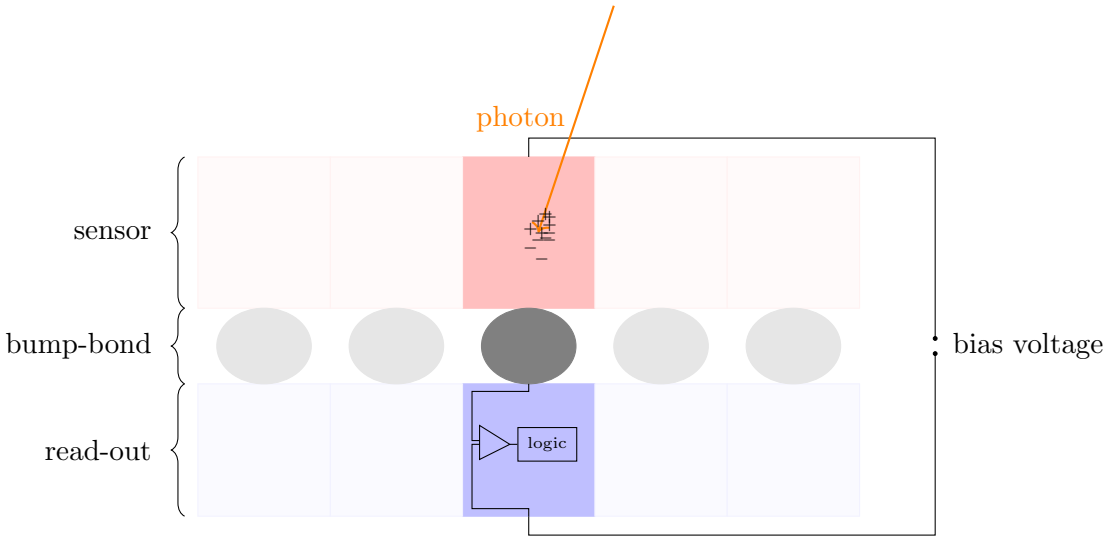

Figure 3.1.: Basic layout of a single pixel cell, embedded between adjacent pixels.

Table 3.1.: Material Properties of different sensor materials. The density ρ is given in $\mathrm{g\,cm^{-3}}$, the resistivity in $\Omega\,\mathrm{cm}$, the $\mu\tau$ products in $\mathrm{cm^2\,V^{-1}}$ and the energies in eV. E_g is the band gap energy and E_i the energy required to create one electron hole pair. Density, $\mu\tau$ products and the energies are from[Spi06].

	ϱ	resistivity	$(\mu\tau)_e$	$(\mu\tau)_h$	E_i	E_g
Si	2.33	1×10^4-10×10^4	>1	>1	3.6	1.12
GaAs	5.32	3×10^8([Bla82])	8×10^{-5}	4×10^{-6}	4.2	1.43
CdTe	5.85	10×10^9([Acr21])	3×10^{-3}	2×10^{-4}	4.43	1.44
$Cd_{0.9}Zn_{0.1}Te$	5.78	10×10^{11}([Acr21])	4×10^{-3}	1.2×10^{-4}	4.64	1.572

called $\mu\tau$ product). Typical electronic properties are shown in table 3.1. The amount of impurities in the semiconductor has a strong influence onto the $\mu\tau$ product. Silicon features excellent semiconductor properties, but due to the small compared atomic number, the attenuation is poor for higher energies. Other semiconductors, like Gallium Arsenide (GaAs), Cadmium Telluride (CdTe) and Cadmium Zinc Telluride (CZT) with higher atomic numbers are promising materials for higher energies. The electronic parameters improved significantly in the last decade (see [Ham+15].

The shaping of the readout electrode and the pixel size can be used to suppress negative effects of a poor $\mu\tau$ product of a single charge carrier type. Due to the so-called small pixel effect [Spi06], the signal of a charge carrier cloud is not equally created in all depth layers in a sensor, but has the largest influence close to the readout electrodes. By letting drift the charge carriers with the worse $\mu\tau$ product towards the planar electrode and the charge carriers with the better $\mu\tau$ product towards the pixelated side, mostly the charge carriers drifting towards the pixelated side contribute to the detected signal.

By implementing a proper charge sensitive amplifier (CSA) pulses with a height proportional to the induced charge are created and then be passed to a logic for further processing. In the photon counting detectors of the Medipix family a Krum-

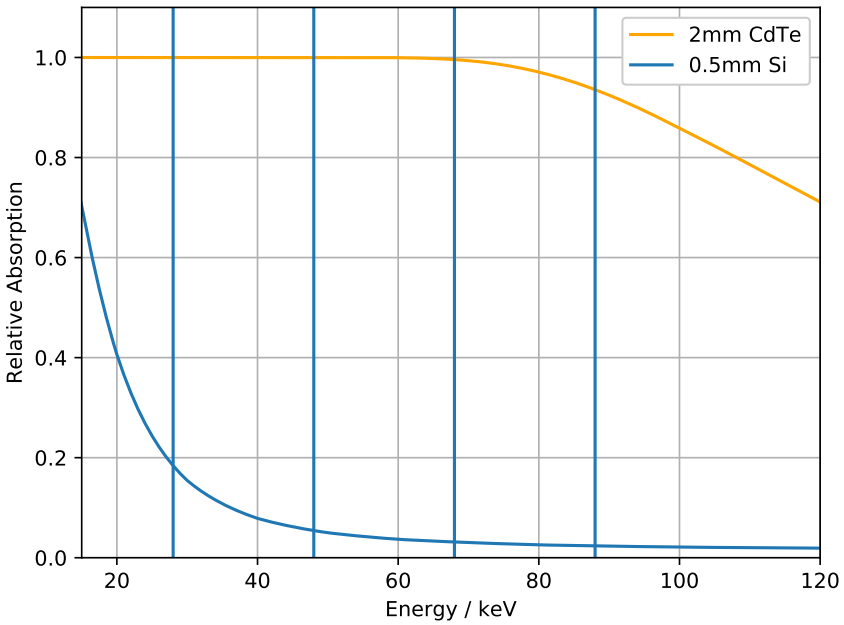

Figure 3.2.: Relative absorption for typical Si and CdTe sensors[US].

menacher feedback circuit is employed. The circuitry of the Krummenacher feedback circuit is shown in figure 3.3

The Krummenacher feedback circuit has two purposes. The first is used as a leakage current compensation, that works individually for each pixel cell. The leakage current is an almost constant current, running through the sensor due to the not perfect insulating properties (see resistivity in table 3.1)). The leakage compensation removes this offset from the photon event pulse. The circuitry is a high pass filter, that removes a constant (or slowly changing) current from the input signal. The total amount of current, that can be compensated, is given by $I_{\mathrm{Krum}}/2$ for electron collection and I_{Krum} for hole collection. The second feature is the pulse shaping. An increased value of the I_{Krum} current results in shorter and lower pulses. This leads to an increased maximum count rate, that can be recorded, and a reduced energy resolution due to the reduced pulse height[Fro+14]. If the I_{Krum} current value is too large undershoots in the signal can be created which should be avoided to keep a flux independent spectroscopic behaviour of the detector.

The logic part of the readout typically includes thresholds, comparators and counters, that count the number of photons that are fulfilling certain criteria. This allows to count the number of photons, detected by their current pulses, exceeding an energy threshold.

Different detectors of the Medipix family have been employed in this work. All these detectors feature a native pixel pitch of 55 µm. The differences between these detectors, and their specific advantages are shown in the following part.

In particular, Timepix[Llo+07] and Medipix3RX[Bal+13] detectors were employed in this work, bonded to different sensor materials. All of them feature basic counting

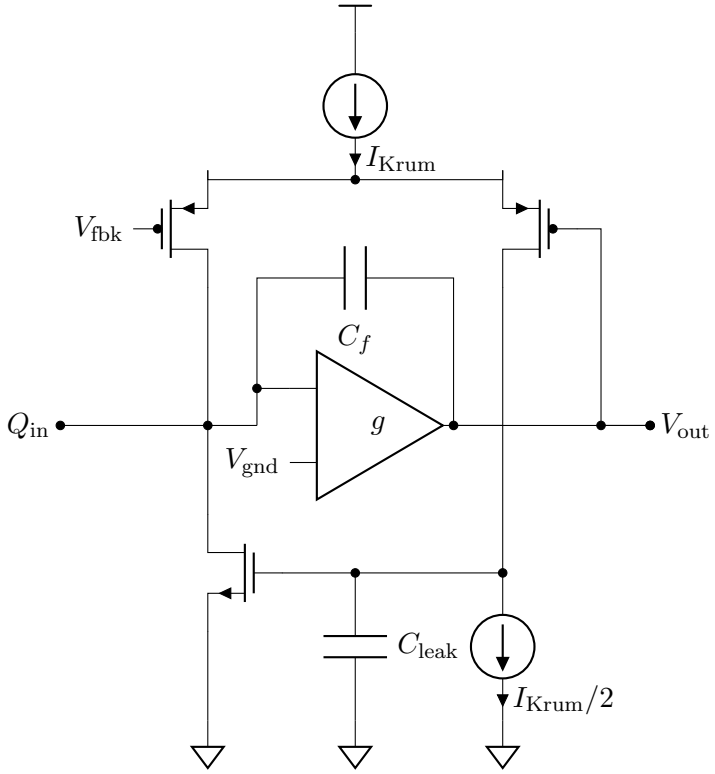

Figure 3.3.: Krummenacher feedback circuit. The sensor is connected to Q_{in} and the V_{out} will pass the offset corrected and pulse shaped signal to the comparator. The shaping of the pulse and the amount of leakage current, that can be compensated can be tuned with the inputs I_{Krum}, V_{fbk} and V_{gnd}.

capabilities, like counting a photon, that exceeded a particular energy threshold.

Timepix: The timepix detector can be operated in photon counting mode and in time-over-threshold mode. In the counting mode, one energy threshold can be set and works as a low energy threshold. All events, that create a pulse exceeding this threshold, are counted. Since the threshold cuts out all signal contribution with a small contribution, no noise is summed up over time as in an energy integrating detector. Therefore, these detectors are often called 'noise-free'.

The energy threshold can be set globally for all pixels of one chip. To compensate for pixel-to-pixel variations each pixel features multiple threshold adjustment bits. In the case of the Timepix four adjustment bits are present. The bits can be set pixel wise and add a linear shift to the energy threshold. The adjustment bits can be optimized by scanning the energy threshold and detecting the pixel wise noise level or test pulses. There is also the possibility to adjust the thresholds to get the most homogeneous flat-field image (see [Koe+11a; Zub+14]). In the latter adjustment process, the pixels show a slightly larger threshold dispersion. However, the more homogeneous intensity values can have use cases, e.g. when the dynamic range needs to be maximized or when no intensity calibration can be performed when no flat field image can be recorded.

In a single frame all photons with an energy above the threshold are counted.

By scanning the energy threshold and recording the counts of the pixels, spectra can be measured. The lowest possible energy threshold, that is defined by the noise level of the amplifier output, is typically in the order of 5 keV (depending on sensor material, temperature and chip quality).

Since there is no summed up noise (dark current) , the dynamic range of the detector is only defined by the exposure time and the counter depth of a single frame. Therefore, there is no difference if one frame is exposed for long or if multiple frames are recorded with a larger frame rate and summed up afterwards.

Besides the counting mode, where all photons are counted, the detector also features a time-over-threshold mode that does not count the number of photons, but the number of clock cycles the input signal exceeded the applied energy threshold. This timing value is almost linear dependent on the energy of the deposited energy. This allows to directly measure the energy of each interaction. However, only one photon is allowed to interact in each pixel within one acquisition. This makes this operation mode not ideal for imaging, where hundreds of photons are required per pixel to form an image, and the typical image readout is in the order of a few frames per second. In this work only the counting operation mode is used.

Medipix3RX: The Medipix3RX features the standard counting mode (as described for the Timepix) but adds the possibility of an internal coincidence detection of interaction in adjacent pixels. This allows to detect and correct for interactions, that are distributed over pixel borders. The normal operation mode without taking the signals from the adjacent pixel into account is called single pixel mode (SPM). This mode allows to use two thresholds/counters in parallel, allowing acquiring two different images corresponding to different parts of the spectrum. The mode, that checks for adjacent events and sums the total charge up is called charge summing mode (CSM). The CSM in detail works like this: Each individual pixel has two energy thresholds. The first one is used as a discriminator of the detected charge pulse. The charges of pixels in which the discriminating threshold was exceeded is sent to a 'summing node', where the charge all 2x2 pixel cluster is summed up. If this summed charge exceeds the second threshold, the counter of the pixel, that contributed the most of the total charge is incremented.

In addition, the detector can also be operated in the so-called colour mode. In this operation mode 2x2 pixels are clustered to a larger pixel (with a pixel pitch of 110 µm) and the flip chip bonding needs to be adjusted accordingly. Now each of this larger pixels work like the pixels in the normal operation mode, but more counters and thresholds can be used. This allows to apply four energy thresholds in the CSM mode within one acquisition and to read the four corresponding counters within one acquisition. In the single pixel mode eight thresholds/counters can be applied.

Charge Sharing: The semiconductor sensor is a bulk material, so charge can travel trough pixel borders. This typically can occur if a photon interacts close to a pixel border. While the charge drifts towards the readout electrode, the size of the charge carrier cloud extents due to diffusion and repulsion. The spread of the charge depends on the sensor material, the thickness and the applied bias voltage. While the charge sharing allows to detect interaction within sub-pixel resolution, if the single

events can be completely read out (like in tracking detectors, see [Spi06]), in counting detectors there is typically not the possibility to get the full interaction data out of the detector at typical interaction rates.

Also, the presence of characteristic absorption edges and their fluorescence photons in the sensor material effect the spatial and spectral resolution of a detector system. For CdTe the energies of the fluoresences are 23.2 keV and 27.5 keV. The absorption length of a photon in this energy range is in the order of 100 µm. This means, with the employed detectors of the medipix family and a pixel size of 55 µm, fluorescence photons can easily be detected in an adjacent pixel or even more far away.

In figure 3.4a gives a sketch how a photon is processed by the readout electronic, if its charge is shared over multiple pixels. Each pixel detects a photon with a fraction of the original charge. The amount of detected charge is denoted by the size of the dotted circles at the pixel centers. The presence of charge sharing results in more low energy photons that are detected but not present in the incoming photon spectrum.

The charge summing mode was introduced in the Medipix3 and has been optimized in the Medipix3RX[Bal+13]. The adapted sketch for this acquisition mode is shown in figure 3.4b. Each single pixel cell detects the amount of charge, that is deposited in its area. If this charge exceeds a certain threshold (to suppress noise), the charge is sent to a so-called summing node. These nodes are denoted by the solid black circle in the sketch. In the summing node all charges of the adjacent pixels are summed up and are sent to the pixel with the largest contribution. If the summed charge exceeds an additional threshold, the pixels counter is incremented. The total recovered charge is denoted by the size of the dashed circle. This results in an almost completely reconstructed charge amount in the pixel where the photon was absorbed. In the Medipix3RX one counter can be used for this operation mode.

In addition, the so-called color mode is possible. In this operation mode 2x2 pixels are put together into one large pixel. These larger pixels now feature the same functionality as the normal CSM but each 2x2 pixel cluster now features four counters with independent thresholds. To operate the chip in this mode only one pixel input must be connected via bump ponds with the sensor. Therefore, one must decide over the operation mode in the production process and one can not change its behaviour in operation.

The different influences on the detector performance for imaging applications is characterized in the next sections.

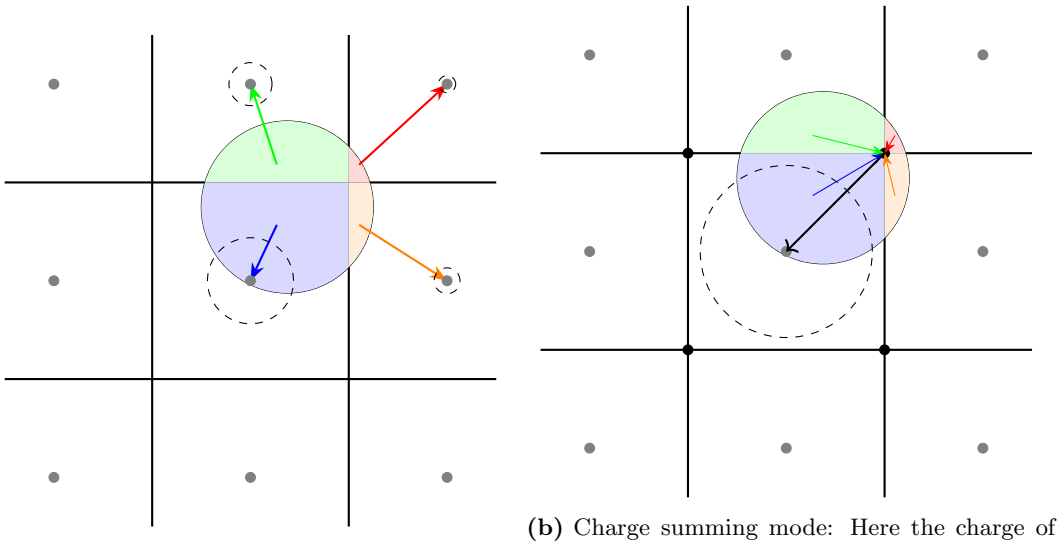

(a) Single pixel mode: Here the fractions of the deposited energy is distributed in multiple pixels. Each of the pixels will detect a photon with a fraction of the original energy.

(b) Charge summing mode: Here the charge of all the pixels is summed in the summing node and assigned to the pixel with the largest contribution, resulting in a correct detection of a single photon with the correct energy.

Figure 3.4.: Interaction of a charge shared photon interaction in different operation modes. Adapted from [Bal+13; Koe+14a].

3.1. Energy Resolution Measurements

For the use of spectroscopic CT the energy resolution of the detector system is a crucial part. Therefore, I show in this part the characterization of the energy response functions (measured with monochromatic synchrotron radiation and radioactive sources) of different detectors, operation modes and sensor materials for the use in spectroscopic CT. The correct understanding of the spectroscopic behaviour of such detectors allows to choose the best setting for a particular application.

The spectroscopic performance of a detector can be characterized by its energy response functions (ERF). The ERF is the measured spectrum, when the detector is exposed to monochromatic radiation. With a photon counting detector, that features a low energy threshold, such a spectrum can be recorded by scanning the threshold and measuring the count rate. Since all photons above the energy threshold are counted, the differential spectrum can be derived by taking the derivative of the measured integral spectrum. In such a spectrum, typically a low energy charge sharing tail can be observed and, depending on the sensor material, characteristic peaks, emerging from fluorescence, and the corresponding escape peaks. Silicon does not have strong enough characteristic lines within the utilized energy range. The used CdTe and CZT ($Cd_{0.9}Zn_{0.1}Te$) has the characteristic fluorescences at the energies 23.2 keV (K_α of cadmium) and 27.5 keV (K_α of tellurium).

The measured spectrum, when the detector is exposed to polychromatic radiation, is a combination of all ERF of all the present incoming energies. Since the characteristic peaks are present at the same energy for all incoming energies above the K-edges, those peaks are always part of a measured spectrum. The charge sharing tail and the escape peaks are dependent on the incoming energy, and therefore are

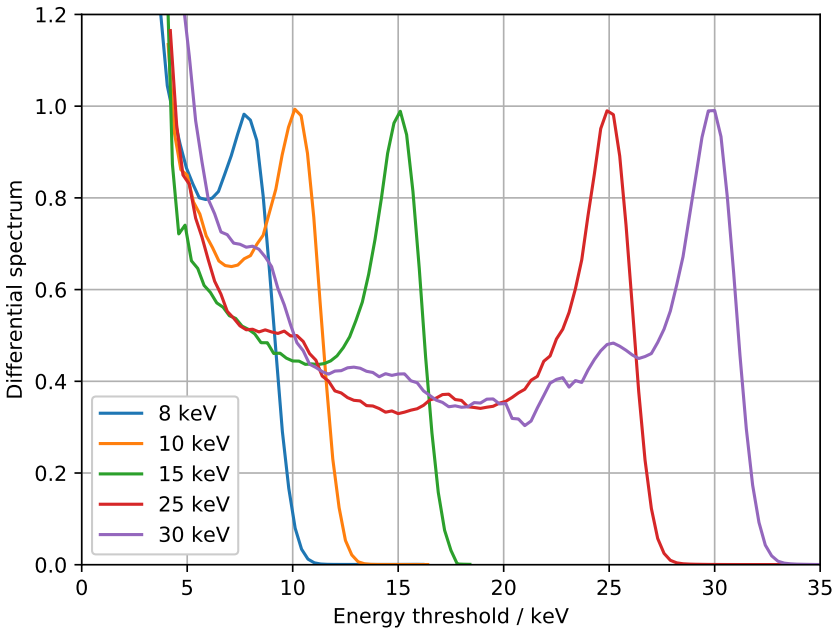

Figure 3.5.: Energy response functions measured with a 500 µm thick silicon sensor based Timepix. The different colors denote different incoming photon energies. A monochromatic synchrotron beam was used with a bandwidth of 2%.

smeared out.

The probability of absorption of a fluorescence photon within 55 µm of CdTe is 37% and 58% for the two energies and 60% and 83% within 110 µm of CdTe. When a single photon creates a charge cloud, that is detected within more than one pixel cell, the detector detects multiple photons with a fraction of the original photon energy. This is called charge sharing (operation described in more detail in section 2.3.4). This causes the background signal for low photon thresholds in the ERFs.

To minimize these artifacts, the so-called charge summing mode (CSM) has been introduced in the Medipix3(RX) detector chips[Koe+14a; Bal+07; Bal+13]. This integrated logic sums the analog signal, that is proportional to the measured charges, in the adjacent pixels and assigns one hit with the summed charge to the pixel with the largest contribution. This effect reduces the charge sharing a lot, since the charge distribution in CdTe is in the order of 25 µm (see section 3.2) and therefore almost all charges are deposited within a 2x2 pixel cluster.

For most events with fluorescence photons, the florescence photon and the remaining energy are collected by the charge summing logic within one summing node.

For the different sensor materials Si (Timepix 55 µm pixel pitch), CdTe (Medipix3RX 110 µm pixel pitch) and CZT (Medipix3RX 110 µm pixel pitch) measured energy response functions are shown in the figures 3.5, 3.6 and 3.7.

The silicon based Timepix was exposed to monochromatic synchrotron radiation of different energies (bandwidth 2%). CdTe and CZT were exposed to an ^{241}Am source, that emits photons at an energy of 59.6 keV.

For an ideal detector system, a delta peak would be expected in the energy re-

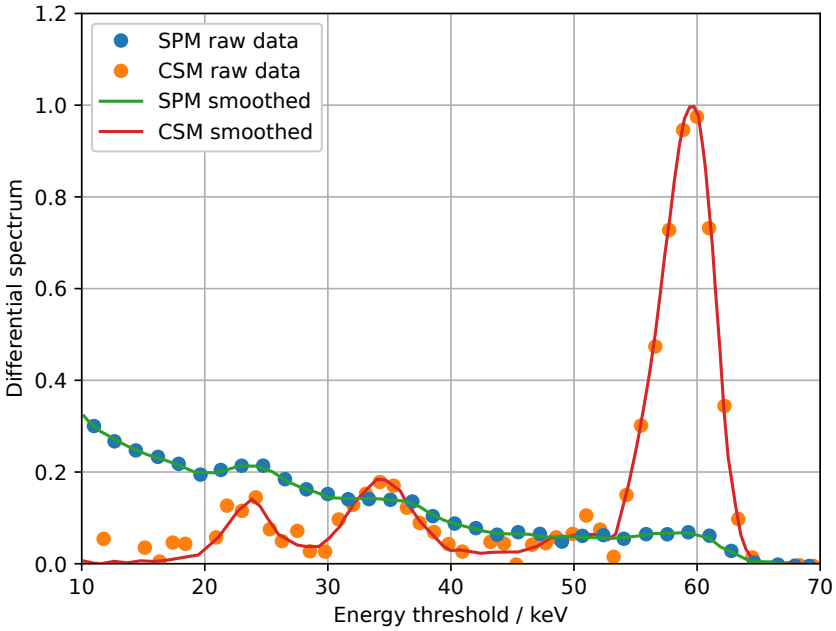

Figure 3.6.: Energy response functions for a 2 mm thick CdTe sensor bonded to an Medipix3RX detector operated in single pixel mode and charge summing mode. The points show the original measured data, the lines a gradiant weighted diffusion filter. The fluorescences at 23.2 keV (K_α of cadmium) and 27.5 keV (K_α of tellurium) are clearly visible. An ^{241}Am source was used for this measurement.

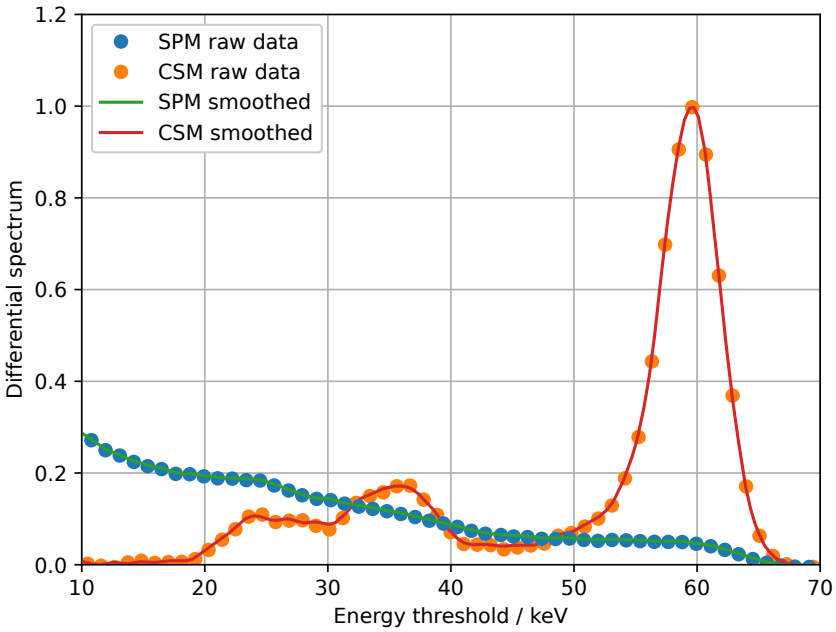

Figure 3.7.: Energy response function of a Medipix3RX bonded to a 2 mm thick CZT sensor. The fluorescences at 23.2 keV (K_α of cadmium) and 27.5 keV (K_α of tellurium) are clearly visible. An ^{241}Am source was used for this measurement.

sponse function. Also, a detector system, that features an extended peak at the incoming photon energy would be favoured. A system that unevenly shifts photons to other energies makes it complicated to perform measurements where the energy discrimination is required.

For the silicon sensor, that does not feature a charge summing mode, the low energy tail, caused by the photon events, that are shared between adjacent pixels, is clearly visible. When looking only at the peak of the photo absorbed photons, a full width half maximum below 4 keV for all energies can be detected. Since the spectra of all pixels of one chip are summed, that dispersion of the energy threshold between the different pixels also influence the width of the peak. The threshold dispersion has been measured to be (0.492 ± 0.100) keV. The error denotes 95% confidence intervals calculated by the means of bootstrapping of the results of the different chips of the assembly. Realigning the single pixel spectra would result in a sharper peak. However, since usually only a global energy threshold can be applied to all pixels for a single acquisition this would show the actual performance of the detector system.

The energy response functions for CZT and CdTe show great differences between the single pixel mode and the charge summing mode. The charge cloud is so large that the 110 µm pixel pitch CZT and CdTe detectors are dominated by charge sharing in the single pixel mode. Even the photo absorption peak at the interacting energy is no longer visible.

However, the charge summing mode is able to recover a spectrum with almost no charge sharing background. Only the fluorescence and escape peaks are visible,

but are way more suppressed than in a 165 µm pixel pitch CdTe detector operated without charge summing[Koe+11b].

The CZT shows no significant difference to the energy response function of CdTe. For both sensor material in the SPM cases, the charge sharing is so prominent that the photo peaks are not visible anymore. The CZT features a full-with-half-maximum of 5.3 keV and the CdTe 5.0 keV at the photo peak in CSM. These values are not in the range of typical spectrometers (which typically does not provide any spatial information), but allow to discriminate e.g. K-edges of different elements with a separation more than 15 keV like gadolinium and iodine.

The charge summing mode significantly improves the spectral performance of the photon counting detectors. The energy response function is much closer to the ideal case.

All the recorded ERF were also used to perform a calibration of the digital threshold values to real photon energies.

3.2. Spatial Resolution

Photon counting detectors, that I employed for spectroscopic CT, feature a high spatial resolution. However, the spatial resolution is not only dependent on the pixel size and sensor material but also depends on different other detector parameters. The modulation transfer function has been examined for different detector types, sensor materials and operation modes. These parameters can be used to actually control the behaviour of the detector to examine the feedback from whole imaging system (see 4.2.6).

The resolution of an imaging system is an important measure for its quality. The total resolution of an imaging system is determined by the source size, the detector resolution and, depending on the measurement, the mechanical stability of the setup or the correctness of its motion trajectory. In addition, also the sample itself can influence the resolution of an imaging system, when the sample interacts with the beam in a way that is not taken into account in the image reconstruction, like incoherent compton scattering, that stochastically changes the propagation direction of the X-rays. In this section the influences of the detector system is characterized for photon counting detectors. For the case of photon counting detectors this is an even more important measure, since the resolution can be changed by the operation modes of the detector assembly.

Most imaging systems can be described as a linear and shift invariant system. Such a two-dimensional system can be characterized by its point spread function (PSF), the response to a point like input signal. The size and the shape of the PSF gives directly the spatial resolution of the imaging system. A broad PSF results in a blurry image while a smaller PSF results in sharper images.

The detected image $I(x, y)$ can be described as the convolution of the incoming intensity field $I_0(x, y)$ by the PSF.

$$I(x, y) = I_0(x, y) * \mathrm{PSF}(x, y) \tag{3.1}$$

The convolution can be rewritten as a multiplication in frequency space.

$$I(x,y) = \mathcal{F}^{-1}\{\mathcal{F}\{I_0\}(\nu_x,\nu_y) \cdot \mathcal{F}\{PSF\}(\nu_x,\nu_y)\} \tag{3.2}$$

We assume that $\mathcal{F}\{PSF\}(\nu_x,\nu_y)$ is identical in x and y direction, and we call it transfer function (TF(ν)). By normalizing the transfer function to 1 for $\nu = 0$ we get the modulated transfer function (MTF)

$$\mathrm{MTF}(\nu) = \frac{\mathrm{TF}(\nu)}{\mathrm{TF}(0)}. \tag{3.3}$$

The MTF denotes how much a specific frequency in the incoming intensity pattern is attenuated or amplified by the imaging system. Typically, the resolution of an imaging system is defined by the frequency where the MTF drops below a certain value.

The PSF can be measured directly by exposing the detector to a point like illumination (e.g. with a pinhole). This is technically challenging, since the pinhole must be significantly smaller than the pixel size, or its shape must be exactly known to eliminate the influences of an extended illumination instead of a point-like illumination.

Another possibility is to measure a line spread function, that gives the point spread function in one dimension with a thin slit. With a sharp edge it is possible to measure the so-called edge spread function, that can be converted to the LSF by taking its derivative.

In the case of photon counting detectors, that feature PSFs that are smaller than the pixel size, a method needs to be employed that results in a finer resolution in the measured functions. This can be achieved by oversampling the functions.

In order to do so I performed an experiment in which the detector was illuminated with a tungsten edge in the beam path. The edge is slightly inclined. By fitting a line to the projected edge on the detector image, it is possible to calculate the perpendicular distance of each pixel with respect to the line. Now the intensity is sampled in finer steps than the pixel size. This method also excludes the influence of the square-shaped pixels and results in the so called pre-sampling modulated transfer function ($\mathrm{MTF_{pre}}$). The $\mathrm{MTF_{pre}}$ was determined as described in [Koe+14a; Boo94][1]. The model uses a weighted sum of a normal distribution.

The analytical model allows to perform the Fourier transformation, that is required to get from the edge spread function (ESF) or line spread function (LSF) to the MTF without introducing additional noise and the resulting $\mathrm{MTF_{pre}}$ is a smooth curve.

This $\mathrm{MTF_{pre}}$ allows to tell a lot about the properties of the sensor material, since the PSF is basically the charge spread that is induced in the electrodes.

To include the pixelated shape the $\mathrm{MTF_{pre}}$ needs to be multiplied by the Fourier transformed pixel shape ($\sin(\nu)/\nu$), which adds additional zero crossings.

Due to the broad $\mathrm{MTF_{pre}}$ this results in multiple values of the MTF significantly higher than zero for frequencies above the Nyquist frequency, which can lead to aliasing in the recorded images. These higher frequencies need to be canceled out by a proper experimental design (like choosing a proper source size) or one needs to take this carefully into account in the data processing.

[1] data processing performed by Thomas König

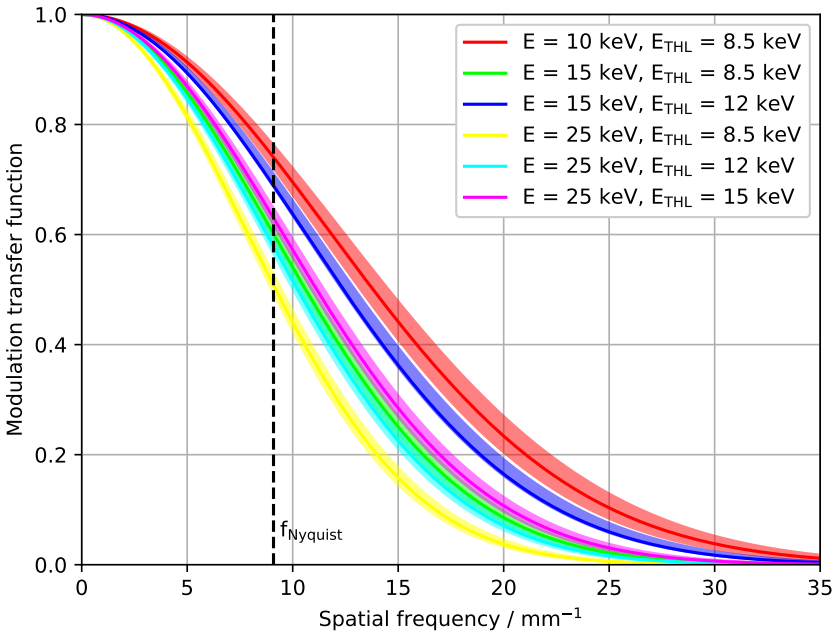

Figure 3.8.: MTF_{pre} of silicon Timepix detector for different photon energies and energy thresholds. The colored areas denote 95% confidence intervals.

The measured MTF_{pre} for a 500 µm thick silicon sensor, bonded to a Timepix is shown in figure 3.8.

The detector assemblies were exposed to monochromatic radiation at the Topo-Tomo beamline of the IPS imaging cluster, featuring a parallel beam and a double multilayer monochromator with an energy bandwidth of 2%. The tungsten edge was aligned to be perpendicular to the sensor and was placed as close as possible to the detector to minimize influences of an extended source. The distance between the source and the tungsten edge was approximately 30 m and the distance between the edge and the detector several cm. The size of the source was 800 µm × 200 µm. This results in a blurring of the edge below 300 nm.

Multiple positions of the projected edge on the detector were used to allow an error estimation. The images were flat field corrected and afterwards the edge positions fitted and the model MTF_{pre} was fitted to the oversampled edge spread function. Out of the different measures of the MTF_{pre} of the same detector, 95% confidence intervals were calculated by the means of bootstrapping.

One can see, that for lower photon energies and for higher threshold values the modulation transfer function becomes larger. The amount of charge sharing increases with higher photon energies. Therefore, the higher photon energy results in a worse MTF. By raising the energy threshold, more parts of the charge shared event are cut out. This leads to a smaller sampling area of a single pixel. Basically, the pixel becomes more insensitive at its borders, since there it is most likely, that an interaction is shared between adjacent pixels.

For the Medipix3RX detectors the MTF_{pre} differs significantly for the different

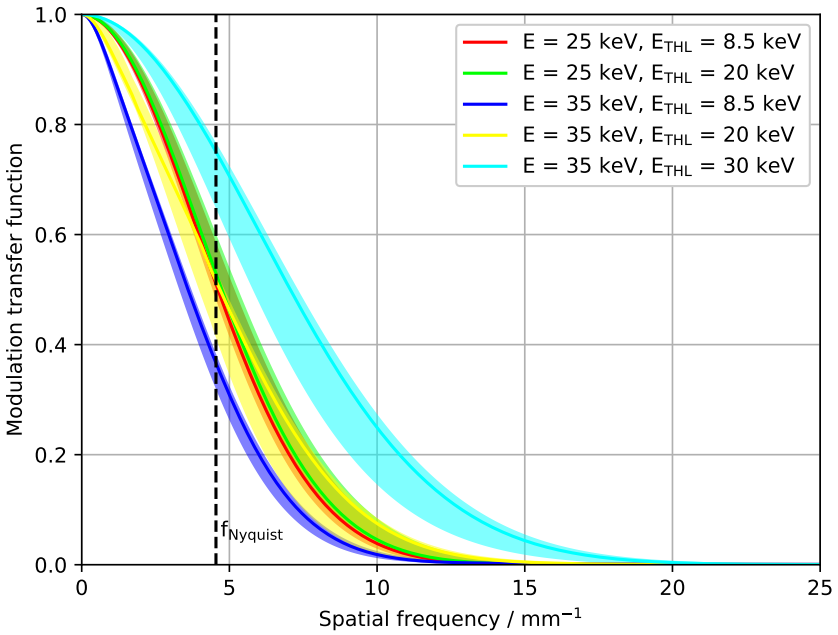

Figure 3.9.: MTF_{pre} of CdTe detector with 110 µm pixel pitch for different energy thresholds and photon energies in single pixel mode. The colored areas denote 95% confidence intervals.

operation modes SPM and CSM. These different resulting curves are shown in figure 3.9 and figure 3.10.

The SPM shows the same behaviour as the Timepix detector, since the effects of charge collection are the same as in the Timepix. The MTF_{pre} improves for higher energy thresholds, since the events, that are highly charge shared are neglected by the detector.

In the case of the CSM, the MTF_{pre} is not significantly different for the different energy thresholds, since most of the photon charges are reconstructed correctly and not so many charge shared photons are omitted by the electronic readout. This leads to a worse MTF_{pre} that is no longer dependent on the energy threshold. For the photons of 35 keV, that are above the K-edges of CdTe result in a worse MTF, since the fluorescence photons cannot always be recovered by the charge summing mode (see energy response functions in section 3.1). Just the measurement with an energy threshold of 30 keV, where all photons that interact with adjacent pixels are neglected, results in an improved MTF_{pre}.

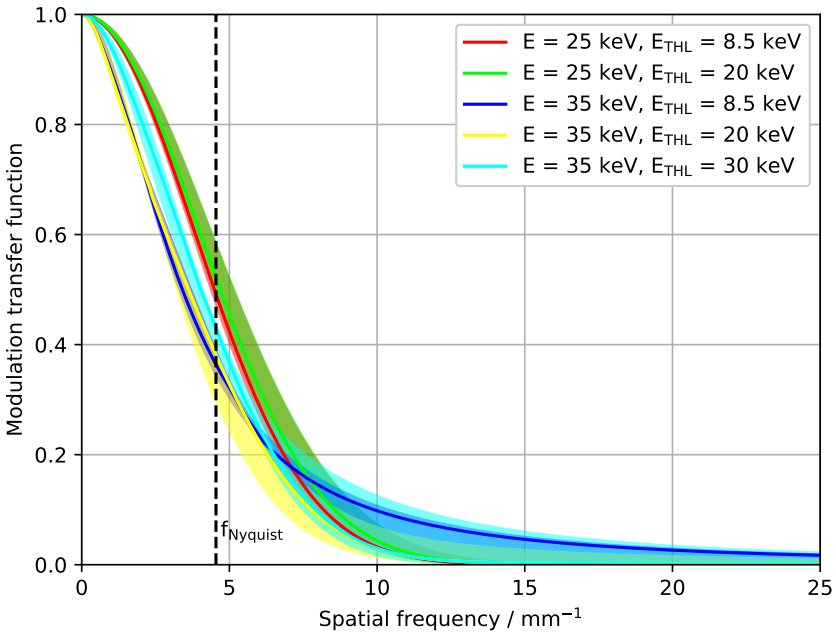

Figure 3.10.: MTF_{pre} of CdTe detector with 110 µm pixel pitch for different energy thresholds and photon energies in charge summing mode. The colored areas denote 95% confidence intervals.

Also, the MTF_{pre} is worse for CdTe than for the silicon sensor. This is caused by the larger charge diffusion in the thicker sensor. The production of the compound semiconductor also induces more crystal defects than the silicon production. These crystal defects also lead to a more scattered charge cloud, leading to a worse MTF_{pre}.

The MTF_{pre} is for both Si and CdTe above 35% at the Nyquist frequency. Therefore, the pixel size is not limiting the spatial resolution of the detector assembly and the full imaging system. One also need to keep in the mind, that the presence of frequencies higher than the Nyquist frequency can lead to aliasing in the recorded images.

3.3. Detective Quantum Efficiency

Beside the spectral and spatial resolution, described in the sections above, the detective quantum efficiency (DQE) is an important measure, how a detector system reacts on noise. In this section, I measure the DQE(0) for different operation modes of the Medipix3RX detector.

The detective quantum efficiency (DQE) denotes how the signal-to-noise ratio of an incoming intensity propagates through the detection system. For the case of Poisson distributed incoming photons the DQE can be expressed as

$$\mathrm{DQE}(\nu) = \frac{\mathrm{SNR}^2_{\mathrm{out}}(\nu)}{\mathrm{SNR}^2_{\mathrm{in}}(\nu)}, \tag{3.4}$$

the fraction between the squared detected signal-to-noise ratio (SNR) and the incoming squared signal-to-noise ratio.

For photon counting detectors it is possible to determine the zero frequency detective quantum efficiency (DQE(0)) by evaluating the distribution of the number of pixels that respond to a single photon interaction[Mic+06; DAM07]. The number of multiple hits, detected by a single photon interaction, is called multiplicity m. The DQE(0) is then given by

$$\mathrm{DQE}(0) = \frac{\langle m \rangle^2}{\langle m^2 \rangle} \varepsilon, \tag{3.5}$$

where $\langle m \rangle^2$ is the squared mean multiplicity and $\langle m^2 \rangle$ the mean of the squared multiplicity. ε is the absorption efficiency of the sensor material multiplied by the fraction of events that are detected by the detector. The latter compensates for the fact, that the detector becomes more and more inefficient for energy thresholds closer to the photon energy.

To measure the multiplicity, the detectors were exposed to radioactive sources and the exposure time was chosen in a way, that only sparse single events were detected. Afterwards, the recorded frames were processed by an algorithm, that detected the clusters of pixels that detected photons. The algorithm checks for each recorded frame all pixels, that are counting, and combines all of those pixels to clusters, that are less separated than a defined radius. Since fluorescence photons can be created, that are able to travel more than one pixel before thy are absorbed again, a radius of 550 µm was used to combine the clusters. To omit interactions of cosmic particles, all events with a size of more than 20 pixels are omitted.

For a 2 mm CdTe Medipix3RX detector (W103_C2) 5000 frames with an exposure time of 1 ms, each in CSM and SPM and for different energy threshold values, where recorded. The detector was exposed to 59.6 keV and 88 keV by using an ^{241}Am and a ^{109}Cd source. The low energy photons of these sources, and their decay products, were suppressed by filtering them with copper and aluminum filters.

In figure 3.11 the average multiplicity is shown for the scan with the cadmium source. For the SPM the multiplicity drops all along with raising energy thresholds. In the CSM case one can clearly see, the crossing of the CdTe fluorescence energies around 25 keV. One can also see, that the total values are much smaller up to the energy of the impinging photons. This arises from the fact, that two adjacent pixels are always reconstructed by the CSM into one pixel.

The resulting DQE(0) values are shown in figure 3.12 for both photon energies.

For the charge summing mode, the DQE(0) stays longer at a high value, since fewer events are lost due to the energy threshold. This is important for the application of photon counting detectors for spectroscopic imaging, where multiple energy thresholds are employed. Also, the charge summing mode clearly outperforms the single pixel mode.

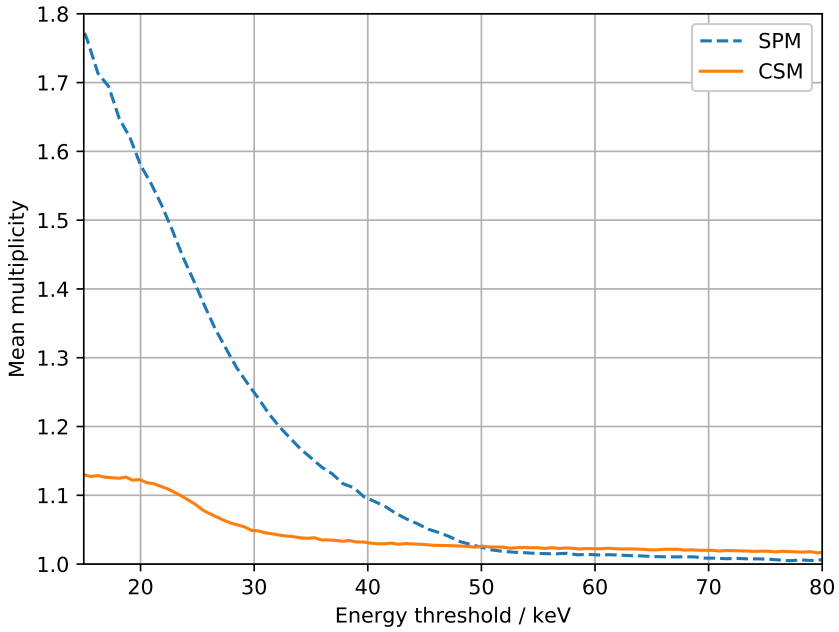

Figure 3.11.: Measured multiplicity dependent on the energy threshold for a photon energy of 59.6 keV in charge summing mode and single pixel mode measured with a Medipix3RX detector with a 2 mm thick CdTe sensor.

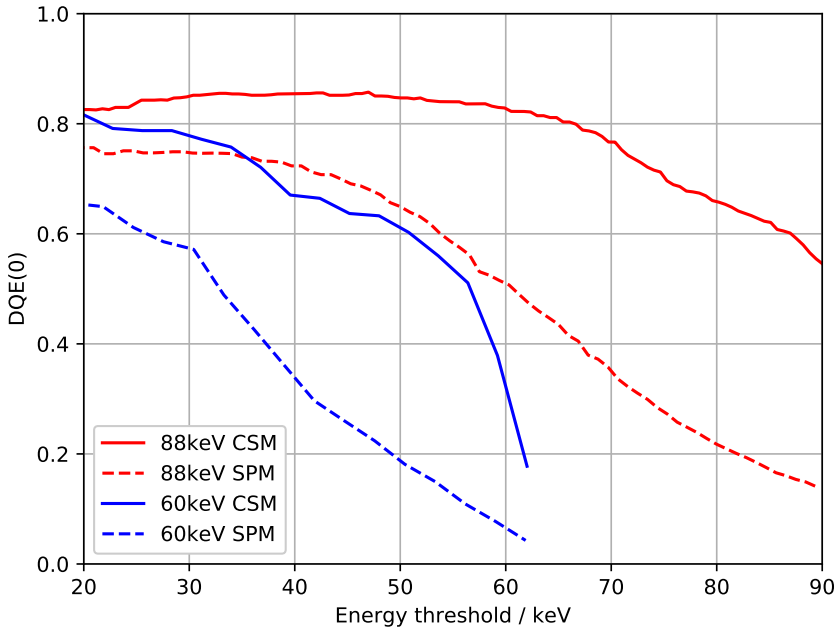

Figure 3.12.: DQE(0) for different photon energies and operation modes. The DQE(0) was measured with a Medipix3RX detector with a 2 mm thick CdTe sensor.

3.4. Sensor Material Influence Onto Spectroscopic Imaging Performance

Sensor materials with a high atomic number are more efficient due to more imperfections in the crystal structure for compound semiconductor materials they also introduce a larger leakage current. The Medipix Detector features an adjustable leakage current compensation. This allows to evaluate the quality of spectroscopic CT data-sets depending on the leakage current compensation, sensor material (CZT and CdTe) and the presence of external temperature variation. The results lead to a more optimized setup for spectroscopic imaging, and show the presence of short strong leakage current pulses in CdTe induced by temperature changes.

In the following measurements Medipix3RX detectors, based on CdTe and CZT sensor, are employed. Since a wide range of energy bins are required for the analysis a high stopping power (see figure 3.2) over the full range of energy thresholds is required. Due to the energy of the absorption edges of the utilized contrast agents, such a large energy range is required. Due to the limited energy resolution of the medipix devices (approximately 5 keV to 8 keV, see section 3.1) the energy bins need to be distributed over a few tens of keVs. Therefore, silicon based devices, which are available in a very high quality due to the well established silicon processing, were not used here due to the low attenuation in the higher energy range.

The detailed method of spectroscopic CT is described in the section 5.4. In this part, we assume, that we have an established method, that yields material specific images. The effects on the material specific images will now be used as a proxy to determine the performance of the detector system under different conditions.

The resistivity of a semiconductor, and therefore the resulting leakage current, is dependent on the temperature of the sensor. In this section an AC (ambient temperature and air conditioning) was used to control the ambient temperature of the experimental hutch. Since the AC controller switches on when exceeding a certain temperature and switching off the AC when reaching a lower temperature a periodically fluctuating ambient temperature is present when the measurements were performed. By completely disabling the AC a higher but much more stable temperature can be achieved.

The enabled AC results in a lower temperature of the detector, but with temperature oscillations of $\approx 2\,^{\circ}\mathrm{C}$. Without the AC the mean temperature is higher and changes slightly over time, but no fast changes of the temperature are present. The measured temperature, while a CT scan was performed and the resulting leakage current are shown in figure 3.13 and 3.14. One can see, that the leakage current for CdTe is larger that for CZT and that both materials show periodical changes in the magnitude of the leakage current, caused by the changing temperature. The temperature was measured with an infrared thermometer, that pointed at the backside of the readout PCB of the two employed Medipix detector assemblies. The exact positioning of the thermometer can lead to a systematic error in the absolute value of the energy.

The resistivity of a semiconductor is depending on its temperature. Therefore, the changing temperature leads to a changing leakage current, that runs through the Medipix detector and the sensor material.

To investigate the temperature and leakage current influences onto material spe-

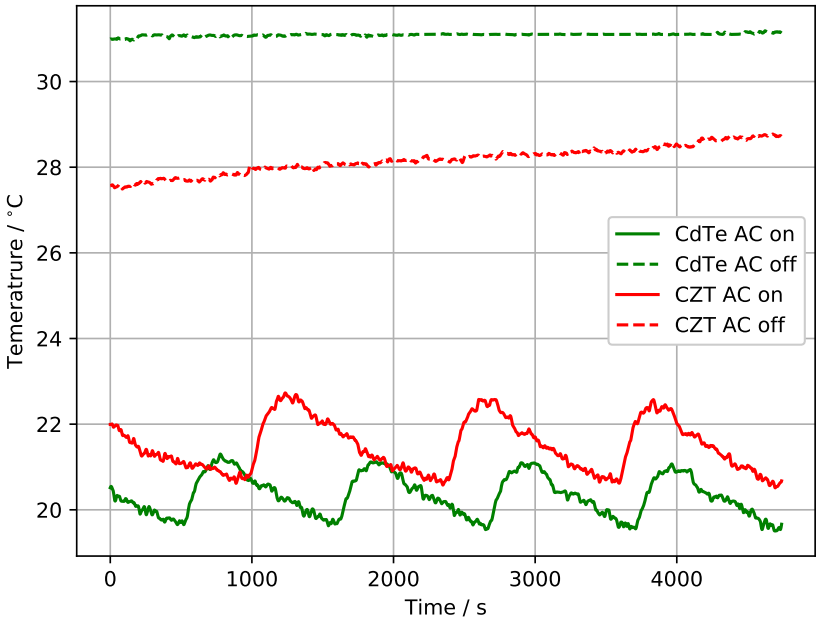

Figure 3.13.: Temperature of medipix (backside of PCB) with and without air conditioning that induces temperature variations.

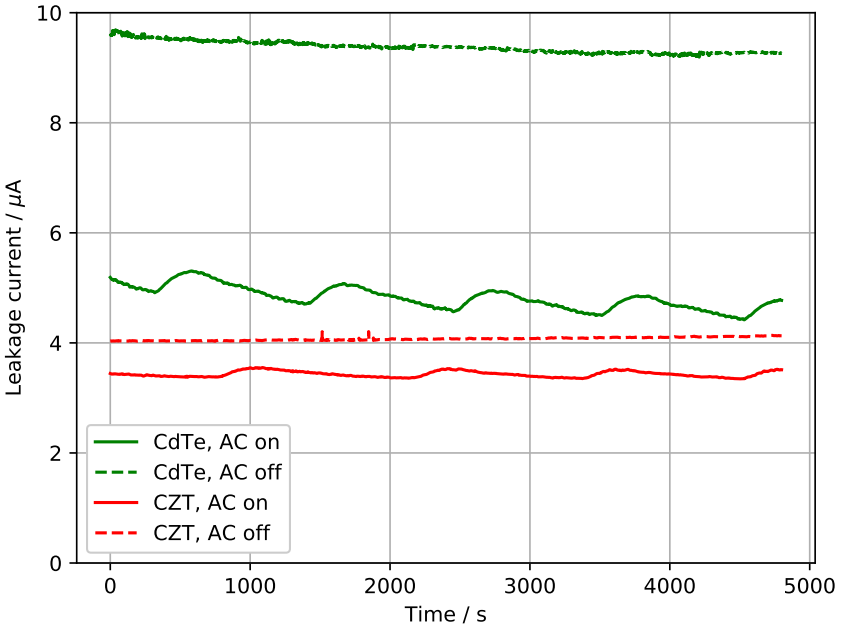

Figure 3.14.: Measured total leakage current for CdTe and CZT assembles under different temperature conditions.

cific spectroscopic CT imaging, CT measurements were performed for CdTe and CZT with and without enabled AC for different magnitudes of leakage current compensations in the Medipix3RX detector.

The leakage current compensation of the Medipix3RX was operated with I_{Krum} values of 4.68 nA, 11.7 nA and 23.4 nA, resulting in a maximum leakage current compensation per pixel of 2.34 nA, 5.85 nA and 11.7 nA.

The CT slices (before the material decomposition was applied) for CdTe with an enabled AC show streak artefacts for the lowest leakage current compensation. In the measurement with the highest leakage current compensation these artefacts disappear. The corresponding CT slices are shown in figure 3.15.

Projection images of the two extreme settings of the leakage current compensation are shown in figure 3.16. Three types of artifacts are visible, probably originated in crystal defects in sensor material. Artefact A is an area with a very low count rate (and therefore a high attenuation is shown). This artefact shrinks when the leakage current compensation is increased. The artefact B is an area with a high count rate and artefact C with low count rate. Both completely disappear for the increased leakage current compensation.

Pixels, that are always counting an extremely high or low value are compensated by the CT reconstruction algorithm. Therefore, the intensity drops, that change over time are creating the artefacts in the reconstructed CT slices.

The count rate of such a pixel close to artefact C is shown in figure 3.19. In addition, the count rate of a pixel in an area far away of a defect is plotted as well. When the leakage current compensation is increased, the drops are disappearing and the signal is stable over the whole measurement. In figure 3.20 no more drops in the count rate are observed.

Those artefacts are caused by a shortly dropping count rate in some pixels.

This leads to the conclusion, that the leakage current is increased for a short time when the temperature changes in the sensor and the leakage current compensation is no longer able to handle the leakage current.

This means, that it is possible to suppress the artefacts, caused by leakage currents, by increasing the leakage current compensation. However, the increased I_{Krum} also influences the spectroscopic performance of the detector. To investigate the influences onto spectroscopic CT full material decomposition was performed for the presence of temperature changes, different I_{Krum} values and the two sensor materials. The slices with the strong streak artefacts were excluded from the analysis. For the different basis materials (water-equivalent, Gd and I) the contrast-to-noise ratio (CNR) was calculated for the regions in the CT slices, that could easily be assigned to the basis materials.

$$\mathrm{CNR} = \frac{|\mu_1 - \mu_2|}{\sqrt{\sigma_1^2 + \sigma_2^2}} \tag{3.6}$$

The borders inbetween the different regions were neglected. As a reference the air region was used for all the materials.

The contrast to noise ratio between the air part of the sample and for the iodine part has been calculated and is shown in figure 3.17 and 3.18 for varying and stable temperature, respectively.

The main differences are, that CdTe suffers more under the temperature changes, while CZT is not dependent on the temperature changes. Even since CZT has a

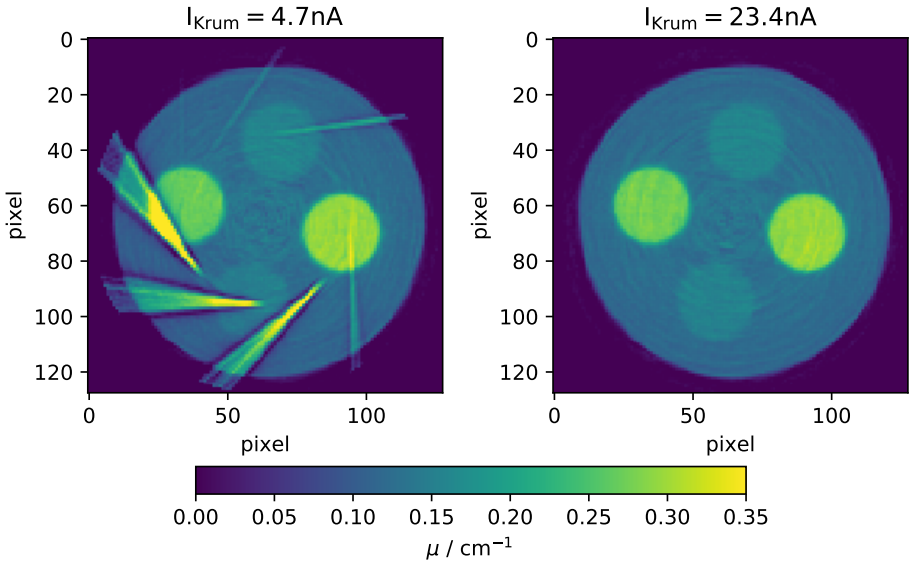

Figure 3.15.: Reconstructed CT slices, located close to the region of the artefact C marked in figure 3.16. The energy threshold of this CT slice was set to 28 keV.

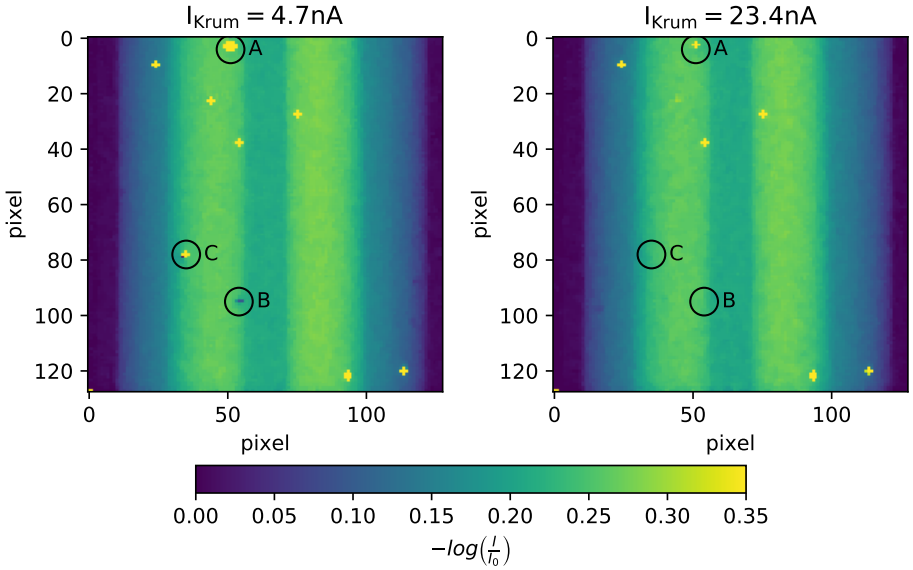

Figure 3.16.: Projection images of the specimens for different leakage current compensations. The markings denote different types of defects.

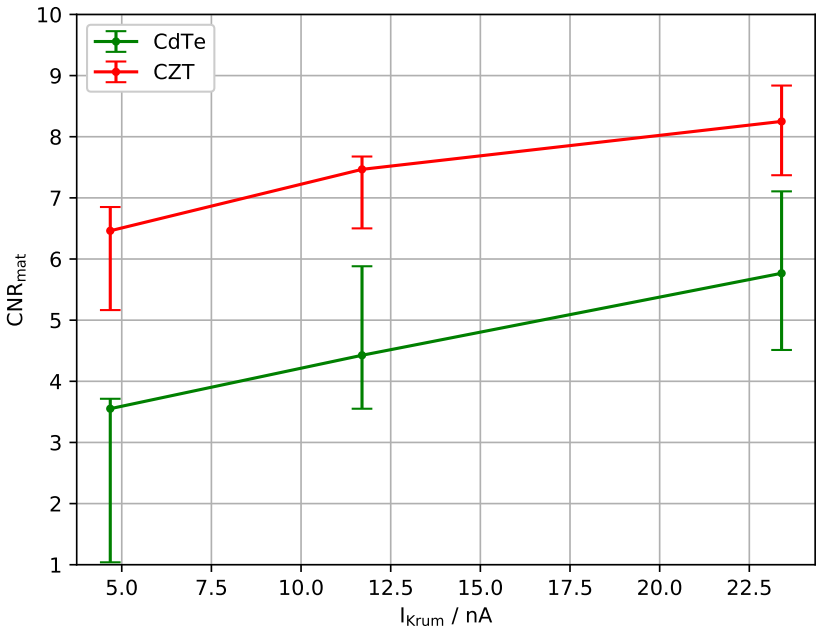

Figure 3.17.: Measured CNR of the reconstructed iodine basis material with enabled AC.

much higher leakage current, the leakage current compensation can handle the CZT better than the CdTe. This can be caused by fast changes in the leakage current in the CdTe due to a change of temperature[Zub+15]. However, when the leakage current compensation if optimized for the task, the differences between the two materials are no longer significant.

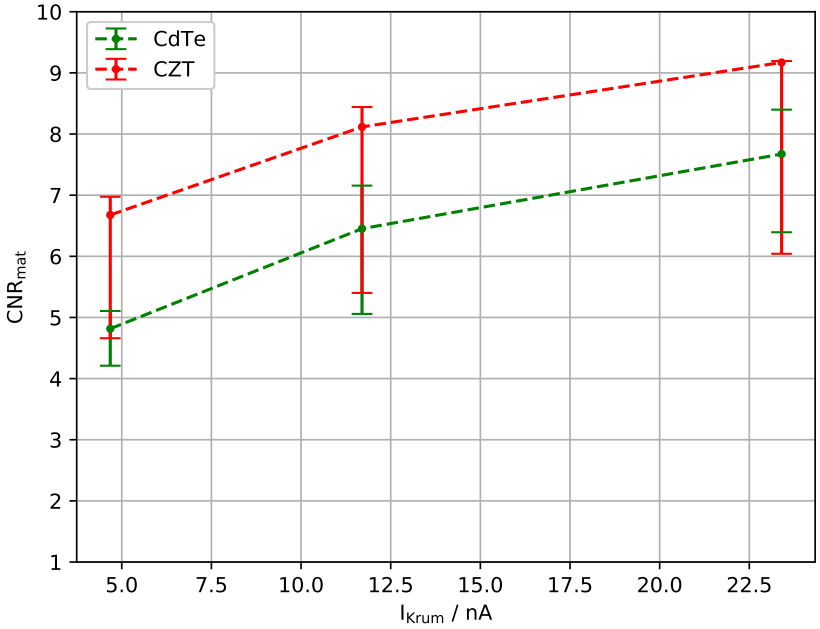

Figure 3.18.: Measured CNR of the reconstructed iodine basis material with disabled AC.

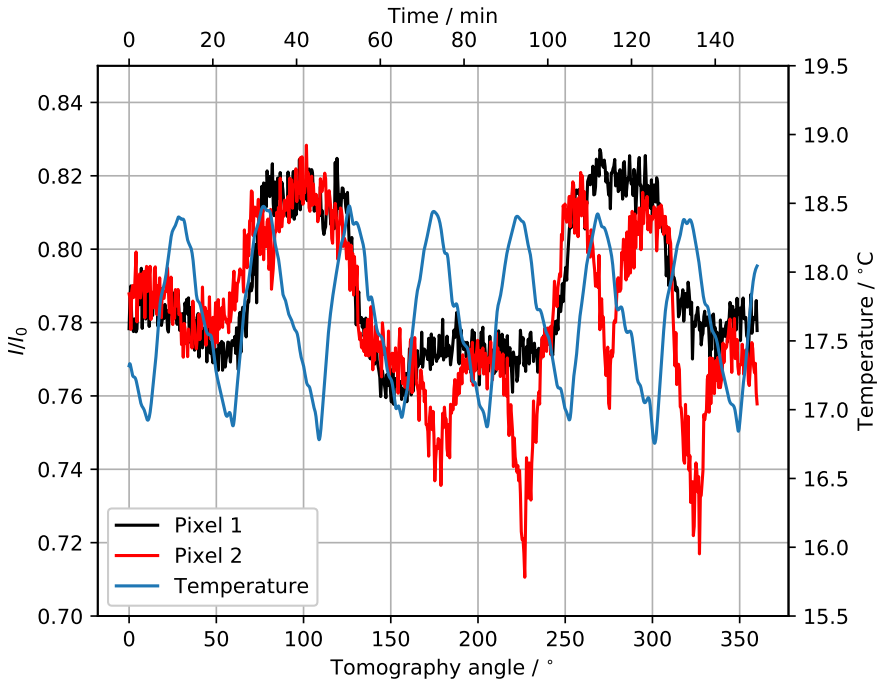

Figure 3.19.: Measured pixel intensity and temperature. Pixel 2 is close to an artefact, Pixel 1 is in a non-effected region close by.

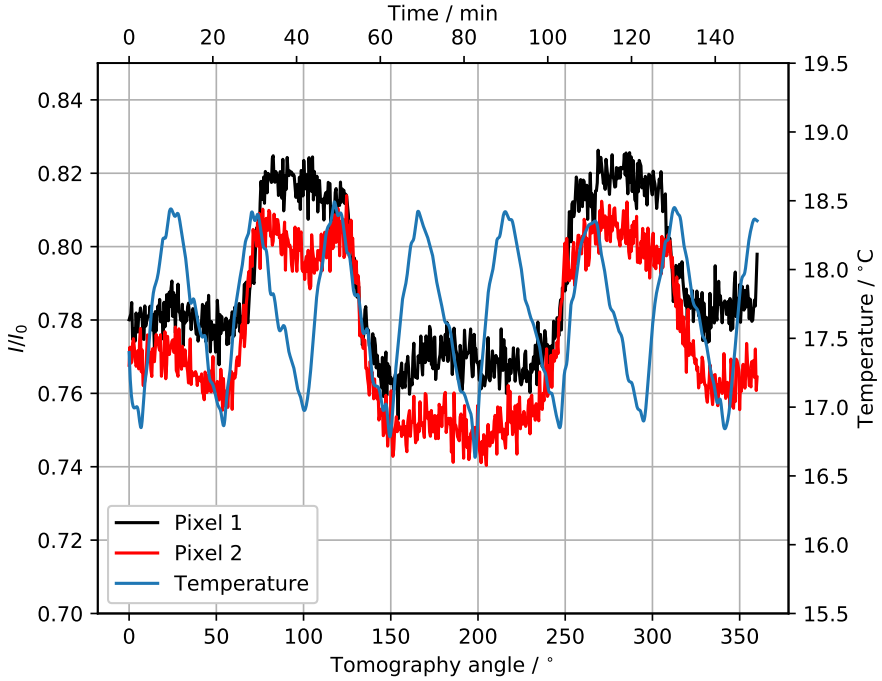

Figure 3.20.: As figure 3.19, but with increased leakage current compensation.

3.5. Summary

In this chapter Timepix and Medipix3RX detector assemblies attached to different semiconductor sensors were characterized by evaluating the energy resolution, the spatial resolution, the detective quantum efficiency and the image quality at different temperature environments. While the energy resolution, spatial resolution and noise properties are well suited for spectral CT, in an un-optimized configuration the CdTe sensors suffer from temperature variations. By optimizing the detector settings, these issues could be suppressed to a non-significant difference to the CZT sensor material. Many findings from this chapter lead to decisions on features of the next generation of Medipix detectors. The poor availability, small size and complexity to operate these devices makes it difficult to use them in many applications. However, I could demonstrate that in general these detectors have unique and promising features for X-ray imaging.

4. Contrast Mechanisms and Image Formation

The laboratory setup is intended to be a platform for research of image formation with X-rays as well as a platform to develop specific applications with X-rays. In this section I describe the formation of the different X-ray contrasts. For the grating based phase contrast imaging, I examined the potentials and limitations of this method.

In this part the theoretical backgrounds for X-ray wave propagation in vacuum and in media are derived from the Maxwell equations. This part is mostly based on the chapter 1.1 and 2.1 of the book [Pag06] and assumes monochromatic radiation, allowing to neglect the frequency dependence of the interacting matter. For a polychromatic illumination and the assumption of a harmonic time dependence, the wave propagation can be described analogous to the monochromatic case by introducing the complex frequency dependent vector fields $\vec{E}(\vec{r},\omega)$, $\vec{H}(\vec{r},\omega)$, $\vec{D}(\vec{r},\omega)$ and $\vec{B}(\vec{r},\omega)$, which is described in detail in [KH09; Man19].

Starting from the Maxwell equations

$$\nabla \cdot \vec{D}(\vec{r},t) = \rho(\vec{r},t) \tag{4.1}$$

$$\nabla \cdot \vec{B}(\vec{r},t) = 0 \tag{4.2}$$

$$\nabla \times \vec{E}(\vec{r},t) = -\frac{\partial \vec{B}(\vec{r},t)}{\partial t} \tag{4.3}$$

$$\nabla \times \vec{H}(\vec{r},t) = \vec{J}(\vec{r},t) + \frac{\partial \vec{D}(\vec{r},t)}{\partial t} \tag{4.4}$$

with the time and space dependent vector fields $\vec{H}$, $\vec{B}$, $\vec{E}$, $\vec{D}$.

The electric displacement $\vec{D}(\vec{r},t)$ and magnetic field $\vec{B}(\vec{r},t)$ are given by

$$\vec{D}(\vec{r},t) = \varepsilon_0 \vec{E}(\vec{r},t) + \vec{P}(\vec{r},t) \tag{4.5}$$

$$\vec{B}(\vec{r},t) = \mu_0 \vec{H}(\vec{r},t) + \vec{M}(\vec{r},t) \tag{4.6}$$

with the polarization $\vec{P}$ and the magnetic material response $\vec{M}$.

In the case of a linear and isotropic material, which can be assumed or all effects in this thesis, these material equations can be simplified as

$$\vec{D}(\vec{r},t) = \varepsilon \vec{E}(\vec{r},t) \tag{4.7}$$

$$\vec{B}(\vec{r},t) = \mu \vec{H}(\vec{r},t), \tag{4.8}$$

with ε and μ only space depended.

By combining 4.1 and 4.4 we get

$$\nabla \left(\nabla \times \vec{H}(\vec{r},t) \right) = \nabla \left(\vec{J}(\vec{r},t) + \frac{\partial \vec{D}(\vec{r},t)}{\partial t} \right) = \nabla \vec{J}(\vec{r},t) + \frac{\partial}{\partial t} \rho(\vec{r}) = 0. \tag{4.9}$$

By applying a rotation to 4.3 we get

$$\nabla \times \nabla \times \vec{E}(\vec{r},t) = -\frac{\partial}{\partial t}\nabla \times \vec{B}(\vec{r},t) \tag{4.10}$$

$$\nabla(\nabla\vec{E}) - \Delta\vec{E}(\vec{r},t) = -\frac{\partial}{\partial t}\nabla \times \vec{B}(\vec{r},t) \tag{4.11}$$

By filling in the material equation 4.8 in 4.4 we get

$$\nabla \times \left(\frac{1}{\mu}\vec{B}(\vec{r},t)\right) = \vec{J}(\vec{r},t) + \frac{\partial}{\partial t}\varepsilon\vec{E}(\vec{r},t) \tag{4.12}$$

$$\frac{1}{\mu}\nabla \times \vec{B}(\vec{r},t) + \left(\nabla\frac{1}{\mu} \times \vec{B}(\vec{r},t)\right) = \vec{J}(\vec{r},t) + \frac{\partial}{\partial t}\varepsilon\vec{E}(\vec{r},t) \tag{4.13}$$

By the combination of 4.11 and 4.13 we get

$$\nabla\left(\nabla\vec{E}(\vec{r},t)\right) - \Delta\vec{E}(\vec{r},t) + \frac{\partial}{\partial t}\left(\mu\frac{\partial}{\partial t}(\varepsilon\vec{E}(\vec{r},t)) + \mu\vec{J}(\vec{r},t) - \mu\nabla\frac{1}{\mu} \times \vec{B}(\vec{r},t)\right) = 0 \tag{4.14}$$

$$\nabla\left(\nabla\vec{E}(\vec{r},t)\right) - \Delta\vec{E}(\vec{r},t) + \frac{\partial}{\partial t}\mu\frac{\partial}{\partial t}(\varepsilon\vec{E}(\vec{r},t)) + \frac{\partial}{\partial t}\mu\vec{J}(\vec{r},t)\frac{\partial}{\partial t}\left(\nabla\ln\mu \times \vec{B}(\vec{r},t)\right) = 0 \tag{4.15}$$

By the assumption of a time independent ε and μ we get

$$\left(\varepsilon\mu\frac{\partial^2}{\partial t^2} - \Delta\right)\vec{E}(\vec{r},t) - \nabla\ln\mu \times \nabla \times \vec{E}(\vec{r},t) + \nabla(\nabla\vec{E}(\vec{r},t)) + \mu\frac{\partial}{\partial t}\vec{J}(\vec{r},t) = 0. \tag{4.16}$$

In the following parts the so called d'Alembert equations are derived for different cases.

Vacuum case: In vacuum we have $\varepsilon = \varepsilon_0$ and $\mu = \mu_0$ and not currents and sources are present, so we can set $\rho = 0$ and $\vec{J}(\vec{r},t) = 0$. This results in the d'Allemberts for vacuum:

$$\left(\varepsilon_0\mu_0\frac{\partial^2}{\partial t^2} - \Delta\right)\vec{E}(r,t) = 0 \tag{4.17}$$

$$\left(\varepsilon_0\mu_0\frac{\partial^2}{\partial t^2} - \Delta\right)\vec{H}(r,t) = 0 \tag{4.18}$$

Source free in matter: If we assume an (inhomogeneous) medium without free sources and currents we can set $\vec{J}(\vec{r},t) = 0$, $\rho(\vec{r}) = 0$, $\varepsilon(\vec{r}) = \varepsilon_r(\vec{r})\varepsilon_0$ and $\mu(\vec{r}) = \mu_r(\vec{r})\mu_0$. This results in these d'Allembert equations:

$$\left(\varepsilon_0\mu_0\frac{\partial^2}{\partial t^2} - \Delta\right)\vec{E}(\vec{r},t) + \nabla(\nabla\vec{E}) - \nabla\ln\mu(r) \times \nabla \times \vec{E}(\vec{r},t) = 0 \tag{4.19}$$

$$\left(\varepsilon_0\mu_0\frac{\partial^2}{\partial t^2} - \Delta\right)\vec{H}(\vec{r},t) + \nabla(\nabla\vec{H}) - \frac{1}{\varepsilon(r)}\left(\nabla\varepsilon(r) \times \nabla \times \vec{H}(\vec{r},t)\right) = 0 \tag{4.20}$$

Homogeneous medium: In a homogeneous medium we have $\varepsilon = \varepsilon_0$ and $\mu = \mu_0$ and not currents and sources $\rho(\vec{r}) = 0$, $\vec{J}(\vec{r}, t) = 0$.

$$\left(\varepsilon\mu\frac{\partial^2}{\partial t^2} - \Delta\right)\vec{E}(r,t) = 0 \tag{4.21}$$

$$\left(\varepsilon\mu\frac{\partial^2}{\partial t^2} - \Delta\right)\vec{H}(r,t) = 0 \tag{4.22}$$

$$\tag{4.23}$$

Inhomogeneous non-magnetic medium without sources: For an inhomogeneous medium without sources we get these assumptions: $\mu \approx \mu_0$, $\vec{J}(\vec{r}, t) = 0$, $\rho = 0$, $\varepsilon(\vec{r}) = \varepsilon_r(\vec{r})\varepsilon_0$.

$$\left(\varepsilon(\vec{r})\mu_0\frac{\partial^2}{\partial t^2} - \Delta\right)\vec{E}(\vec{r},t) + \nabla(\nabla\vec{E}(\vec{r},t)) = 0 \tag{4.24}$$

$$\left(\varepsilon(\vec{r})\mu_0\frac{\partial^2}{\partial t^2} - \Delta\right)\vec{H}(\vec{r},t) - \frac{1}{\varepsilon(\vec{r})}\nabla\ln\varepsilon(\vec{r}) \times (\nabla \times \vec{H}(\vec{r},t)) = 0 \tag{4.25}$$

By the assumption of only slowly varying compared to the wavelength we get

$$\left(\varepsilon(\vec{r})\mu_0\frac{\partial^2}{\partial t^2} - \Delta\right)\vec{E}(\vec{r},t) = 0 \tag{4.26}$$

$$\left(\varepsilon(\vec{r})\mu_0\frac{\partial^2}{\partial t^2} - \Delta\right)\vec{H}(\vec{r},t) = 0. \tag{4.27}$$

Due to the absence of any mixing of both formulas for electric and magnetic field we can handle them as a scalar (typically the electric field is identified with the scalar).

$$\left(\varepsilon(\vec{r})\mu_0\frac{\partial^2}{\partial t^2} - \Delta\right)\Psi(\vec{r},t) = 0 \tag{4.28}$$

With the spectral decomposition of the field Ψ in its monochromatic components Ψ_ω we get

$$\Psi(\vec{r},t) = \frac{1}{\sqrt{2\pi}}\int_{-\infty}^{\infty}\psi_\omega(\vec{r})e^{-i\omega t}d\omega. \tag{4.29}$$

By combining the spectral decomposition with the formula 4.28 we get

$$\left(\Delta + \varepsilon_\omega(\vec{r})\mu_0 c^2 k^2\right)\psi_\omega(\vec{r}) = 0 \tag{4.30}$$

with $\omega = ck$ and the ω dependent electrical permittivity ε_ω.

By introducing the ω dependent refractive index $n_\omega(\vec{r}) = \sqrt{\frac{\varepsilon_\omega(\vec{r})}{\varepsilon_0}}$ and $k = 2\pi/\lambda$ we get

$$\left(\Delta + \left(\frac{2\pi}{\lambda/(c\sqrt{\varepsilon_\omega(\vec{r})\mu_0})}\right)\right)\psi_\omega(\vec{r}) = 0 \tag{4.31}$$

and resulting in the so-called inhomogeneous Helmholtz equation

$$\left(\Delta + k^2 n_\omega^2(\vec{r})\right)\psi_\omega(\vec{r}) = 0. \tag{4.32}$$

The interaction of X-rays with matter can be split into attenuation, refraction and interference, and scatter.

The introduction of a complex refractive index, allows to combine the attenuation of a wave and the phase shift induced by a material, into a single material property.

The complex refractive index n is given by

$$n = 1 - \delta + i\beta, \tag{4.33}$$

with δ denoting the phase shift of the wave and β the attenuation[AM11].

The linear mass attenuation coefficient μ can be extracted from β with the wave-vector k:

$$\mu = 2k\beta \tag{4.34}$$

The δ can be written as

$$\delta = \frac{2\pi r_0 \rho_e}{k^2} = \frac{e^2\rho_e}{2\epsilon_0 m_e c^2 k^2}, \tag{4.35}$$

with ρ_e electron density, r_0 classic electron radius and m_e the electron mass.

This is valid for free electrons with k values not to close to an absorption edge.

A plane wave in vacuum can be described as

$$\psi(\vec{r}) = E_0 e^{in\vec{k}\vec{r}} \tag{4.36}$$

with the magnitude of the electric filed E_0 and n corresponding to a homogeneous material. Since n is equal to one in vacuum the plane wave can be written as

$$\psi(\vec{r}) = E_0 e^{i\vec{k}\vec{r}}. \tag{4.37}$$

By comparing the two formulas for vacuum and a homogeneous material, it follows for a material with the thickness of d that the intensity, that corresponds to Φ^2 is given by

$$I = E_0 \left|e^{-\beta k d}\right|^2 = I_0 e^{-\mu d} \tag{4.38}$$

and the phase shift of

$$\Delta\phi = \delta\vec{k}\vec{r}. \tag{4.39}$$

After X-rays were discovered, the thickness and material dependent attenuation was immediately used for imaging with films and fluorescence screens. In the initial publication of Röntgen[Rön95] he described the attenuation as thickness dependent and that heavier materials also attenuate stronger than lighter materials. Röntgen also tried to measure if X-rays are refracted by prisms and lenses and also tried to detect interference effects. However, due to the small deviation of the refractive indices these effects were too small to be detected in this time.

4.1. X-ray Absorption Contrast

The attenuation coefficient μ (see equation 4.34) can be split in components of photoelectric absorption, compton scattering and pair-production. For pair production photon energies above twice the electron energy (511 keV) are required. Since this is way above the energies applied in this thesis, it will be neglected.

$$\mu = \mu_{\text{pe}} + \mu_{\text{cs}} \tag{4.40}$$

4.1.1. Photoelectric absorption

In the photoelectric absorption process, the incoming photon interacts with a bound electron. If the photon energy (E_γ) is higher than the binding energy of the electron, the electron can be liberated completely from the atom or can be raised to a higher shell. Since the binding energy of an electron is depending on the atomic number Z, also the attenuation coefficient for photoelectric absorption is depending on on Z.

The attenuation coefficient for photoelectric absorption is proportional to

$$\mu_{\text{pe}} \propto \rho_e \frac{Z^m}{E_\gamma^3}, \tag{4.41}$$

with the electron density ρ_e and m between three and four, depending on the atomic mass [SB02]. Higher Z result in larger values of m.

With this proportionality, one can see, that this process is most pronounced for low energies and becomes stronger for heavy elements.

4.1.2. Compton scattering

Compton scattering is an inelastic process, where parts of the photon energy E_γ is transferred to an electron. This results in a photon with an increased energy and an outgoing photon with reduced energy.

The change in the wave length of the photon (and the energy) can be described with the conservation of energy and momentum resulting in [AM11]

$$\Delta\lambda = \lambda_c(1 - \cos\theta), \tag{4.42}$$

with the scattering angle θ and the compton scattering length

$$\lambda_c = \frac{h}{m_e c} = 3.86 \times 10^{-3}\,\text{A}. \tag{4.43}$$

The attenuation coefficient is proportional to the inverse of the photon energy [SB02]

$$\mu_{cs} \propto \frac{1}{E_\gamma}. \tag{4.44}$$

4.1.3. Interaction of photons with detector systems

X-rays were quickly used for medical imaging with films and fluorescence screens.

For the case, where only absorption is present, the intensity of the radiation I at the position (x, y, z), with an initial intensity distribution $I(x, y, z = 0)$, is given by

$$I(x, y, z) = \exp\left(\int_{z'=0}^{z} -g(x, y, z')dz'\right) I(x, y, z = 0) \tag{4.45}$$

$$\frac{I(x, y, z)}{I(x, y, z = 0)} = \exp(-\mu T(x, y)) \tag{4.46}$$

with the object function $g(x, y, z)$, the linear mass attenuation coefficient μ and the projected thickness of the object $T(x, y)$ for any z larger than the object thickness for an object with constant μ.

The beer lambert law (equation 4.46) gives the relative intensity after passing through an object with the projected thickness T.

The attenuation is energy dependent. If the sample is exposed to a polychromatic beam, always an averaged attenuation coefficient is measured.

$s(E)$ is the energy spectrum of the source (see figure 2.5 and figure 2.4). The spectrum after the beam passed the specimen is given by

$$s_{\text{sample}}(E) = s(E)e^{-\int \mu(E,z)\,\mathrm{d}z}. \tag{4.47}$$

The absorbed signal in the sensitive sensor layer is given by

$$s_{\text{detector}} = \int \left(1 - e^{-\mu_{\text{sensor}}(E)d}\right) s_{\text{sample}}(E)\,\mathrm{d}E. \tag{4.48}$$

For the energy integrating detector

$$\frac{I}{I_0} = \frac{\int \eta(E) \left(1 - e^{-\mu_{\text{sensor}}(E)d}\right) s(E)e^{-\int \mu(E,z)\,\mathrm{d}z}\,\mathrm{d}E}{\int \eta(E) \left(1 - e^{-\mu_{\text{sensor}}(E)d}\right) s(E)\,\mathrm{d}E} \tag{4.49}$$

with the light yield $\eta(E)$, which is typically proportional to the energy E. Therefore, the detected signal is proportional to the amount of the total absorbed energy. $\eta(E)\left(1 - e^{-\mu_{\text{sensor}}(E)d}\right)$ is plotted for the employed energy integrating detectors in figure 2.8.

For photon counting

$$\frac{I}{I_0} = \frac{\int\limits_{\text{disc.}} \left(1 - e^{-\mu_{\text{sensor}}(E)d}\right) s(E)e^{-\int \mu(E,z)\,\mathrm{d}z}\,\mathrm{d}E}{\int\limits_{\text{disc.}} \left(1 - e^{-\mu_{\text{sensor}}(E)d}\right) s(E)\,\mathrm{d}E} \tag{4.50}$$

all photons are contributing equally to the output signal. Also, the signal is directly the amount of detected photons without any additional conversion. The signal also includes no dark current. Therefore, there is no difference in recording multiple short exposed images and summing them up in post-processing or recording a single

long exposed image. Only a dead-time due to the readout could make a difference in the experimental protocol.

The projected thickness of the sample is given by

$$-\log\frac{I}{I_0} = \int \hat{\mu(z)}\rho(z)\,\mathrm{d}z \tag{4.51}$$

if the spectrum is not changed significantly by the sample.

In this case the logarithm can be moved inside the integral

$$\int \hat{\mu}\rho\,\mathrm{d}z = \frac{\int\limits_{\text{disc.}} \left(1 - e^{-\mu_{\text{sensor}}(E)d}\right) s(E) \int \mu(E)\,\mathrm{d}z\,\mathrm{d}E}{\int\limits_{\text{disc.}} \left(1 - e^{-\mu_{\text{sensor}}(E)d}\right) s(E)\,\mathrm{d}E} \tag{4.52}$$

This will allow to perform the spectroscopic CT algorithm (see 5.4) on the reconstructed CT slices if the spectrum is not significantly changed by the specimen.

4.2. Phase Contrast

The possibility to measure not only the X-ray mass attenuation, but also the X-ray refractive index of a material and the visibility (scattering) contrast completes the X-ray laboratory to be able to measure all the interactions of X-rays with matter. To measure these properties of the wave field optical elements are introduced to the X-ray beam. These optical elements interact with the X-ray beam in a well understood way and by evaluating the X-ray beam after adding a sample one can calculate the influences of the sample onto the wave field.

Already in 1985 Röntgen tried to measure if X-rays can contribute to interference and refraction [Rön95]. However, he was not able to detect any of such effects. This was due to the small difference of the refractive index of typical materials and the vacuum (or air). The angular difference of a refracted beam is typically bellow a few µrad (corresponds to a few mm per km propagation), which was not detectable by Röntgen.

4.2.1. Refractive Index Decrement and Principles of Wave Propagation

The δ of the refractive index is called refractive index decrement and is used to describe the elastic scattering of an object. In the elastic process the energy of the photon is not changed, but the propagation direction is changed. For a material without absorption this leads to the Sells law

$$n_1 \sin(\alpha_1) = n_2 \sin(\alpha_2). \tag{4.53}$$

The following description of wave propagation is based on the book [Pag06].

Due to the Huygens-Fresnel principle a propagated wave front can be described as an interfering superposition of single waves. For a plane wave (parallel beam) this leads to a solution of the Helmholtz equation

$$\Psi(\vec{r}) = \Psi(x, y, z) = \exp\left(i(k_x x + k_y y + k_z z)\right). \tag{4.54}$$

Assuming only propagation in positive z this can be rewritten as

$$\Psi(x,y,z) = \exp\left(i(k_x x + k_y y)\right) \exp\left(iz\sqrt{k^2 - k_x^2 - k_y^2}\right) \tag{4.55}$$

with $k^2 = k_x^2 + k_y^2 + k_z^2$. The second part ($\exp\left(iz\sqrt{k^2 - k_x^2 - k_y^2}\right)$) is called free-space propagator and describes the propagation over z.

The composition of the propagated wave out of plane waves with different k can be seen as a Fourier series. In real-space the propagated wave can be described by the incoming wave, convoluted with the free-space propagator.

$$\psi(x,y,z=\Delta) = \mathcal{F}^{-1}\left(\exp\left(i\Delta\sqrt{k^2 - k_x^2 - k_y^2}\right)\mathcal{F}\left(\psi(x,y,z=0)\right)\right) \tag{4.56}$$

With this the propagator D_Δ can be defined as, where Δ denotes the propagation distance.

$$D_\Delta = \mathcal{F}^{-1} \exp\left(i\Delta\sqrt{k^2 - k_x^2 - k_y^2}\right)\mathcal{F} \tag{4.57}$$

When assuming only small angles components in the plane wave, relatively to the propagation direction, k_z can be approximated as (paraxial approximation):

$$k_z = \sqrt{k^2 - k_x^2 - k_y^2} \approx k - \frac{k_x^2 + k_y^2}{2k}. \tag{4.58}$$

With this approximation the propagator D_Δ can be transformed in the Fresnel propagator D_Δ^F:

$$D_\Delta^F = \exp(ik\Delta)\mathcal{F}^{-1}\left(\exp\left(\frac{-i\Delta(k_x^2 + k_y^2)}{2k}\right)\right)\mathcal{F} \tag{4.59}$$

This propagator, that is valid for parallel beam illumination can be extended for a conical beam by so-called Fresnel scaling. For this we assume that a point like monochromatic source is located at the distance r_s in front af the sample. The detector is located at the distance r_d behind the sample, which corresponds to the propagation distance Δ. When the distance r_s is significantly larger than the sample size, we can assume a paraxial illumination of the sample. In this case the projection approximation is valid and the Fresnel propagator can be used. The geometrical magnification can be given by

$$M = \frac{r_s + r_d}{r_s}. \tag{4.60}$$

The Fresnel scaling theorem [Pag06] states, that in a divergent beam that diffraction pattern at the propagation distance Δ is equivalent to the plane wave case at the distance Δ/M.

The adjusted Fresnel propagator $D_z^{F,c}$ is given by

$$D_\Delta^{F,c} = \exp(ik\Delta/M)\mathcal{F}^{-1}\left(\exp\left(\frac{-i\Delta(k_x^2 + k_y^2)}{2kM}\right)\right)\mathcal{F}. \tag{4.61}$$

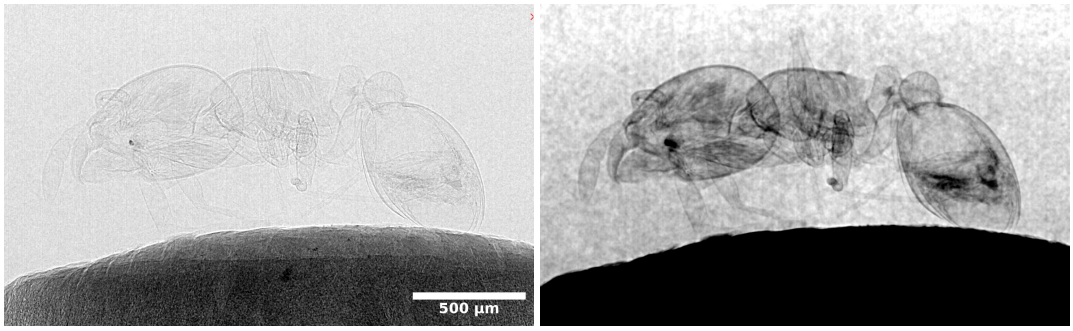

(a) Flat field corrected projection image.

(b) Retrieved sample function using the ufo-filters implementation ([Far+22]) of [Pag+02].

Figure 4.1.: Projection image of an ant and the retrieved sample function.

This results that for higher magnifications, the interference patterns move more close to the sample. In addition to the changed propagator, the initial (conical) wave ψ^c needs to be adjusted, according the spherical waves emitted form the source

$$\psi(x, y, z = 0)^c = \psi(x, y, z) \exp\left(\frac{ik}{2r_s}\left(x^2 + y^2\right)\right). \tag{4.62}$$

Also the intensity (down-scaled by M^2) and the magnification (by M) needs to be taken into account.

4.2.2. Propagation-Based Phase Contrast

When a sample is illuminated with a coherent source, the wave front is disturbed by the sample. When this disturbance propagates over a distance Δ, the wave front is changed, resulting in a change in intensities (as described in equation 4.61).

With the source size of 0.8 µm and propagation distances of up to 1.7 m the propagation results in an edge-enhancement effect and overshoots at the edges of the sample.

To reconstruct the original sample, the propagation needs to be inverted. However, since the detectors only measure the intensity, the phase information is lost in some way. Multiple approaches have been proposed to reconstruct the phase information, e.g. by [Pag+02] which is the most suited for the presented geometry and coherence of this laboratory.

As an example an ant has been imaged with the presented setup, utilizing a large propagation distance and a small source size. The specimen was placed 12 mm away from the source and the propagation distance was 1497 mm. The X-ray tube was operated with an acceleration voltage of 50 kV and a source size of 0.8 µm. The physical pixel size of the detector was 200 µm.

In figure 4.1a the projection image of the ant is shown. The retrieved sample function is shown in figure 4.1b. For the phase retrieval the ufo-filters implementation of [Pag+02] was used.

4.2.3. Experimental Method: Grating Interferometry

To measure the attenuation and the phase shift of a sample with a detector that features large pixels, and therefore also a large field of view, a Talbot-interferometer can be employed[Mom+03]. In such an interferometer, typically one-dimensional gratings are employed.

The phase grating induces a periodical phase shift onto the incoming wave field. While this new wave field propagates the phase shifts are transferred into intensity shifts at defined positions, the so-called fractional talbot distances (equation 4.63[Sul97; LKJ05]). This interference pattern has the same pattern as the phase shift, however it is magnified by the conical beam geometry and can be scaled by half depending on the strength of the phase shift.

For a parallel beam configuration the fractional Talbot distance d_T (for any integer m) and the distances to get an interference pattern is given by

$$d_{T_n} = m\frac{p_1^2}{2\lambda\eta^2} \tag{4.63}$$

with the pitches of the grating p_0, p_1, p_2 of the source grating G_0, phase grating G_1 and the analyzer grating G_2, respectively. η is given by

$$\eta = \begin{cases} 1 & \text{for } \pi/2 \text{ phase shift in the phase grating} \\ 2 & \text{for } \pi \text{ phase shift in the phase grating.} \end{cases} \tag{4.64}$$

The different distances are denoted in figure 4.2.

For a cone beam setup, the talbot distance d_T gets scaled by the magnification (eqn. 4.63). Also, the distances and periodicity of the grating need to be selected as shown in equations 4.63.

With he magnification (of the grating) M, given by

$$M = \frac{L + d_{T_n}}{L} \tag{4.65}$$

the fractional Talbot order is scaled to

$$d'_{T_n} = M \cdot d_{T_n}. \tag{4.66}$$

Since also the interference pattern is magnified by the conical beam, the pitch of the analyzer grating needs to match the periodicity of the self image:

$$p_2 = M \cdot p_1/\eta \tag{4.67}$$

For a source, that features a coherence lower than the required one to create the interference pattern at the analyzer grating an additional grating G_0 can be introduced. This splits the incoherent source into multiple sources, that are incoherent to each other, but within one sub-source there is enough coherence to create a pattern. The periodicity of the sub-sources needs to be chosen in a way, that the intensities of the interference patterns sum up at the analyzer grating. This periodicity is given by:

$$p_0 = \frac{p_2 L}{d'_{T_n}} \tag{4.68}$$

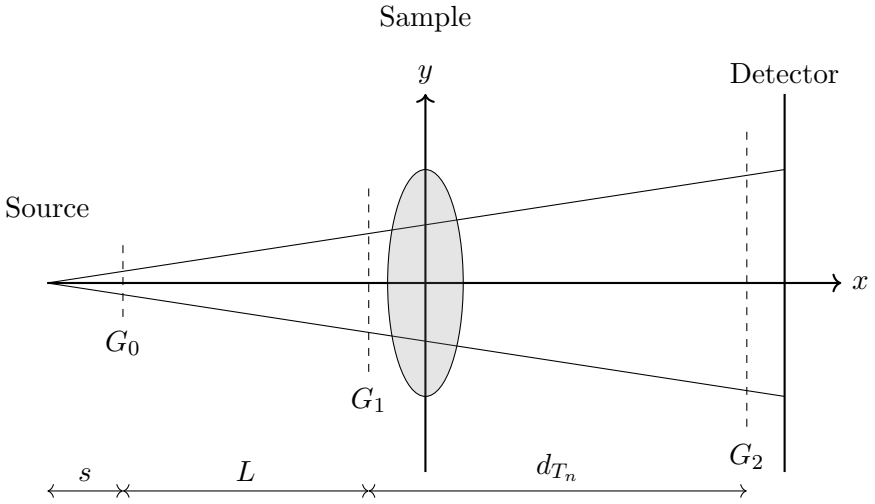

Figure 4.2.: Geometry definition for a talbot-lau interferometer (top view). In case of a talbot interferometer the source grating G_0 is not used.

Now any source size can create self images. However, each of the sub-sources is slightly shifted, which results in a blurring of the sample function.

A typical flat panel detector is not able to resolve these interference patterns. Therefore, an analyzer grating G_2 is introduced, that features the period of the talbot self-image at the position of G_2. By scanning this grating along the y axis, one can sample the finer interference pattern, that is not directly resolvable by the detector. However, one needs to keep in mind, that one detector pixel sees the average intensity of multiple lamella openings of G_2. Typically, grating pitches are in the order of 2 µm to 10 µm and detector pixel sized in the order of 50 µm to 200 µm. This results in at least 5 to 100 intensity patterns, that are summed in one pixel.

When now a sample is introduced, the sample can interact with the wave field via attenuation, refraction and scattering. These effects then change locally the intensity, the propagation distance, and therefore the local shape of the intensity pattern at G_2 or can reduce the local visibility.

In the normal case, one assumes that the sample does not introduce any interference effects and that the samples phase shift is only projected onto the self-image of the phase grating. However, if the sample is illuminated with a coherent source, there can be inference effects (starting with edge enhancement at the borders and more distributed interference patterns for large coherence length). The presence in of interference, where normally only a pure projection of the sample is assumed, can result in a wrong interpretation of the sample.

In case of a source, that features not enough coherence that an interference pattern develops at G_2, an additional absorption grating G_0 can be introduced. This grating now creates multiple small sources. Each of this source is located in a way, that the created intensity pattern at G_2 matches with the intensity patterns of the other sources. The wave fields of the different small sources are no longer coherent to each other, so they do not interfere. Only the intensities at the analyzer grating are summed up. A sketch of such an interferometer is shown in figure 4.2.

4.2.4. Measurement Protocol to Extract Absorption, Phase and Visibility

In grating interferometry the self pattern of the phase grating can not directly be resolved by a detector system for most of the imaging systems. Therefore, the analyzer grating is used to sample the pattern with higher resolution than the actual detector pixels.

The analyzer grating is moved multiple steps over a range of its pitch. In the case of an ideal self-image without the presence of an object this would result in a sinus signal in the measured intensity.

This sinus curve is changed by the sample. The differences in the mean values relate to the attenuation. A shift relates to a phase shift in the object and therefore a change in the local propagation distance. And a reduction of the amplitude can be caused by scattering or any other effect that influences the propagation of the wave. Such an intensity profile is shown in figure 4.3.

An easy way to process the data is based on a fourier transform of the intensity signal $I(x, y, p)$ of the different detector pixels x and y as well as the position of the analyzer grating p. The values of p are distributed over n_p number of stepping periods and n_s the number of steps per period. So p runs from 0 to $n_p * n_s - 1$.

$$\hat{a}_k = \sum_{p=0}^{n_p n_s - 1} e^{-2\pi i \frac{jk}{n_p * n_s} * I(x,y,p)} \tag{4.69}$$

The mean intensity I is then given by a_0. The amplitude of the curve v by $abs(a_{n_p})$ and the phase ϕ of the signal by $\arg(a_{n_p})$ (the complex argument).

By measuring the stepping curves twice, one time with the sample and one time without, the images can be corrected fo intensity and phase variations of the incoming beam. The corrected values for absorption contrast, phase and visibility reduction are given by:

$$\frac{I_1}{I_0} = \frac{a_1}{a_0} \tag{4.70}$$

$$\phi = \phi_1 - \phi_0 \tag{4.71}$$

$$d = \frac{v_1}{v_0} \tag{4.72}$$

I implemented these types of measurements in the laboratory setup, allowing easy measurements of single projection images of samples as well as performing computed tomography experiments of all three contrasts. The experiment class directly yields processed images of the attenuation, phase and visibility contrast, that can be used as single projection images, as well as input for standard CT reconstructions. These simple to handle automized measurement templates allow a simple evaluation of the imaging technique grating interferometry that is now followed in the next sections.

4.2.5. Absorption, Refraction and Scatter with Incoherent Sources Based on Grating Interferometry

The standard setups for grating interferometry (Talbot and Talbot-Lau) were implemented in the laboratory setup including the automatic data processing yielding

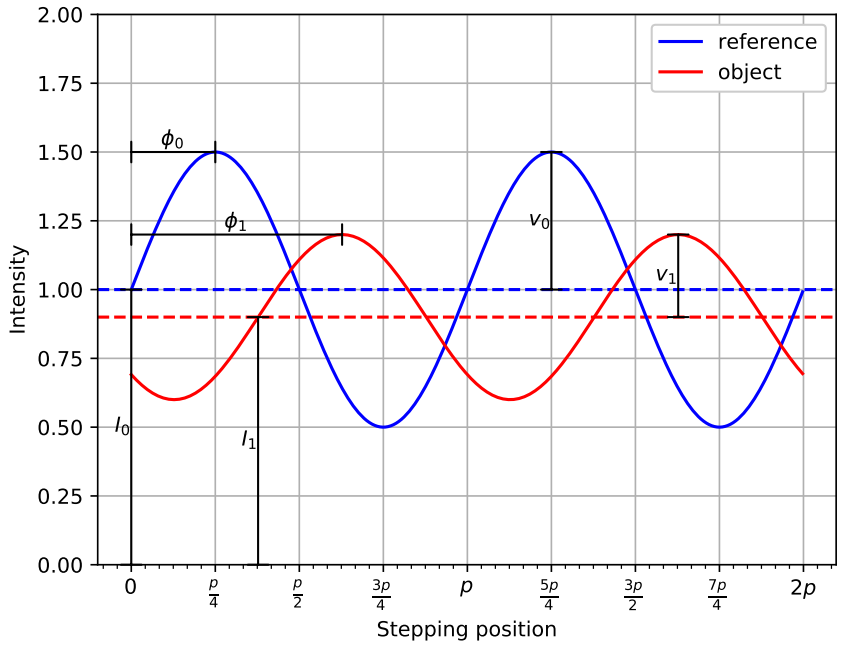

Figure 4.3.: Phase stepping intensity values of one pixel. X-axis in units of the analyser grating pitch p.

directly data of attenuation, phase shift and visibility. This makes the system also an ideal tool to examine grating interferometry as an X-ray imaging method. I demonstrated that it is also an ideal tool to characterize the quality of different grating designs including new grating layouts for large gratings allowing to optimize the grating production (see 6.6).

Interferometer setups can be implemented using two and three gratings. For the two grating setup (Talbot-interferometer), a small source size is required to achieve the required coherence and a source blurring small enough that the interference pattern is not washed out. In the case of the three grating setup (Talbot-Lau-interferometer), an additional grating is introduced, that splits the source in multiple small sources, that are not coherent to each other. But the positions of these multiple sources are arranged in a way, that the interference patterns of the different sub-sources are shifted by a multiple of the periodicity of the self-image.

The position of one grating is then scanned perpendicular to the beam to sample the intensity pattern in each pixel as described in section4.2. To demonstrate the process a Talbot-Lau-interferometer is set up.

Such a Talbot-Lau-interferometer implementation is shown in figure 4.4.

In this particular example implementation, as source grating a 120 µm high gold grating with a pitch of 4.8 µm was employed. To introduce the periodic phase shift a phase grating with a periodicity of 4.8 µm is used. The employed grating introduces a phase shift of π for photons of an energy of 40.5 keV. As analyzer grating another 120 µm high gold grating with a periodicity of 4.8 µm, matching the periodicity of the self-image is used.

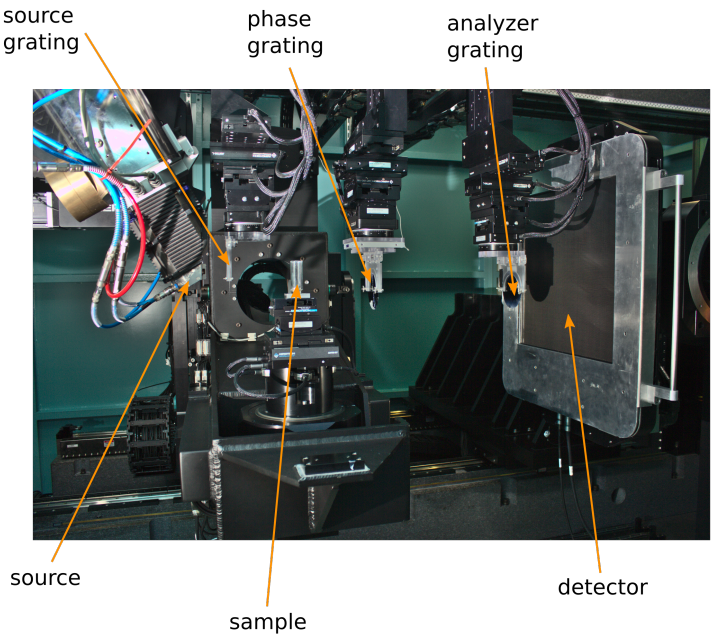

Figure 4.4.: Setup for grating interferometry radiography and tomography.

The source grating was placed 5 cm from the source. The distances between the source grating and the phase grating was set to 56.4 cm. Between the phase grating and the analyzer gratings the same distance was set up, resulting to measure in the third fractional talbot order.

The sample was placed 5 cm in front of the phase grating, resulting in a propagation distance of 61.4 cm to the analyzer grating.

The employed detector has a pixel pitch of 200 µm. Due to the geometrical magnification of 2.354 the effective pixel size was 84.94 µm.

The X-ray tube (in reflection geometry) was operated with an acceleration voltage of 70 kV and a target power of 75 W. Each frame was exposed for 1 s.

The pixel-wise fourier components were calculated and used to determine the transmission, differential phase shift and the visibility reduction of a test sample (pipe connector). The resulting contrast images are shown if figure 4.5.

One can see, that in regions with high attenuation the phase signal can no longer be extracted correctly. The visibility contrast shows also low values in the regions of high attenuation, but also the edges are showing higher contrast values.

The signal of a single pixel at different stepping positions, with and without the sample in the beam is shown in figure 4.6. Despite the noise in the signal, the periodicity, the amplitude reduction, the mean reduction and the shift is clearly visible.

A scatter plot of the different combinations of the signal (see figure 4.7) shows the independence of the pixel wise recovered contrasts. For a dependence of the contrasts the points would be located on a line.

As another example figure 4.8 shows the three contrasts for a sample, composed of a tube, filled with coffee powder, sugar and salt and two cotton swabs (left with

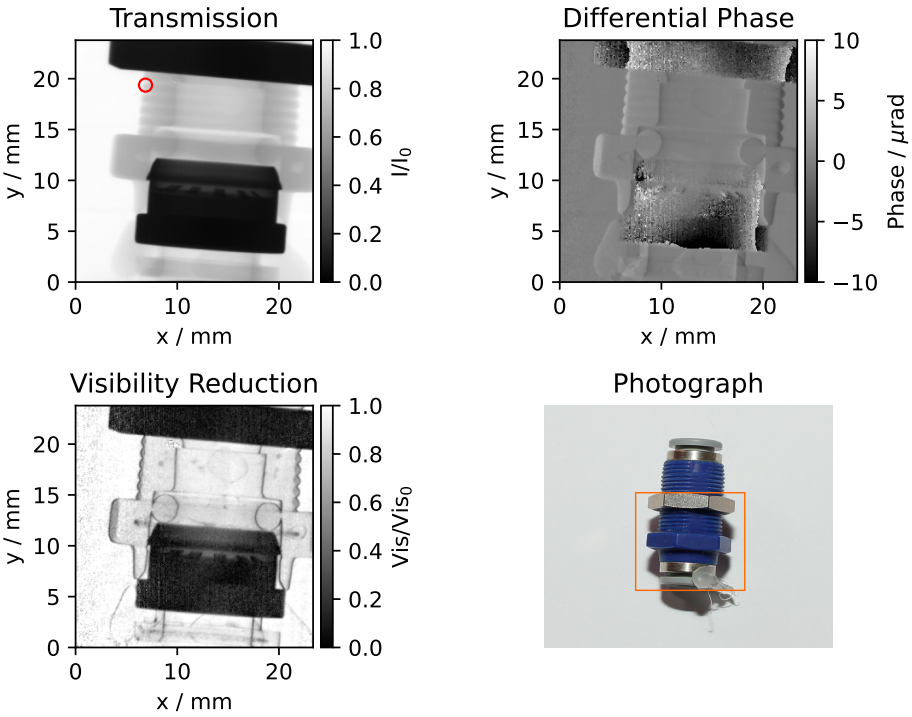

Figure 4.5.: Projection images of the different contrast modes in the grating based phase contrast imaging. The stepping curve of the red marked pixel is shown if figure 4.6.

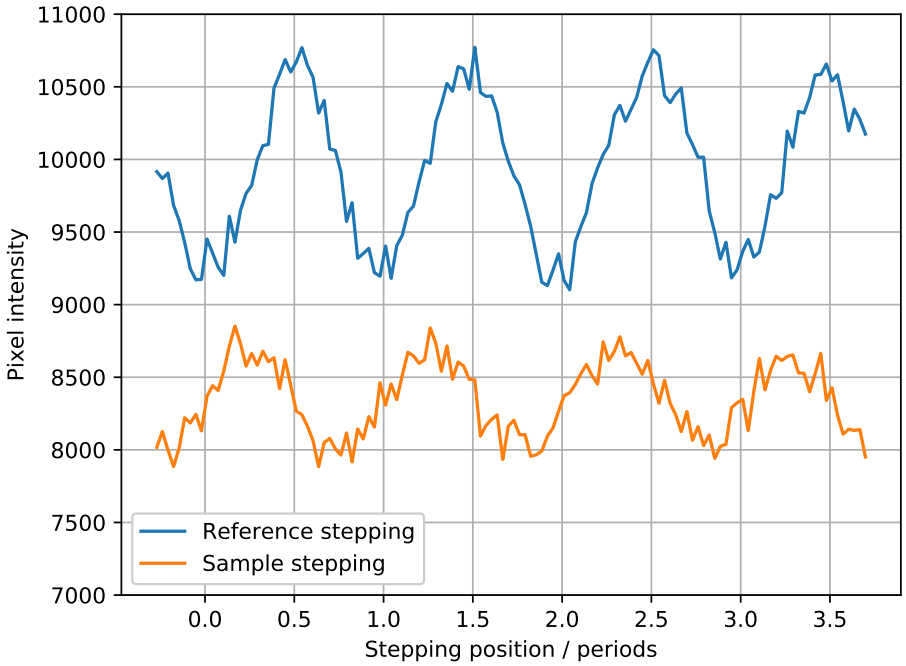

Figure 4.6.: Phase stepping curve. The analyzer grating was scanned over four periods with a sampling of 32 steps per period. The position of the pixel in the images is denoted by the red circle in figure 4.5.

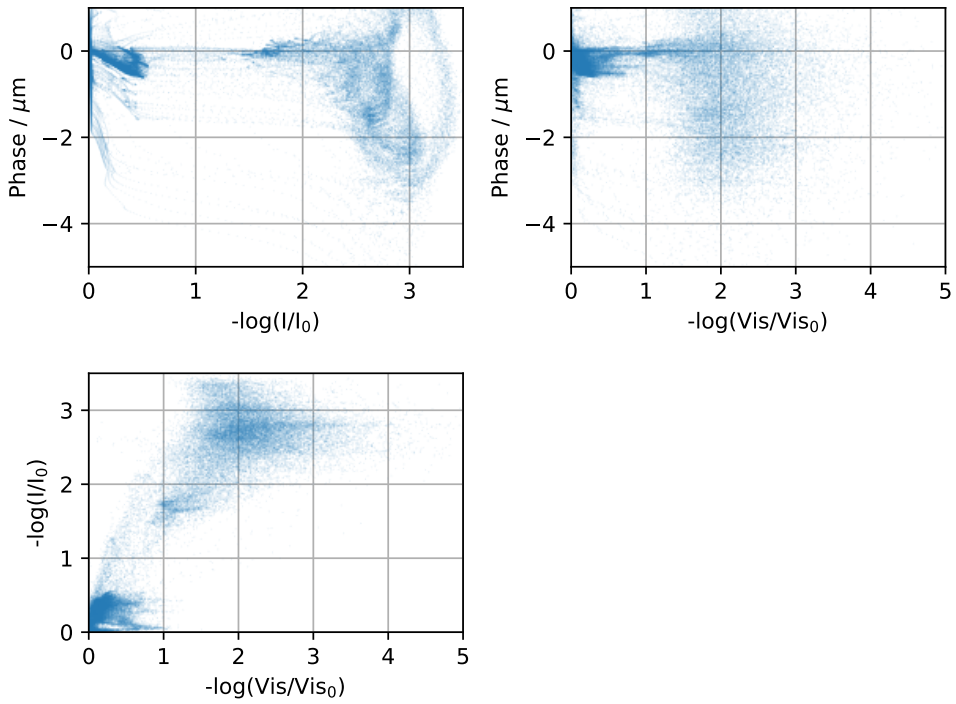

Figure 4.7.: Scatter plot for the different combinations of contrast modes. This illustrates the independence of the different contrasts.

plastic stick, right with wooden stick). In this example one can also see, a difference for the tree contrasts for the different materials.

A quantitative comparison with other established laboratories as not possible, due to the lack of a reference measurement protocol. However, when qualitatively comparing the results with other established laboratories from literature, the results are comparable. By optimizing the setup for certain applications, the results can often be improved.

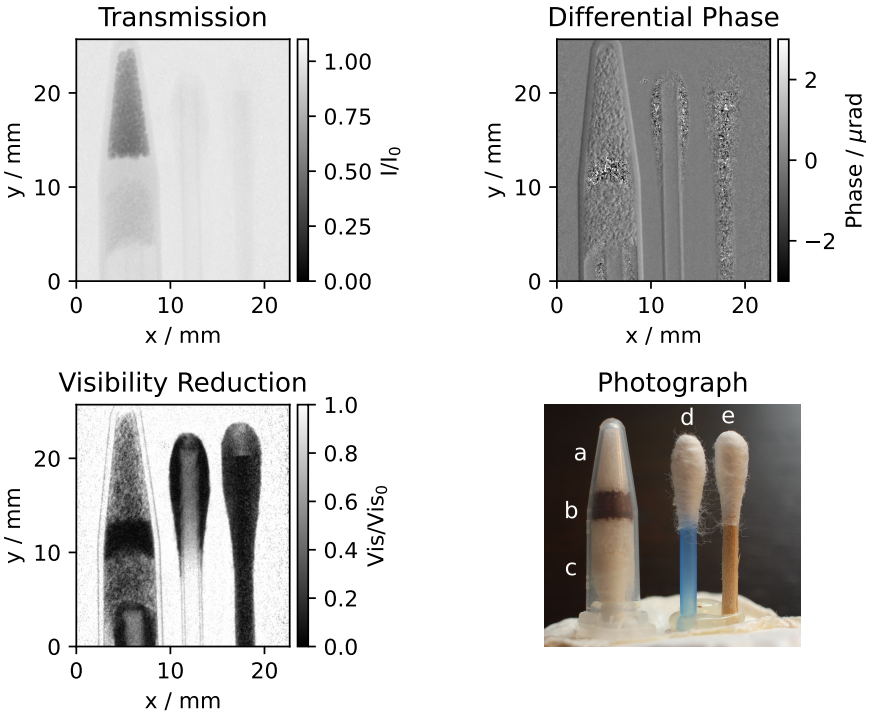

Figure 4.8.: Projection images of the different contrast modes in the grating based phase contrast imaging. The sample features a tube filled with salt (a), coffee powder (b) and sugar (c) and a cotton swab with plastic stick (d) and cotton swab with a plastic stick (e).

4.2.6. Photon Counting Detectors in Combination with X-ray Grating Interferometry

The Medipix detectors allow to adjust the sampling area per pixel without changing the pixel pitch (see section 3.2). With this feature the influences of the spatial sampling in grating interferometry can be examined. To evaluate the general applicability and comparability of the resulting images in grating interferometry, experiments were carried out at the synchrotron with a monochromatic and parallel beam. The results show a strong dependence between the normalized visibility and the point spread function when features are present that are close to the resolution limit of the detector system. This shows that the method of grating interferometry is highly dependent on the setup. The comparability between the reconstructed material properties is difficult and cannot be easily be normalized like with a Houndsfield calibration in normal absorption CT. These examinations allow to learn a lot about the image formation and which are the key features to optimize in such an imaging system.

Results of this section were published in [Koe+16].

The Medipix3RX detectors have a unique feature. They allow to change the sensitive area of a pixel while keeping the pixel pitch constant by introducing an unresponsive part at the pixel borders when operated in single pixel mode (SPM). Therefore, the MTF can be adjusted with the setting of the energy threshold (see section 3.2). The charge sharing, where parts of the deposited energy of an interacting photon is spread over multiple pixels, reduces the chance of a photon to be detected, when the threshold gets closer to the photon energy. When operated in charge summing mode (CSM), the energy threshold has no significant influence onto the presampling MTF.

To minimize the influence of the actual spectrum experiments were carried out with monochromatic radiation at the synchrotron. A 1.5 T bending magnet and a double multilayer monochromator feature a monochromatic beam with an energy bandwidth of $\frac{\Delta E}{E} = 1\%$ at an energy of 18 keV. The detector is an Medipix3RX featuring a 500 µm thick GaAs sensor with an intrinsic pixel pitch of 55 µm. The detector can be operated in CSM and SPM and the energy thresholds were set to 7 keV, 11 keV and 15 keV.

The presampling MTF was measured with the slanted edge method described in section 3.2[1] resulting in value σ for all the different detector settings.

This value corresponds to the size of a gaussian shaped point spread function. The values of the different σ values, dependent on the energy and the operation mode of the detector are shown in figure 4.9. One can see, that the values are significantly different for the different energies in the single pixel mode, while they do not show a significant deviation in the charge summing mode.

A two grating talbot interferometer, featuring phase and absorption gratings with pitches of 2.4 µm were used. The phase grating induced a $\pi/2$ phase shift for its design energy of 18 keV. The exposure time for the different settings of the detector were adjusted in a range of 0.2 s to 0.5 s to reach similar numbers of counts in the images. To minimize the influence of grating imperfections the grating was scanned over a region of 8 periods with 8 steps per period.

[1] data processing performed by Thomas König

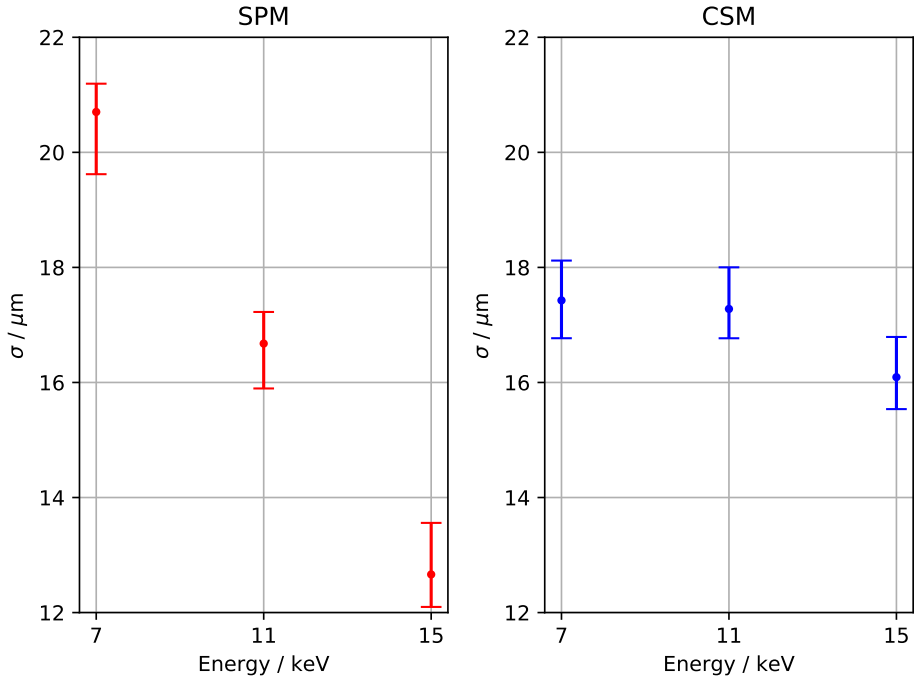

Figure 4.9.: Measured size of the energy threshold dependent effective point spread function. σ denotes the standard deviation of a gaussian shaped point spread function.

As a sample a rat lung, heart and trachea were used[2]. This sample features fine and porous structures in the region of the lung with feature sizes of a few 10 µm.

In the area of the heart the features are much more homogenous and does not have such fine structures.

The resulting images were processed with the fourier method, resulting in images for attenuation, phase shift and visibility. The resulting images for one set of detector settings is shown in figure 4.10.

The area a denotes a region of lung tissue, where no defects were located. The area b gives a region without any sample and the region c is a part of the heart tissue.

The median value of the visibility of the regions a and c, respectively, has been calculated and normalized by the air region, giving normalized visibilities for all sets of detector settings. The results for the lung is shown in figure 4.12 and for the heart in figure 4.11.

For the lung the normalized visibility shows a strong dependence to the point spread function in the SPM case. In the charge summing mode no significant influence is present.

In the area of the heart, where no small features are present, no dependence between the normalized visibility, and the point spread function can be discovered.

[2]sample courtesy University Saarland

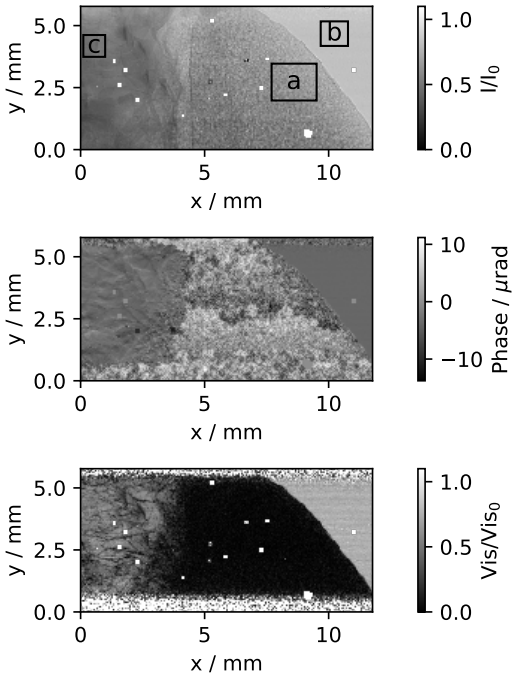

Figure 4.10.: Projection images of the sample in the three contrast modes. The area a marks the used region for the lung material, b for calibration with air and c the used heart region.

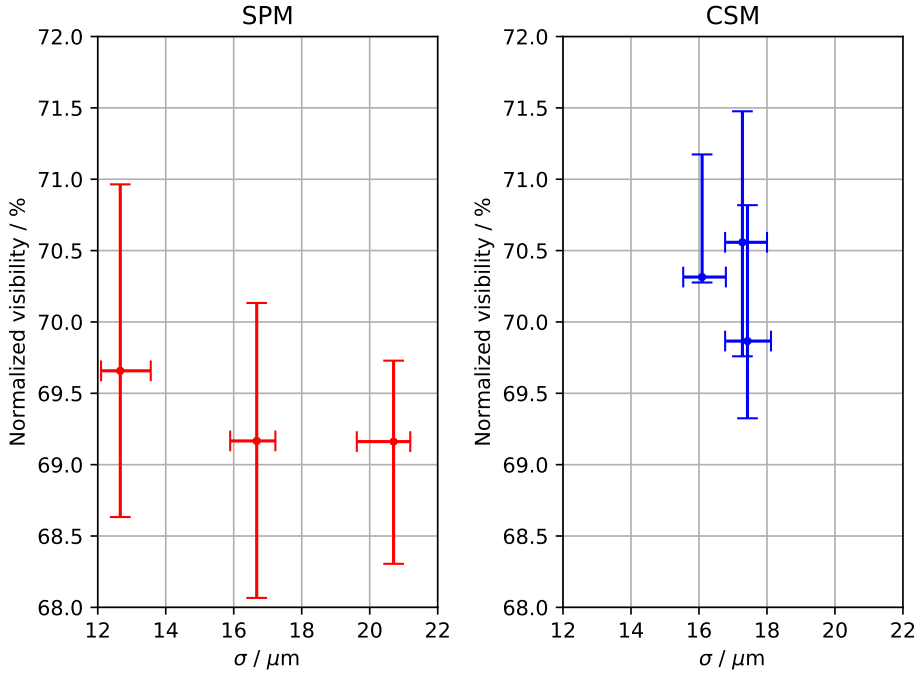

Figure 4.11.: The measured normalized visibility of the heart region for different effective point spread functions.

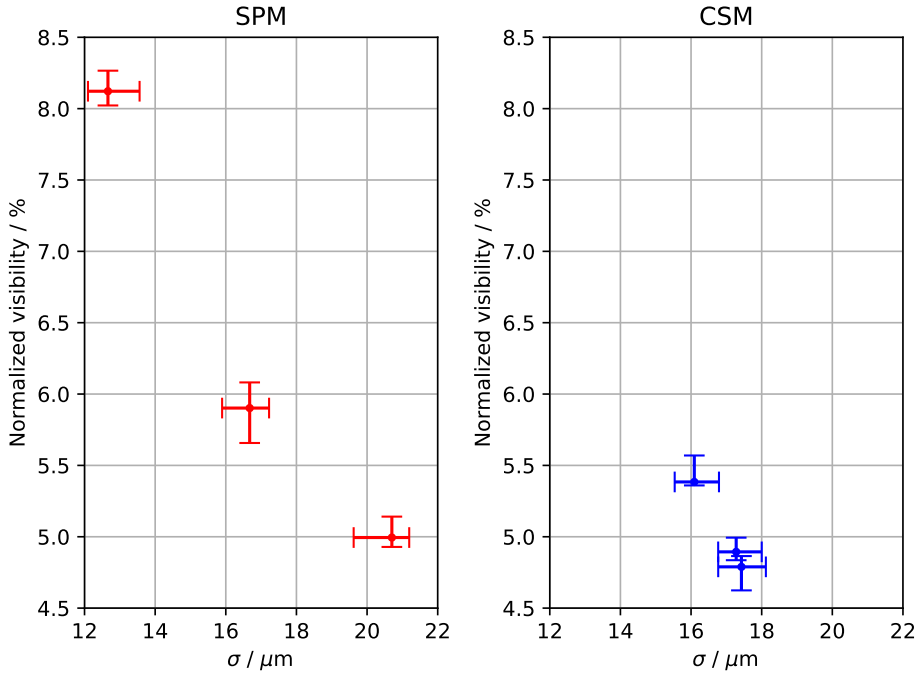

Figure 4.12.: The measured normalized visibility of the lung region for different effective point spread functions.

These results lead to the conclusion, that the visibility contrast is strongly dependent on the resolution of an imaging system and makes it difficult to compare results acquired with different imaging setups and settings without deep considerations about the information in the images. Structures, that are close to the resolution limit of the system, lead to an averaging of different signals within a single pixel, leading to a reduced visibility. As an example, one can imagine an edge, that creates a phase shift corresponding to half an analyzer grating shift. If this edge is directly centered on top of a large pixel, the pixel averages two intensity signals, that are shifted by π, resulting in a visibility of zero.

In addition, a source, that is coherent enough to create interference patterns from the sample, will boost this issue. The presence of high frequency interference patterns, which typically start to manifest as edge enhancement for low coherence sources, will create structures, that are most probable not resolvable, and will result in a local reduced visibility. For Talbot interferometers, where the coherence length must be in the order of a grating pitch or larger, interference patterns can be easily formed by a sample, that is located far enough from the detector (see 4.2.7).

These findings were published under [Koe+16].

4.2.7. Influences of Magnification and Source Size on Grating Interferometry Results

The system allows implementing multiple types of interferometric setups and also to easily change the magnification of the object onto the detector plane (without adjusting the interferometer).

This lead to a study of the influence of the sampling in grating based visibility contrast. By keeping the physical source size constant and varying the magnification of the sample, the projected source size (and therefore the averaged sample region) could be examined. A transition between the phase contrast and the visibility contrast could be observed.

The findings are consistent with the examinations with the varying sampling region in direct converting detectors (see 4.2.6).

For the experiment a symmetrical grating setup was employed with a source grating placed 3 cm in front of the X-ray tube. The distance between the source and phase grating (and the phase and analyzer grating) was 55.7 cm. For X-ray detection the Dexela 1207 (Varex Imaging) with a pixel pitch of 74.8 µm (see section 2.3) was employed. The X-ray tube was operated at 50 kV and 10 W. The same sample as in section 4.2.6 was used.

The transition of the contrasts, for different positions of the sample (rat lung), is illustrated in figure 4.13. By moving the sample along the beam axis, the effective pixel size changes while the sampling at the analyzer grating and the blurring of the source stays the same. This results in a different spatial sampling of the specimen.

These findings demonstrate, that the visibility contrast is highly dependent on the employed imaging setup and is difficult to correlate with a physical sample property. If used as a contrast for non-resolvable structure these findings can be used to optimize the setup for a certain contrast but also make it difficult to compare visibility contrast and phase contrast on a quantitative bases between multiple setups. These findings are published under [Koe+16].

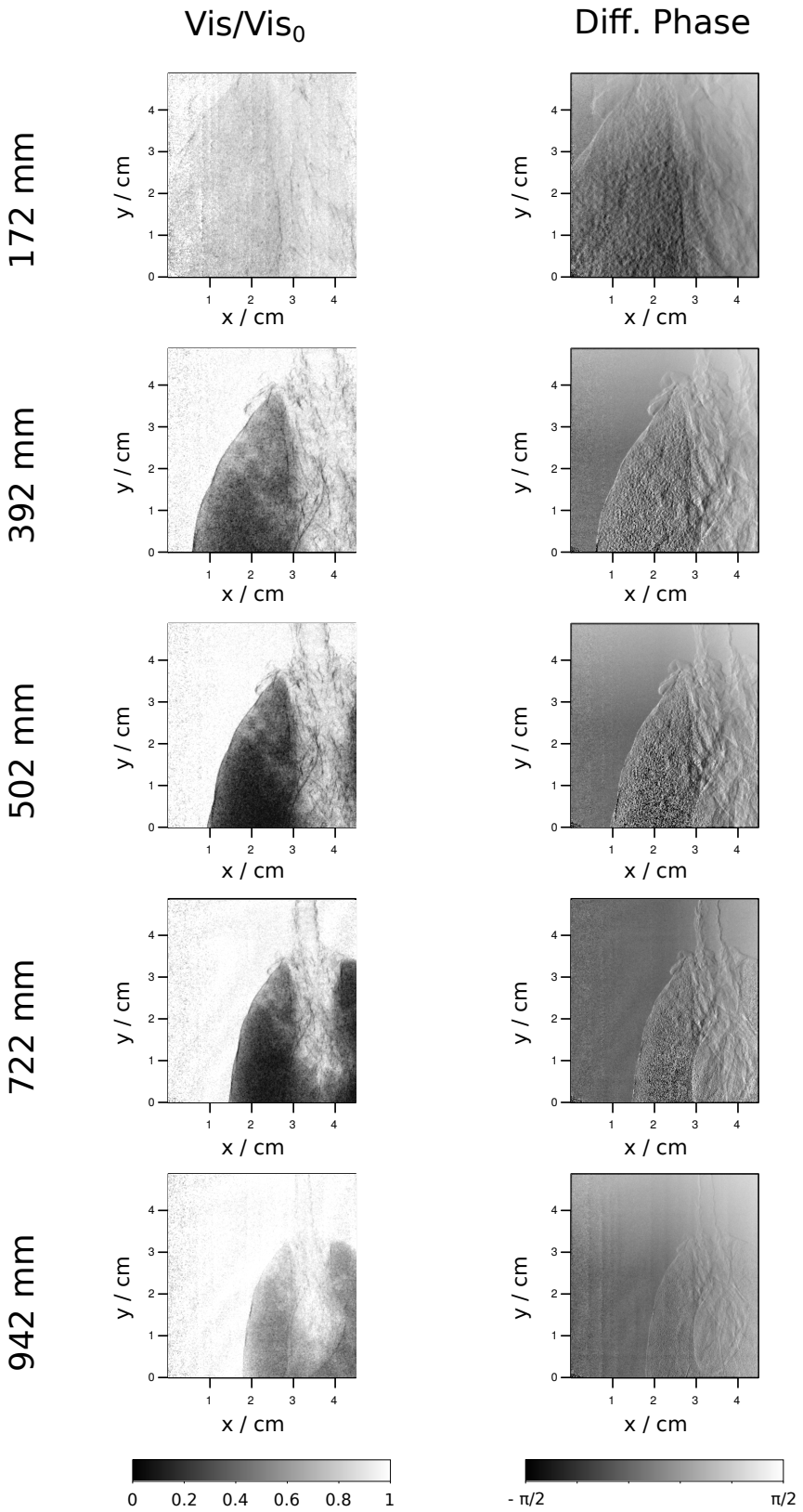

Figure 4.13.: Visibility contrast and differential phase contrast for different sample positions. The sample position is given (on the left side) by the source-sample distance.

4.3. Summary

In the chapter the image and contrast formation was discussed. Methods for extracting the attenuation and also the phase contrasts were discussed, as well as their limitations and influences of the imaging system, leading to different results, that can not be easily re-normalized. By employing the Medipix3RX (see chapter 3) and the possibility to perform grating interferometry with various magnifications in the CL/CT-Laboratory, I show a strong dependence between the visibility contrast and the spatial resolution of the imaging system.

5. Extending Projection Images to 3D Imaging

In chapter 4 the image formation of a single projection is described. In this part the transition of these projection images to 3D volumetric data and the mathematical background of the reconstruction of the 3D volume is explained. The presented reconstruction methods work with attenuation images as well as with the different contrasts of the grating interferometry from section 4.2.3. In addition, also a method for spectroscopic 3D data is described and evaluated.

5.1. Computed Tomography

Computed tomography (CT) is a common method to acquire 3D information from objects. The sample rotates, with respect to the source-detector, around an axis perpendicular to the central ray. By acquiring projection images and applying a correct data processing, the 3D distribution of the X-ray mass attenuation coefficient can be performed. I implemented computed tomography as a tool to produce ground truth data for comparison with other imaging techniques as well as to have the possibility to optimize the system for certain applications. For a better understanding of the requirements for CT measurements and the possible artefacts induced by non-ideal imaging properties I explain the filtered back projection method for reconstructing the 3D CT slices.

Here the reconstruction of an object from projections will be shown. This derivation of the *Filtered back projection* is based on the explanation in [Jäh05, section 8.6.2 and 8.6.3] and [KS01, section 3].

Figure 5.1 defines the geometry for the parallel computed tomography. On each detector pixel the projection of the object function $g(\vec{x})$ along the corresponding ray will be detected. The projection P can be written as

$$P(r,\theta) = \int\limits_{\text{path}} g(\vec{x})\,\mathrm{d}\vec{s}. \tag{5.1}$$

In case of X-ray tomography, where the line integral is created by the attenuation that is described by the Beer-Lambert law the projection of the linear mass attenuation coefficients $\mu(\vec{x})$ can be written as

$$P(r,\theta) = \int\limits_{\text{path}} g(\vec{x})\,\mathrm{d}\vec{s} = -\log\left(\frac{I(r,\theta)}{I_0(r,\theta)}\right) \tag{5.2}$$

where $I(r,\theta)$ and $I_0(r,\theta)$ denote the detected X-ray flux with and without the sample, respectively. The sample is placed at the origin of the coordinate system while

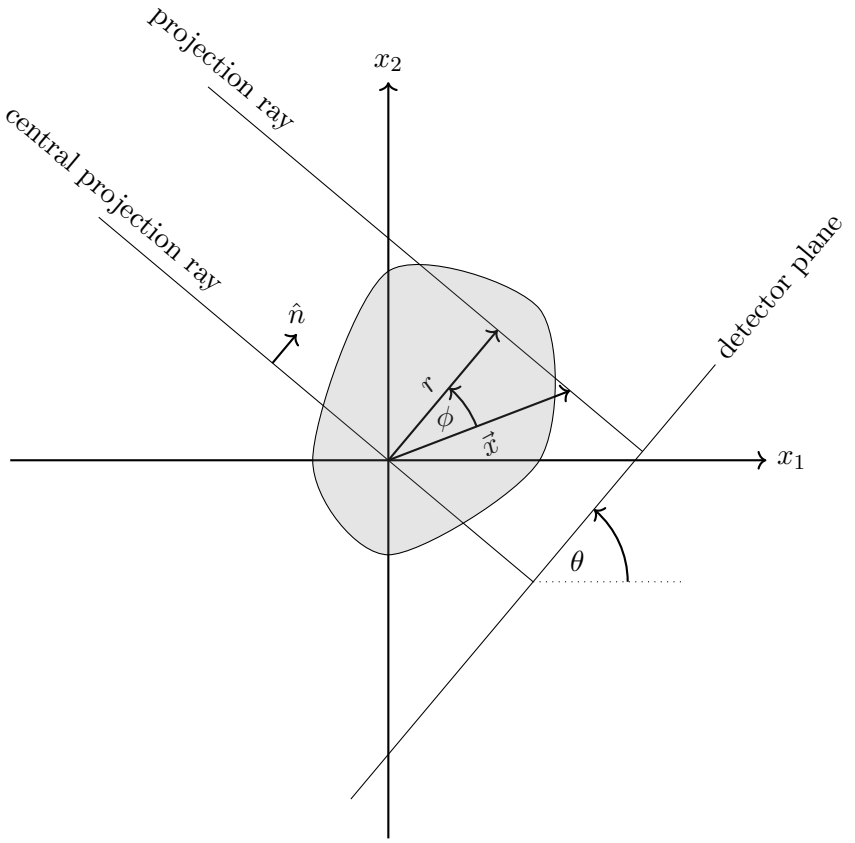

Figure 5.1.: Geometry definition for parallel beam CT. The sample is projected onto the detector plane.

the detector and the parallel beam source rotates around the sample, resulting in different angles of θ. The normal vector $\hat{n}$ to the projection ray can be written as

$$\hat{n} = \begin{pmatrix} \cos(\theta) \\ \sin(\theta) \end{pmatrix}. \tag{5.3}$$

A point along a projected ray is denoted $\vec{x}$. The angle ϕ gives the angle between $\vec{x}$ and $\hat{n}$ and is given by

$$\cos(\phi) = \frac{\vec{x} \cdot \hat{n}}{|\vec{x}|}. \tag{5.4}$$

This gives us the definition of r, the shift between the central ray and the projection ray, that passes through $\vec{x}$ as

$$r = \cos(\phi)\,|\vec{x}| = \vec{x} \cdot \hat{n}. \tag{5.5}$$

By combining (5.3) and (5.5) the constraint for points lying on a path at the distance r can be written as

$$\vec{x} \cdot \hat{n} = x_1 \cos(\theta) + \sin(\theta) - r = 0. \tag{5.6}$$

This can be used to rephrase (5.1)

$$P(r,\theta) = \int_{-\infty}^{\infty}\int_{-\infty}^{\infty} g(\vec{x})\,\delta(x_1\cos(\theta) + x_2\sin(\theta) - r)\,\mathrm{d}x_1\,\mathrm{d}x_2. \tag{5.7}$$

This projection of a two-dimensional function $g(\vec{x})$ on $P(r,\theta)$ is called *Radon transform*. The *Radon transform* can be characterized in the Fourier domain. Without loss of generality the projection will be discussed for $\theta = 0$. Then (5.1) can be written as

$$P(x',0) = \int_{-\infty}^{\infty} g(x',y')\,\mathrm{d}y'. \tag{5.8}$$

The Fourier transform of $P(x',0)$ is given by

$$\tilde{P}(k'_x,0) = \int_{-\infty}^{\infty} P(x',0)\exp(-2\pi k'_x x')\,\mathrm{d}x' = \int_{-\infty}^{\infty}\left[\int_{-\infty}^{\infty} g(x',y')\,\mathrm{d}y'\right]\exp(-2\pi i k'_x x')\,\mathrm{d}x'. \tag{5.9}$$

By adding the constant value of $\exp(-2\pi i 0 y') = 1$ into the inner integral it can be shown that $\tilde{P}(k'_x,0)$ can be identified with $\tilde{g}(k'_x,0)$:

$$\tilde{P}(k'_x,0) = \int_{-\infty}^{\infty}\int_{-\infty}^{\infty} g(x',y')\exp(-2\pi i k'_x x')\exp(-2\pi i 0 k'_y)\,\mathrm{d}x'\,\mathrm{d}y' = \tilde{g}(k'_x,0). \tag{5.10}$$

After applying a back transformation to make this valid for all values of θ this becomes

$$\tilde{P}(q,\theta) = \tilde{g}(\vec{k})\,\delta(\vec{k} - (\vec{k}\hat{n})\hat{n}). \tag{5.11}$$

This is the so called *Fourier slice theorem*. It tells that the Fourier transform of the projection is identical with the Fourier transform of the object along the corresponding normal vector $\hat{n}$. To apply the *Fourier slice theorem* that is given in polar coordinates (q,θ) to the *Radon transform* ((5.7)) it has to be transformed into polar coordinates as well:

$$g(\vec{x}) = \int_{0}^{2\pi}\int_{0}^{\infty} q\tilde{g}(q,\theta)\exp\left(2\pi i q(x_1\cos(\theta) + x_2\sin(\theta))\right)\mathrm{d}q\,\mathrm{d}\theta. \tag{5.12}$$

To apply the *Fourier slice theorem* the limits of the integrals have to be adjusted as well. Therefore, the integral is expanded into two parts

$$\begin{aligned} g(\vec{x}) = &\int_{0}^{\pi}\int_{0}^{\infty} q\tilde{g}(q,\theta)\exp\left(2\pi i q(x_1\cos(\theta) + x_2\sin(\theta))\right)\mathrm{d}q\,\mathrm{d}\theta \\ &+ \int_{0}^{\pi}\int_{0}^{\infty} q\tilde{g}(-q,\theta')\exp\left(-2\pi i q(x_1\cos(\theta') + x_2\sin(\theta'))\right)\mathrm{d}q\,\mathrm{d}\theta' \end{aligned} \tag{5.13}$$

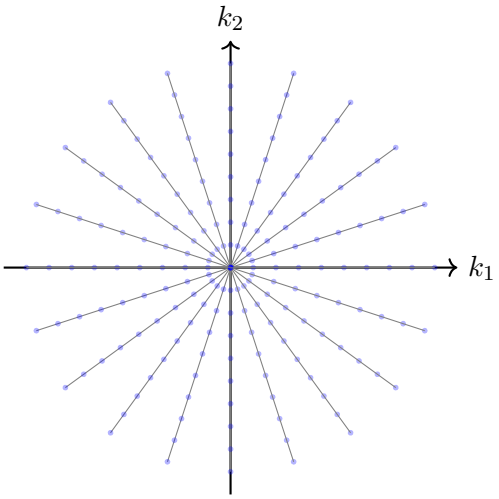

Figure 5.2.: Sampled Fourier space. he sampled points are denoted in blue. Here 10 projections and 19 pixels are used for the scheme.

with the substitutions $\theta' = \theta + \pi$, $\tilde{g}(-q, \theta) = \tilde{g}(q, \theta')$, $\cos(\theta') = -\cos(\theta)$ and $\sin(\theta') = -\sin(\theta)$. The two integrals in (5.13) can be combined into one integral with the proper limits again

$$g(\vec{x}) = \int_0^{\pi} \int_{-\infty}^{\infty} |q| \tilde{P}(q, \theta) \exp\left(2\pi i q (x_1 \cos(\theta) + x_2 \sin(\theta))\right) \mathrm{d}q \, \mathrm{d}\theta \tag{5.14}$$

$$= \int_0^{\pi} \mathcal{F}^{-1}(|q| \mathcal{F} P) \, \mathrm{d}\theta \tag{5.15}$$

$$= \int_0^{\pi} \left(\mathcal{F}^{-1}(|q|) * P\right) \mathrm{d}\theta. \tag{5.16}$$

This shows that the original object function $g(\vec{x})$ can be reconstructed by back projecting the projections after applying a convolution. Each angular projection results in sampling the Fourier space of the object function along one line through the axis of rotation. In case of a real measurement with finite number of angular projections (θ) and pixels (r) this would result in a Fourier space that has been sampled at discrete radial coordinates as shown in figure 5.2. An artifact free interpolation of these points onto a cartesian grid would result in many interpolation calculations. A more robust solution is to estimate the object function $g(\vec{x})$ by using (5.16), where the interpolation can be done in the real space. This is called the *Filtered back projection (FBP)*.

Moving to a divergent point source the projections are acquired in the so-called *Fan beam* geometry. The basic geometry is sketched in figure 5.3. This geometry can be easily transformed back to the previously described parallel beam case. All beams of the fan can be assigned to beams in the parallel beam geometry as

$$P_{\text{parallel}}(r, \theta') = P_{\text{fan}}(r - \sin(\theta), \theta + \alpha). \tag{5.17}$$

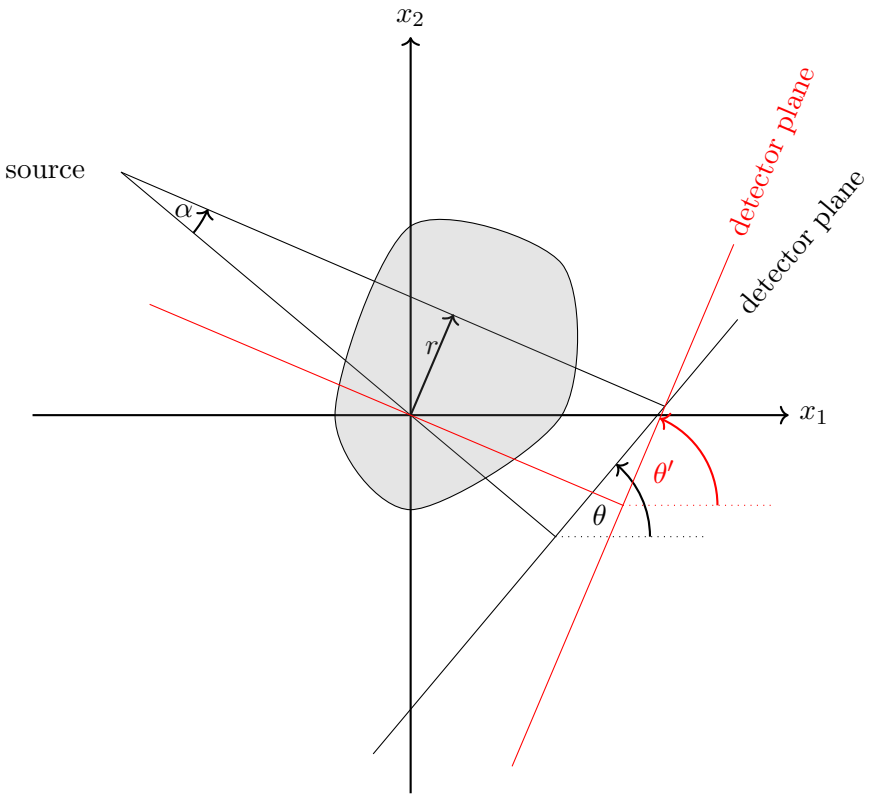

Figure 5.3.: Geometry definition for fan beam CT. All beams not passing through the center of rotation can be assigned to rays in the parallel beam case.

This relation is also shown in figure 5.3, where the red drawn detector plane is the corresponding detector position in the parallel beam case. In the ideal case of an infinite number of projections the parallel case can be completely applied to the fan beam measurement. However, if only a finite number of projections are recorded, the sampling in the Fourier space is different from in the parallel beam case. Therefore, the discrete filters have to be adjusted.

When multiple detector rows are used, a point like source will result in a conical beam geometry. Figure 5.4 shows the cone beam geometry from a side view. In such a case the sample and the detector are elongated along the x_3 axis. This leads to a conical ray propagation. Then the angle between the rays and the rotation axes at the sample is no longer perpendicular at all positions within the sample.

When going from the fan beam geometry, the filter kernel and the back-projection needs to corrected accordingly as it is implemented in the Feldkamp algorithm [FDK84].

$$d'_{\mathrm{SOD}} = \sqrt{d^2_{\mathrm{SOD}} + \zeta^2} \tag{5.18}$$

5.1.1. Implementations of CT Scans

I implemented different ways to perform automized computed tomography experiments. With these implementation CT scans can be performed automatically and the control system takes care of the most common issues, that can take place in long-running experiments (like instabilities in the source performance).

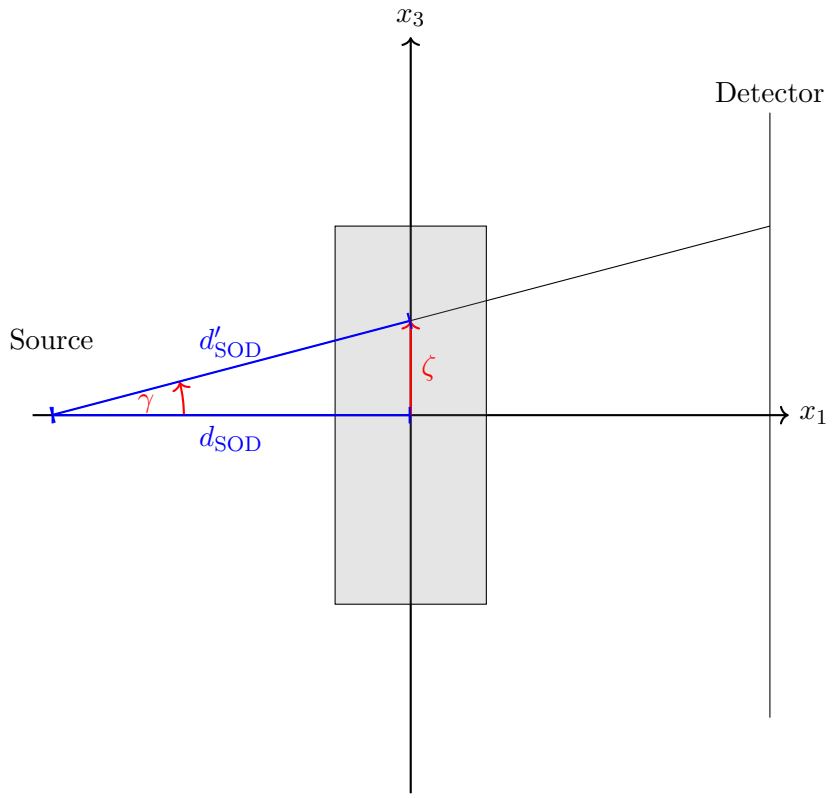

Figure 5.4.: Additional parameters for cone beam geometry. Side view of a cone beam projection. The axis of rotation is given by x_3.

The different CT implementations are all feature high level access to all relevant parameters like X-ray tube settings, detector settings and sampling of the tomographic rotation. Due to the abstraction level they can be used with all types of detectors, sources and sample environments.

The online reconstruction of *ufo* [Far+22] was also combined with the CT scans, yielding directly 3D volumes when a CT scan is finished.

The following automized image recording schemes were implemented in the laboratories control system *concert*.

Stepped Tomography In the stepped computed tomography the motor of the tomography axis moves to a defined number of angular positions (equally distributed over a defined range) and after each position is reached an image is acquired. In addition, images without radiation and images with radiation but without the sample in the field of view, are recorded to perform a pixel-wise offset and gain correction. This is called flat-field correction.

The concert implementation of this tomography uses the number of angular steps, the angular range, the number of dark and flat images and the tubes' acceleration voltage and target power as parameters. In addition, thresholds for the tube parameters can be give, enabling an online check of the X-ray tube, allowing an automized detection of instabilities in the X-ray tube. If a significant change of the X-ray tube performance is detected, the X-ray tube is reset, and the non-optimal frames are

repeated. This is especially required for long scans, that can easily exceed multiple hours.

Continuous Tomography In the continuous tomography implementation the tomography axis spins with a defined speed and images are continuously recorded by the detector. This method is preferred when fast tomograms are recorded and allows to minimize the time of the system, where no images are acquired. These times occur in the stepped implementation when the motors need to accelerate and decelerate and when the system waits until the target position is reached. In this laboratory system these additional dead times were measured to be below 10 ms. The continuous scan becomes important, when the acquisition times gets close to and smaller than this dead time. However, this scan mode needs a more precise control of the speeds, acceleration phases and detector synchronisation. All the automatic corrections described in the stepped tomography are also implemented in this tomography implementation.

Spiral Tomography The spiral tomography allows to scan thin long objects. In this case the detector and the source are moved on a synchronized trajectory parallel to the tomography axis[1]. One could think of later resorting the detector rows according to the angular position to get normal projections like in multiple 'normal' CT scans. The z-scanning (z corresponds to the x_3 axis in the description of CT reconstruction) also results in the fact, that not the same set of detector rows are always contributing to the same slice in the CT reconstruction. This distributes the artefacts more uniformly in the volume, which suppresses the presence of the so-called ring artefacts. The here employed ufo reconstruction[Far+22] backprojects the full projections onto the full volume. So no restoring of the data is required.

For most of the CT experiments, the sample was positioned on top of the 4-axis-manipulator (see: 2.4.1). Such a setup for tomography is shown in figure 5.5

For demonstration, a tree branch was scanned in the spiral scanning geometry. Therefore, 7265 images were scanned [2] with a vertical shift of 15 cm per revolution. This resulted in a volume of $2048 \times 2048 \times 5217$ voxels with a size of 82.35 µm. A photograph of the sample in the setup and a volume rendering of the resulting CT volume is shown in figure 5.6.

5.1.2. High Resolution CT

The use of the transmission X-ray tube head allows to perform CT scans with voxel sizes in the micro meter range. However, in such a setup the position of the source also needs to be stable within this accuracy while the sample is positioned close to the source. The presence of the precise alignment motors induce magnetic and electric fields to the X-ray tube that change the position of the electron beam, resulting in a moving source position. This effect also changing over time within the scan.

[1] It would be easier to just move the sample along the tomography axis while spinning the tomography axis. However, this degree of freedom is not present in this system. Therefore, the rest of the system needs to moved on parallel trajectories

[2] CT reconstruction performed by Tomáš Faragó

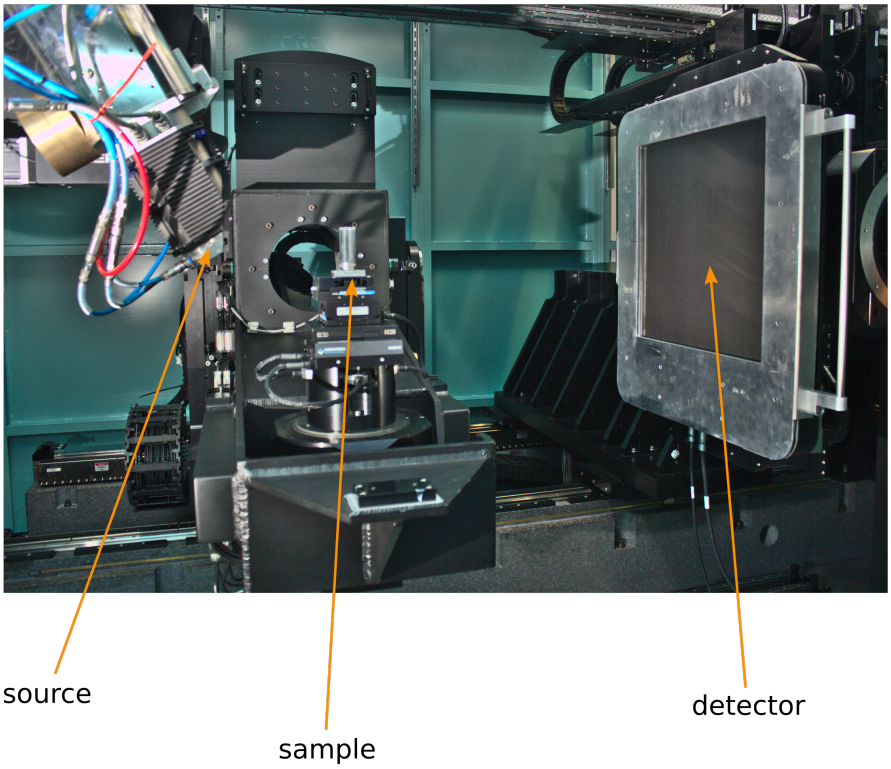

Figure 5.5.: Setup for computed tomography, featuring the direct tube head and the high-precision sample alignment module.

(a) Photograph of the tree branch in the setup. **(b)** Volume rendering of the reconstructed CT volume.

Figure 5.6.: Spiral CT was performed with a tree branch as specimen.

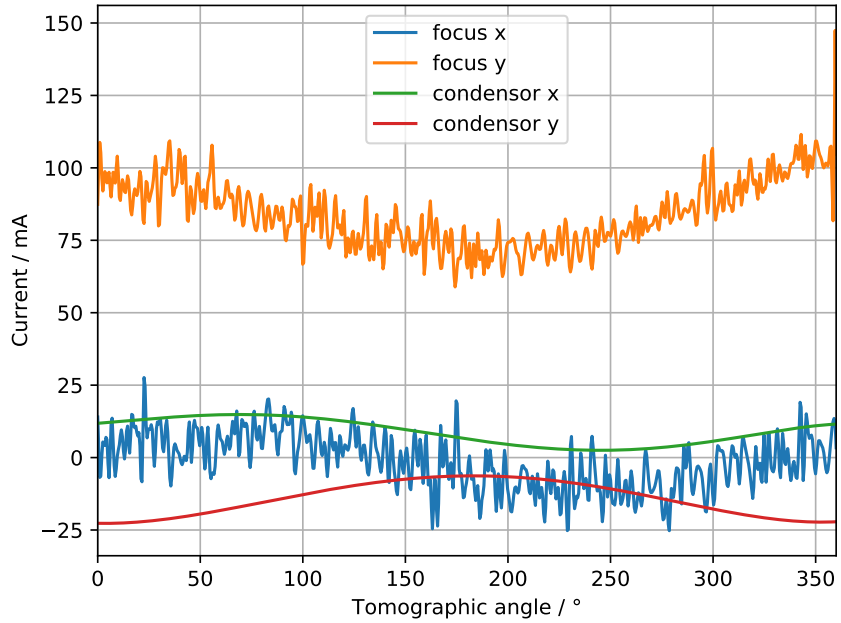

Figure 5.7.: Measured currents to maintain a stable source position.

Here, I present a method, that takes care of this effect and is required for high resolution computed tomography. Without this method, the deflection of the X-ray tubes electron beam would result in a completely unstable source size and position.

This method benefits from the strong integration of all the components of the setup in the control system. It learns the influences of the system onto the X-ray tube in advance of a CT scan and then adapts the X-ray tube settings accordingly within the actual CT scan to compensate the deflection of the electron beam.

To achieve resolutions better that 5 µm the transmission X-ray tube head is employed, featuring a source spot size below 1 µm. The position of the source needs to be stable over the whole CT scan. However, the magnetic field of the motors of the sample stage, which are close to the source, when a large magnification is required, deflect the electron beam in the X-ray tube and change the position where the beam hits the target.

Since the X-ray tube can be completely remote controlled via the control system, it is possible to compensate the external magnetic field with the focusing and centering coils in the X-ray tube.

Therefore, I implemented a procedure, where for a few different tomographic angles, the ideal settings for the centering is measured. This results in a set of ideal current settings for the x and y steering coils of the condenser and focusing section of the X-ray tube. This gives in total six current values for the internal coils, for each tomographic angle. In the actual CT scan, those values are interpolated and set for each position of the tomographic axis. This allowed to fully recover a stable source position at highest magnifications, resulting in voxel sizes below 1 µm.

To show the smoothness of the values for the operation of the alignment coils, the

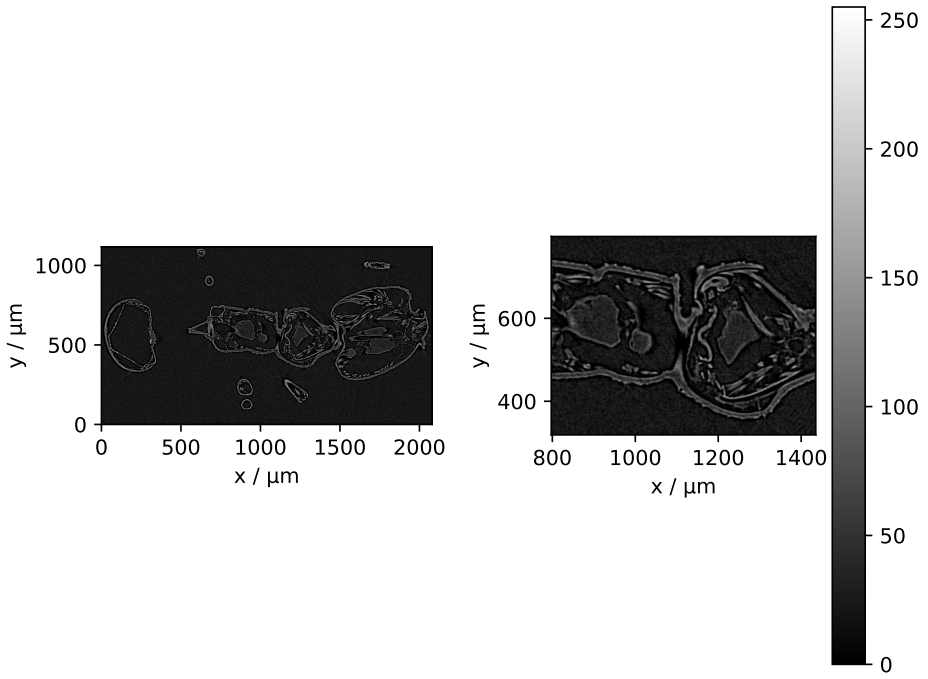

Figure 5.8.: High-resolution CT slice of an ant employing the high-resolution CT scan implementation.

best values were determined for a full revolution of the tomography axis in steps of 0.5°. The resulting values are shown in figure 5.7. The values of the focus coils scattered more, but they also have less influence on the resulting image quality. Each point was determined by the internal alignment procedure of the X-ray tube. This process is completely independent between the individual steps.

For a single scan, these values are sampled over 32 points and then interpolated.

In figure 5.8 resulting CT slices, generated with the here presented method are shown. When the correction of the electron beam steering is not present, the X-ray tube does not create a usable source spot after the tomographic motor is rotated by a few degrees.

5.1.3. CT for Large Samples

For large samples with not so high resolution a stitched CT scan was implemented. For the horizontal direction for all tomographic angles multiple x-positions of the detector position are recorded. The number of projections then needs to be adjusted to match the with of the stitched detector image. For the vertical extension of the sample, the source and detector are moved parallel (so basically, the sample moves along the z axis) to keep the amount of cone beam artefacts small. Due to the mechanical DOFs of the CL/CT-Laboratory all these detector postions will be scanned in an automatized manner. For stitching the different x positions to wide projection images, suitable for the CT reconstruction, I implemented python functions.

Application examples for the stitched CT scans are shown in the section 6.2.3 and

section 6.3.

5.2. Extending CT to Computed Laminography

Computed laminography (CL) is a method to examine flat laterally extended objects with high resolution in a selected field of view by the drawback of loosing spatial resolution in one dimension. The possibility of such imaging methods was a key requirement for the planing of the setup. The possibility of almost all geometrical arrangements of the source, detector and sample allow a lot more general imaging methods like CL. Computed laminography has been implemented in two different geometrical settings, allowing to either tilt the sample or to move the source and detector in order to keep the sample upright. The second option is preferred, when a sample is fragile and cannot be easily fixed to the sample holder.

Computed laminography (CL) is a more general imaging geometry than computed tomography. In a CL geometry the axis of rotation can be inclined by an arbitrary angle with respect to the optical axis, while for CT the axis is required to be perpendicular to the optical axis. This method is similar to tomosynthesis [Gra72], where usually the source is moved. At synchrotron sources, there are also implementations of this method [Hel+05].

In figure 5.9 is is demonstrated how CL is related with cone beam CT. One can imagine that the sample region-of-interest is shifted from the central beam by ζ, resulting in laminographic inclination angle of γ. In most cases, the detector is also rotated perpendicular to the new central beam direction to prevent distortions in the image.

This allows optimizing geometry for flat laterally extended objects. By inclining the tomographic axis, the projected thickness becomes more uniform during the tomographic rotation. This allows to minimize the maximum attenuation within an object and to minimize the required dynamic range of the detector system. Due to the inclination, not the full Fourier space can be samples, like it is done in CT (see figure 5.13). This results in an unsampled cone in the fourier space along the x_3 axis, resulting in blurring along this axis.

A typical setup for computed laminography would look like shown in figure 5.10.

In this geometry the tomographic axis still points upwards, but the detector and source are moved to realize an inclined optical axis. This helps, when fragile samples are scanned, since they don't need to be fixed on the inclined x-y-table of the setup.

In the laminography case the axis of rotation is inclined with respect to the beam path. The flexible setup in the CL/CT-Laboratory allows to implement this in two different ways. In the first one, the source and detector remain like in the standard CT geometry, but the axis of rotation is tilted by an additional motor on the sample stage. Then the axis of rotation is no longer pointing upwards. The magnification still can be easily changed like in the CT case. Also, the alignment of the geometry can be done in the CT geometry and then the axis is inclined by a known angle.

In the second possible implementation, the sample stage stays unchanged. Now the source and the detector are moved in a way that the rest of the setup makes the inclination. Now the axis of rotation still points upwards. This has the practical advantage, that the sample stays in a horizontal plane, allowing an easier fixation without the danger of the sample falling down. However, the alignment and the

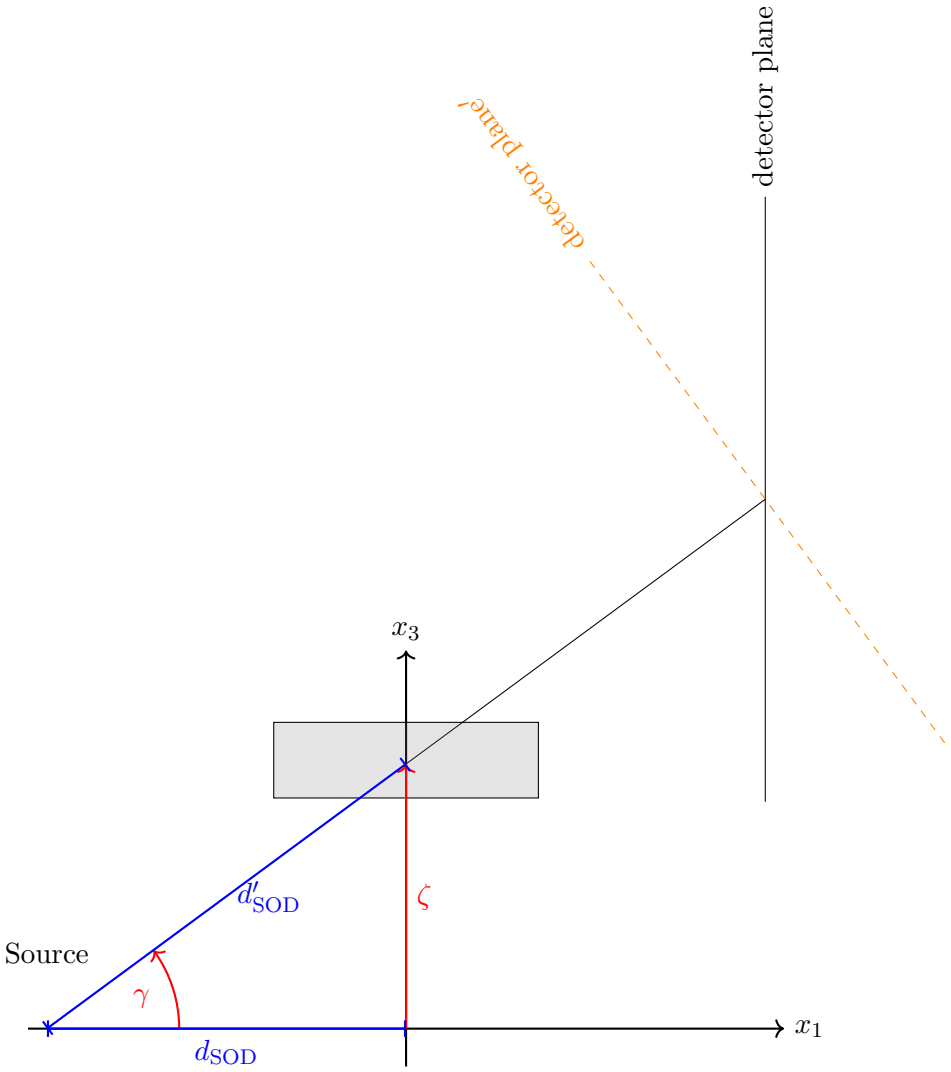

Figure 5.9.: Geometry definitions for cone beam laminography.

change of the magnification is more difficult, since multiple axes for the detector and source need to be moved to change the magnification.

In both implementations the sample can be scanned with the OX2-OY2 sample alignment within the sample plane (see section 2.4.2). This allows acquiring multiple CL scans, where later the volumes can be stitched together, resulting in large volumes.

Computed laminography can be widely applied to paleontology with flat compression fossils (see section 6.1.1 and section 6.1.2) and in the inspection of electron devices, which are also mostly planar.

In figure 5.11 a reconstructed CL slice of a DDR3 memory module is shown. The magnification was 20-fold, resulting in an effective pixel size of 10 µm and the tomographic axis was inclined by 20.9° with respect to the CT case. The memory is connected via flip-chip bonds with the circuit bord, which are visible in the zoomed region. One can also see small voids within these bonds. Due to the typical

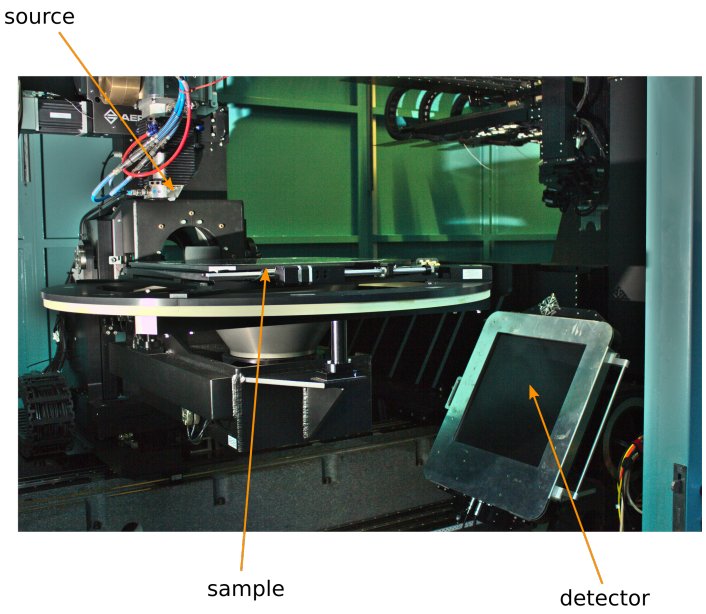

Figure 5.10.: Laminography setup. Here the setup is organized in a way, where the tomographic axis is pointing upwards and the rest of the components are rotated.

laminographic artefacts, the layers above and below are blurred overlapping.

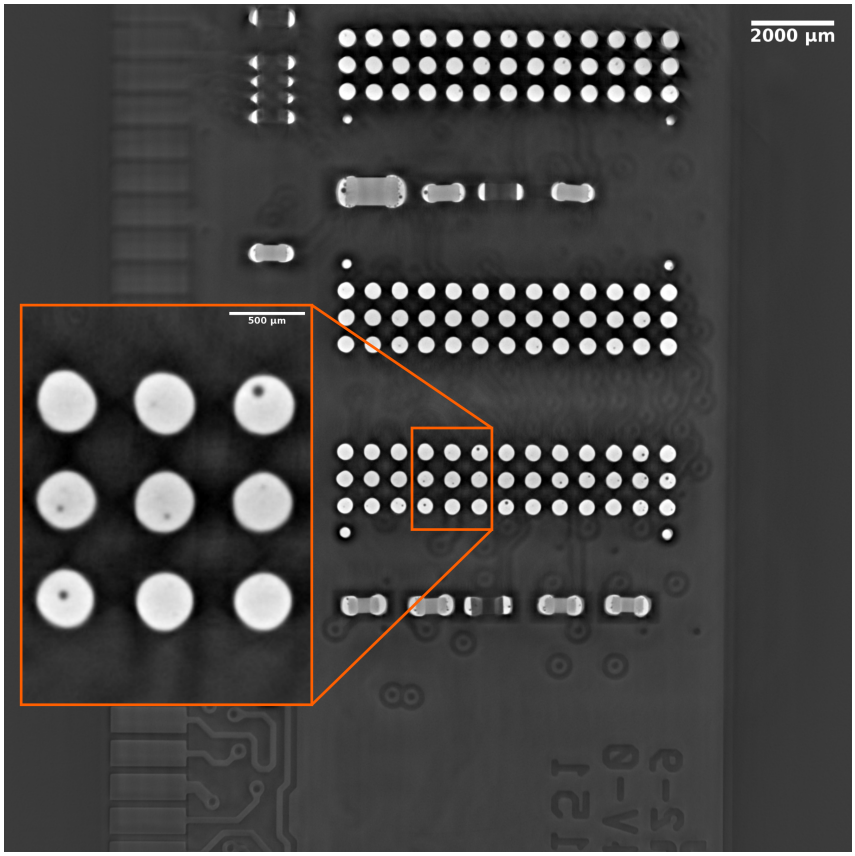

Figure 5.11.: Slice of a CL scan of a DDR3 memory module.

5.3. Augmented Laminograpgy: Extending CL with Prior Knowledge from CT Data

Computed laminography suffers from the fact that the 3D reconstruction is an ill-posed problem, resulting in artefacts. The use of prior knowledge allows restoring the missing information. Due to its flexibility, the system can acquire in addition to the CL scan low resolution CT data. In this section, I propose a method to partially fill the missing data with CT data as prior knowledge and demonstrate its applicability to compression fossils.

While computed laminography allows inspecting flat extended objects in a very high resolution, the method suffers from the artefacts, arising from the incomplete sampling of the specimen. Since the problem is ill-posed, these artefacts cannot be reduced without the use of prior knowledge of the sample.

There are multiple methods to reduce artefacts by adding prior knowledge to the reconstruction, like allowing only discrete attenuation values and assuring sharp edges.

I introduce a method called augmented laminography (AL), where the missing information in the CL reconstruction is partially filled by low resolution CT scans. Since the image formation (absorption in the sample as well as the detection) works identically, no knowledge about the sample is required. The flexibility of the setup allows us to perform both CT and CL in the same configurations of source and detector. Only the magnification will be adjusted accordingly.

Figure 5.13 illustrates the sampling of the Fourier space in CT, CL and AL. For CT a single projection populates a vertical plane with values. By the sample rotation different rotated planes around the k_z axis are added, resulting in a fully samples cylinder for a sufficient amount of angular steps. In the CL case the plane is inclined by the angle ϕ and is still rotating around the k_z axis. This results in two cones, that will never be samples. Due to the sampling of the fourier space in the laminography measurement scheme, the volume defined by $\sqrt{k_x^2 + k_y^2} < |k_z \tan \phi|$ is never populated. From those unsampled cones one can derive, that the missing resolution in z direction is introducing artefacts. In case of the AL the missing parts of the CL are partially filled with data acquired with a low resolution CT scan. CT scans in the full resolution are typically not possible.

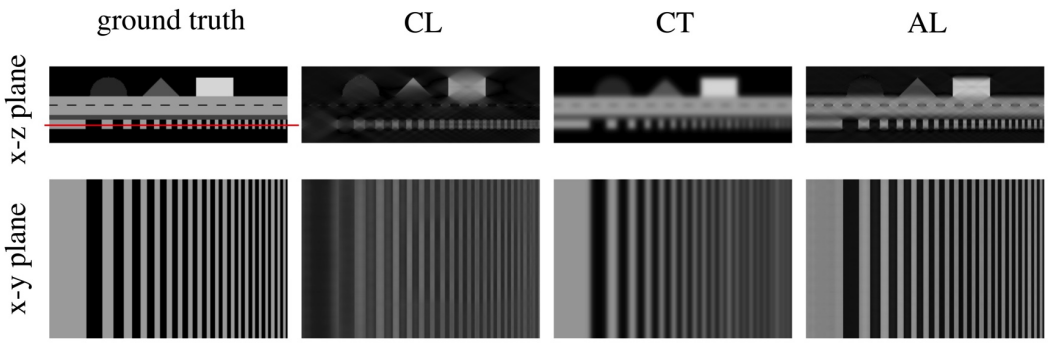

Figure 5.12.: Simulation of low resolution CT, CL and the combined AL. The red line denotes the position of the horizontal cuts.

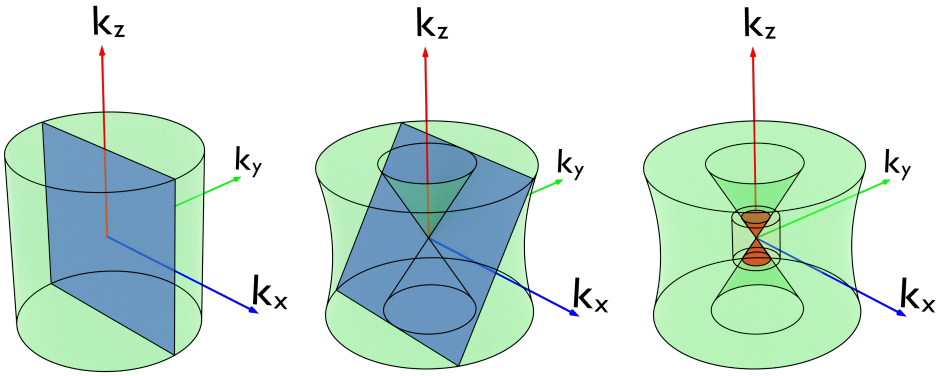

Figure 5.13.: Different samples regions in fourier space. **left:** Sampled volume in CT geometry. A single projection populates the region along one plane, that rotates for different projection angles. **middle:** Samples volume for CL geometry. Here the plane, that is populated by one projection is inclined. By filling the fourier space two cones are never filled. **right:** Sampled volume in AL. The small cylinder in the center represents a CT scan with a lower resolution. The two red cones from the CT data are used to fill parts of the missing cones in the volume that is samples by the CL scan.

The absence of the frequencies mostly directed along the k_z axis results in an unsharpness along the z axis in real space. The features, that are located in one xy plane are also blured visible in the slices above and below. In figure 5.12 this effect is shown for a simulated example. The laminography angle ϕ is set to 30°.

The CT images in figure 5.12 show the results of a simulated CT volume, acquired with a lower resolution. The data now has a lower resolution in all directions. However, in the region $\sqrt{k_x^2 + k_y^2} < |k_z \tan\phi|$ of the CL scan, we can use the frequencies, that are sampled by the CT scan. If this part is filled with the data of the CT scan, the resolution in z direction is partially restored.

For the actual implementation, CL and CT scans need to be performed and reconstructed to 3D volumes. The resulting volumes (which need to be correctly aligned) are then Fourier transformed. For each voxel in the Fourier space the most suitable data source is then combined to a reciprocal volume for AL. The resulting volume is then converted back to real space by the means of an inverse Fourier transformation.

The results of this method are shown in figure 5.12 in two example applications.

Multiple applications with scientific samples from paleontology are shown in section 6.1.

5.4. Spectroscopic CT for Material Specific 3D Datasets with Photon Counting Detectors

I implemented a method for spectroscopic CT in the new laboratory setup and in the IPS Detector-Lab[3] *based on the image domain and optimized the experiments for best spectroscopic imaging performance. In addition, I implemented a machine learning based algorithm to perform a decomposition of multiple materials. The*

[3] `https://www.ips.kit.edu/5930.php`

general applicability to create CT volumes that show the concentration/density of different materials is shown in this part, demonstrating that the X-ray laboratory is capable of performing spectroscopic CT imaging.

The spectroscopic imaging detector creates energy dependent images. Depending on the detector, those can be created within one acquisition or multiple acquisitions are required. The possibility of recording all spectral channels in one acquisition reduces the dose on the sample and is less prone to motion within the sample. However, in such an acquisition, the noise of the spectral channels are more correlated.

In this study, I apply a linear regression model, that works on the reconstructed CT volumes of the different energy channels [HTF09]. This means, first CT reconstructions of the different energy dependent images are applied, yielding multiple energy dependent 3D volumes of attenuation coefficients. For each voxel the different densities of the used materials is then calculated.

It would also be possible to first reconstruct a material dependent projected thickness of each material and then applying the CT reconstruction afterwards. This method would also allow compensating for beam hardening artifacts, but is more difficult to implement and is more prone to artefacts when unknown basis materials are present [DPS20].

Computed tomography scans were performed with four different energy thresholds (28 keV, 48 keV, 68 keV and 88 keV) in charge summing mode. The X-ray tube was operated with an acceleration voltage of 120 kV. After applying the CT-reconstruction an estimated energy and material dependent linear mass attenuation coefficient $\hat{\mu}$ can be assumed (see x-ray absorption contrast).

$$\hat{\mu}(\vec{x}) = \frac{\int\limits_{\text{disc.}} \left(1 - e^{-\mu_{\text{sensor}}(E)d}\right) s(E)\mu(E,\vec{x})\,\mathrm{d}E}{\int\limits_{\text{disc.}} \left(1 - e^{-\mu_{\text{sensor}}(E)d}\right) s(E)\,\mathrm{d}E} \tag{5.19}$$

CT slices of a known sample can be used for training these modes.

As model a linear regression model is applied. This model does not care about geometrical properties, therefore all voxels are treated the same way. The reconstructed CT volumes can be written as an $n \times p$ matrix X, where n is the number of voxels and p is the number of energy channels. The measured values are shifted and rescaled to have a mean value of zero and a variance of one. The exact rescaling needs to be applied onto all measurement the estimated $\hat{\beta}$ will be applied to. Due to the linearity of the model it can be assumed that

$$\vec{y_i} = X\vec{\beta_i}, \tag{5.20}$$

where the n-dimensional vector $\vec{y}$ denotes the material concentrations. By solving the system of equations, β can be determined for a training dataset, featuring the measured X as well as the known y of a known test sample. β can then afterwards applied to an unknown voxel, resulting in material concentrations. β can be esti-

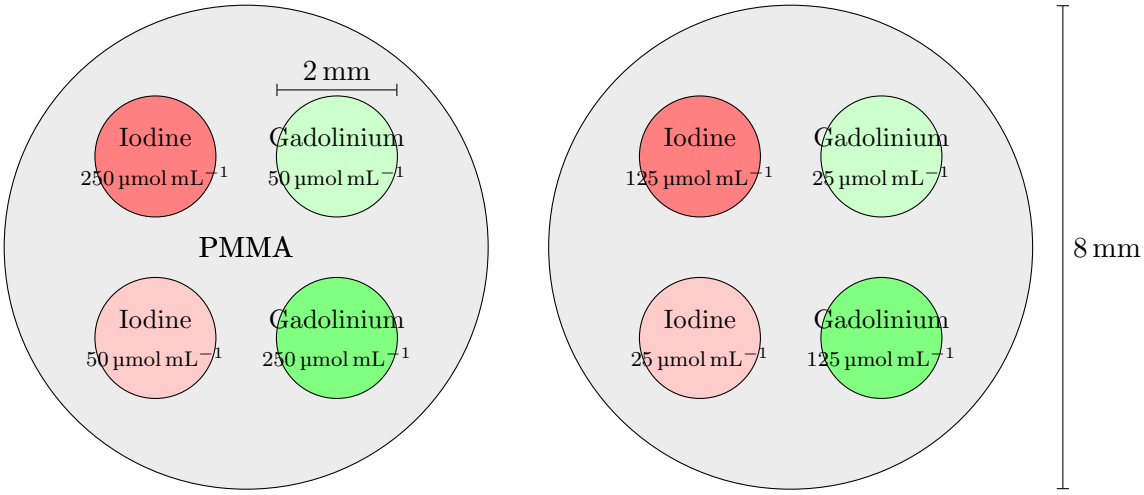

Figure 5.14.: Contrast agent phantoms used for spectroscopic CT.

mated from the calibration measurement with the least squares approach ([HTF09]):

$$\hat{\vec{\beta}}_i = \arg\min \left(\left(\vec{y}_i - X\vec{\beta}_i \right)^T \left(\vec{y}_i - X\vec{\beta}_i \right) \right) \tag{5.21}$$

$$= \left(X^T X \right)^{-1} X^T \vec{y}_i. \tag{5.22}$$

For the following study a sample, consisting of a Poly(methyl methacrylate) (PMMA) cylinder with four capillaries was used. The capillaries where filled with solutions of gadolinium and iodine of different concentrations. The used set of contrast agent concentrations, and the geometrical dimensions are shown in figure 5.14.

The linear mass attenuation coefficients of the different materials in the phantom are shown in figure 5.15. The attenuation coefficients of water and PMMA are quite similar and both materials will be treated as the same material with different densities.

Scatter plots for the different energy thresholds of the reconstructed attenuation coefficient are shown in figure 5.17. The colored points belong to a labeled region, where the material is exactly known. The gray points are from regions, where the voxels can not be exactly registered to a specific material, e.g. at the blurred borders of a capillary. For the training and validation only the colored and labeled voxels where used. In order to equally include the different materials in the model, the same amount of randomly chosen voxels of each material where included in the training of the model, while the other pixels where ignored in the training process. For the validation all voxels, that are not in border regions are included. All values for the training the known concentrations of the gadolinium and iodine were used for the contrast agents. For the PMMA/water, the density was used, which is $1\,\mathrm{g\,cm^{-3}}$ for the contrast agent solutions and $1.18\,\mathrm{g\,cm^{-3}}$ for the PMMA. The air region was trained as zero for all materials.

The resulting material specific CT slices are shown in figure 5.18.

The implementation of spectroscopic CT can be applied on different types of samples. It can be used to determine the distribution of contrast agents in differ-

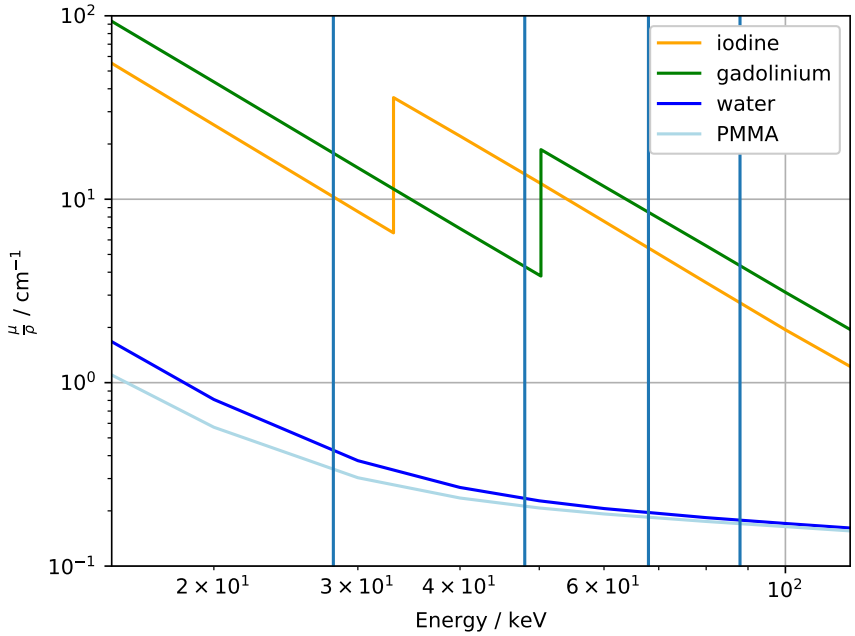

Figure 5.15.: Linear mass attenuation coefficient of water, iodine, gadolinium and PMMA [HS15]. The blue lines denote the positions of the applied energy thresholds of the Medipix3RX detector.

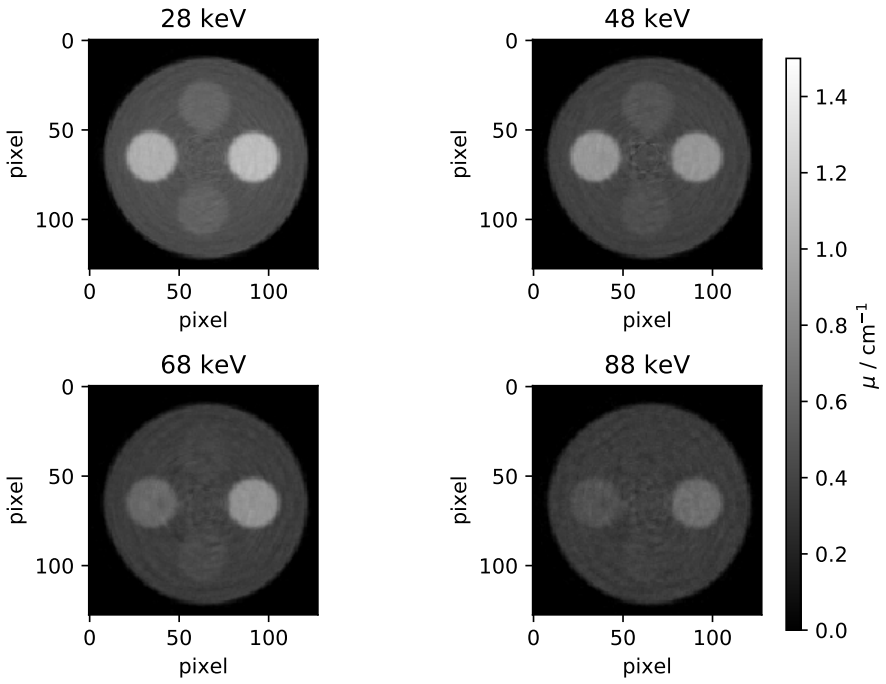

Figure 5.16.: CT slices with different energy thresholds of the contrast agent test phantom with iodine and gadolinium solutions.

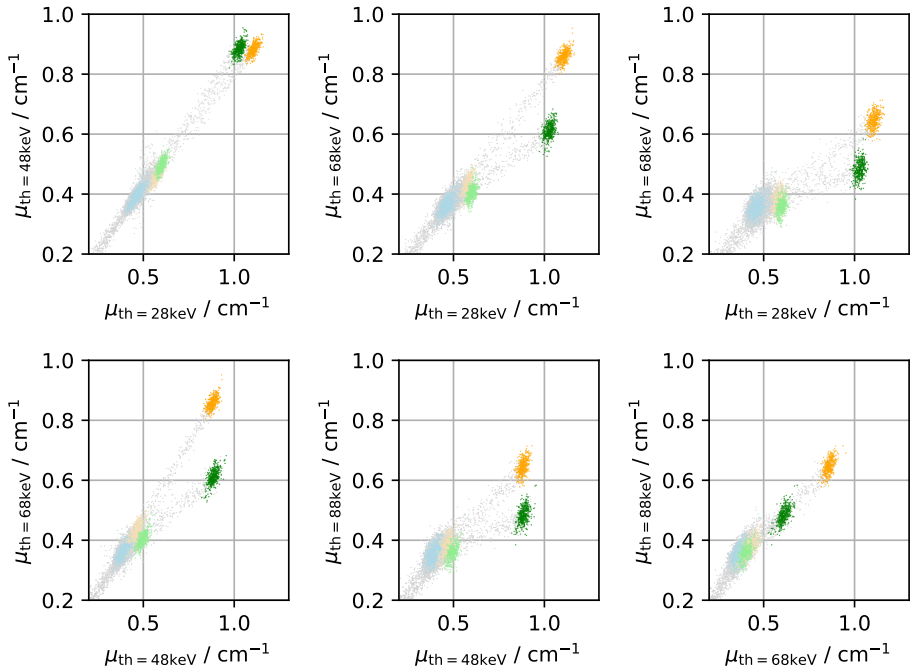

Figure 5.17.: Scatter plots of the reconstructed attenuation coefficients of the low concentration phantom (25 µmol mL^{-1} and 125 µmol mL^{-1} concentrations of iodine and gadolinium.). The color denotes to which segmented area the voxels belong. Orange marks the iodine capillaries and green the gadolinium. The PMMA is labeled with blue.

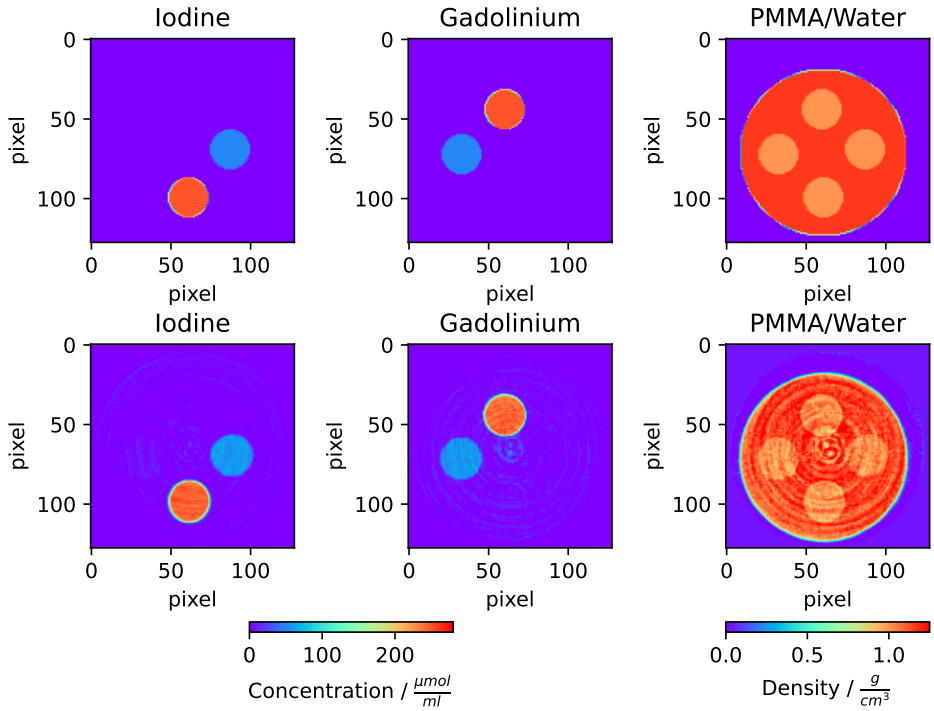

Figure 5.18.: Reconstructed material specific for the high concentration phantom. The density difference between the density of PMMA and water are clearly visible in the PMMA/water channel.

ent scientific fields. The concentrations used here are extremely low, compared to non-living stained specimens. For the set of concentrations of 250 µmol mL^{-1} and 50 µmol mL^{-1} the correct concentrations can be reconstructed. When a training set with lower concentrations is used, the attenuation coefficients of the different energy channels are not seperated enough for the training algorithm. Since both test cases where trained with data with the same range of concentrations, the use of a training set with a higher concentration could also decrease the errors for lower concentrations. The possibility to distinguish the different contrast agents could lead to new fixation/staining protocols, where the tissue specific staining can be used, resulting in directly tissue specific CT slices.

Also, this model can easily be extended to more materials, if a larger amount of energy thresholds are applied. This is currently limited by the amount of thresholds and counters present in the detectors (if the scan should be done in a single shot).

It is also important to remember, that this method is not a classifier but gives pixel-wise concentrations of all basis materials and can therefore also be applied when materials are mixed. This happens in this phantom in the contrast agent region, where the contrast agent concentration as well as the water density is correctly detected.

This method and the required optimization steps where published in [Koe+14b; Koe+14a; Ham+14; Bal+16; Zub+14].

The detected material concentrations are similar as other spectroscopic CT implementations employing photon counting detectors [But+09]. However, the results are not completely comparable, since the other implementations use a classifier, not

allowing a pixel-wise mixing of different materials.

The implementation of this method allows to reconstruct material specific CT slices with quantitative values for the material concentrations, which can be used for further analysis and is (when the calibration is done in the same framework) completely independent on the imaging system.

5.5. Summary

In this chapter, the methods of computed tomography and the more general computed laminography are described as a possibility to get three-dimensional data out of the two-dimensional projection images described in chapter 4. Starting from this, I implemented various routines in the CL/CT-Laboratory to carry out these measurements with different optimizations for different sample types (e.g. flat samples or small samples with high resolutions). The resulting implementations for CT scans and online data processing in the control system are open source and are employed also in other experimental stations and facilities. By using the unique features of the CL/CT-Laboratories new methods like augmented laminography where developed. With the detectors characterized in chapter 3 I implemented a method for material specific 3D reconstructions.

6. Application Examples

Here I demonstrate how I optimized and applied the CL/CT-Laboratory for multiple applications from various scientific fields. The applications where mostly done in collaborations with research partners, that where experts in the corresponding research field while I contributed the knowledge about the X-ray physics, the imaging techniques, optimized the X-ray setup for the special needs. The resulting image data, then allowed the scientist form the different fields a deeper analysis of the specimens.

In the following sections, I will give a short introduction into the scientific question and how I could use the unique features of the laboratory setup to contribute to the different scientific fields. In each example, the special requirements, that could be achieved with the here presented X-ray imaging setup, are described in the requirements part.

6.1. Paleontology

Samples from paleontology are often preserved in compression fossils and morphological features of the specimen can be hidden inside the stone matrix inaccessible for optical inspections from the surface. These specimens are embedded in laterally extended flat samples with thicknesses ranging from a few mm up to multiple cm. This geometry makes laminography and augmented laminography a well suited method. The specimens are also often heavy and fragile. The possibility to keep the samples in a horizontal orientation within the experiment often is a required feature, to acquire images without destroying unique samples.

6.1.1. Askeptosaurus italicus

Collaboration

The studies where carried out together with the Paläontologisches Institut und Museum (Universität Zürich).

Sample description

Askeptosaurus italicus is a marine reptile from the Middle Triassic. It can have a length of up to 2.5 m with a skull length of up to 26 cm and has a long neck and tail.

The specimen of this study is a compression fossil with a size of approximately 25 cm × 14 mm. The total size of the stone, where the fossil was embedded is a few cm larger and is 3 cm thick.

Summary

In this science case the augmented laminography (see 5.3) was required to achieve 3D datasets with a high resolution, high signal-to-noise ratio and without the presence of strong artefact, that would be present when only CL is applied. For this study, the flexibility of the setup, to do low resolution CT and high resolution Laminography was essential in the same experimental environment.

Requirements

Changeable magnification, tomographic axis can be inclined, high energy, horizontal sample plane (due to the fragile sample, the tomographic axis needed to point upwards).

Experiment description

For the experiments the direct tube head and the PerkinElmer XRD 1621 CN14 ES detector (see section 2.3) were employed. The X-ray tube was operated with an acceleration voltage of 200 kV and the beam was filtered with a 2 mm thick copper filter (in the CL case). The effective pixel size for the CL scan was set to 80 µm and 103 µm for the CT scan. Due to the size of the specimen multiple scans where required and stitched to a large volume afterwards (approximately 4000 × 2000 × 500 voxel). For both scans, 2048 projections, where recorded over an angular range of 360°. The tomography axis was inclined by an angle of 30 deg for the laminography case compared to the CT case. Finally, the data was combined as described in section 5.3.

Results

Cuts through the resulting volumes of CT, CL and AL are shown in figure 6.1. While both CT and CL feature unique features, the combined AL dataset allows to examine the specimen with the benefits from both methods. This allows a better understanding of the morphology of the specimen and may lead to a deeper understanding on the sample environment and behaviours. The data delivered invaluable information for the completion of a PhD thesis in paleontology and a corresponding publication is in preparation.

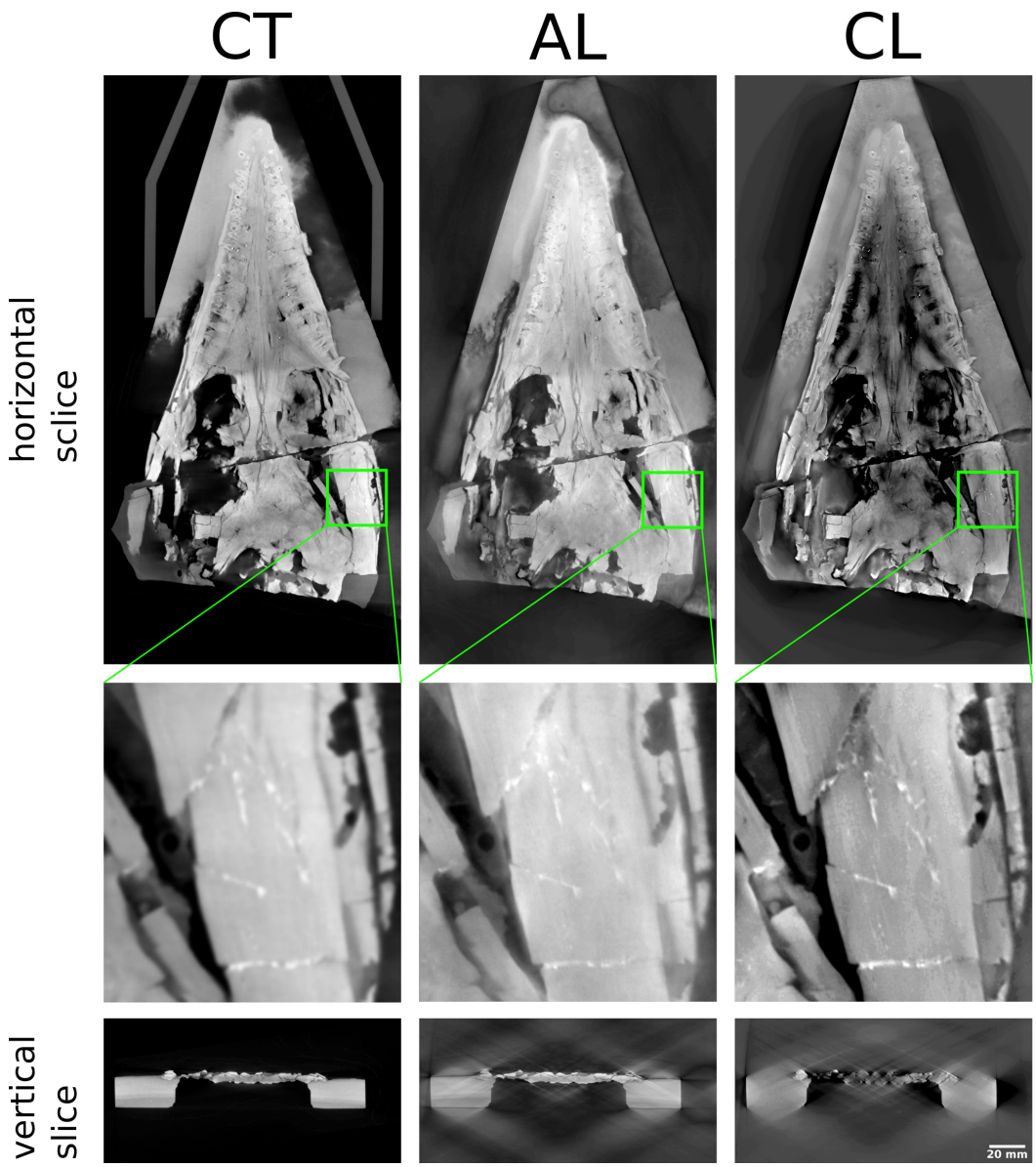

Figure 6.1.: Computed tomography (CT), Computed laminography (CL) and fused data (AL) of the *Askeptosaurus italicus* specimen. The CL data has the highest resolution within a horizontal slice but has limited resolution in the vertical slice. The CT scan has a lower resolution but this resolution is also the same in the vertical slice. The AL results in a high resolution in the horizontal slice and suppresses the artefacts from the CL in the vertical slice a lot.

6.1.2. Limulitella

Collaboration

The studies where carried out together with the University of Duisburg-Essen and the Martin-Luther-University Halle-Wittenberg.

Sample description

A compression fossil out of Muschelkalk with the specimen size of approximately 30 mm × 30 mm. The total size of the stone, where the fossil was embedded is a few mm larger and is 6 mm thick.

Summary

In this application the capability of the laboratory for method development can be demonstrated. The combination of CT and CL data into an AL data set (see 5.3) can be demonstrated on a compression fossil of a *Limulitella* (horseshoe crab). For this study, the flexibility of the setup, to do low resolution CT and high resolution Laminography was essential in the same experimental environment.

Requirements

Changeable magnification, tomographic axis can be inclined, high energy, horizontal sample plane (due to the fragile sample, the tomographic axis needed to point upwards).

Experiment description

For the experiments the direct tube head and the PerkinElmer XRD 1621 CN14 ES detector (see section 2.3) were employed. The X-ray tube was operated with an acceleration voltage of 200 kV and the beam was filtered with a 1 mm thick copper filter (4 mm in the CL case). For the CT scan a 5.16-fold magnification was chosen to cover the whole sample. The CL scan does not require, that the full sample is in the field of view. Therefore, the magnification could be increased to 8.28. For both scans, 2048 projections, each exposed for 36 s where recorded over an angular range of 360°. The tomography axis was inclined by an angle of 29.8 deg for the laminography case compared to the CT case. Both scans where reconstructed with Octopus 8.6[1] and the data fusion was performed using *python* and the *numpy*[2] library for the fourier transformations.

Results

Cuts through the resulting volumes of CT, CL and AL are shown in figure 6.2. This method and the resulting specimen description, that was not feasible without the presented scans, are published under [Zub+17] and lead to following collaborations in the field of paleontology.

[1] Inside Matters, Gent, Belgium
[2] `https://numpy.org/`

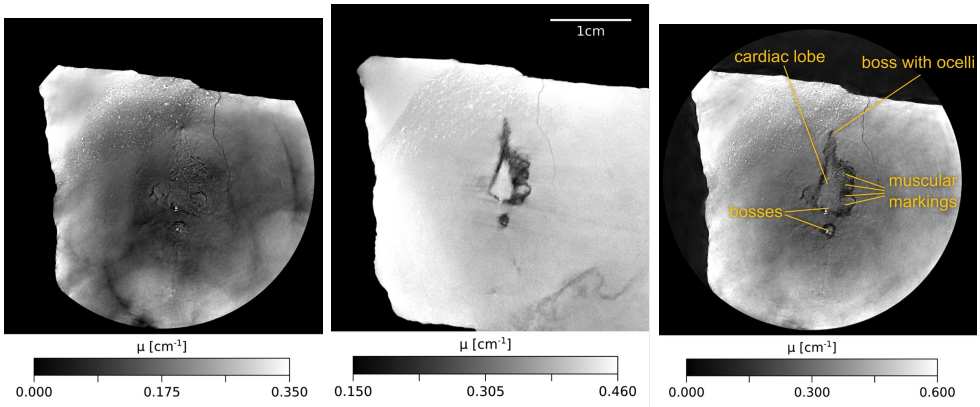

(a) CT slice of the specimen. **(b)** Laminography slice of the specimen **(c)** Augmented laminography slice of the specimen.

Figure 6.2.: Cuts through the CT, CL and AL volumes of the Limulitella specimen.

6.2. Biology

6.2.1. Screening of Ants

Requirements

Flexible magnification, high resolution

Summary

Over 2000 ant specimen where scanned with synchrotron tomography (SR-μCT) in collaboration with the Biodiversity and Biocomplexity Unit of the Okinawa Institute of Science and Technology (OIST). These specimen cover around 65% of the ant species in the world and the data can be used for a better understanding of biodiversity and evolution of ants. Due to the limited field of view in SR-μCT these examinations where concluded by scanning the larger specimens in the heere presented setup.

Figure 6.3 shows the spectrum of sample sizes.

Most of the samples where scanned using SR-μCT due to the shorter scanning times (approximately 30 s sample exposure for a full tomogram). However, in figure 6.4 it is demonstrated, the similar spatial resolution and data quality can also be realized with the here presented laboratory based setup offering much reduced flux but result in scanning times of multiple hours per specimen.

For this scan, the online X-ray tube alignment method (see 5.1.2) is performed.

Results

The CT scans at the laboratory allowed to complete the synchrotron experiments for larger sample sizes. It can also be demonstrated, that in general similar resolutions as synchrotron sources based experiment stations can deliver, can be achieved with longer scanning times.

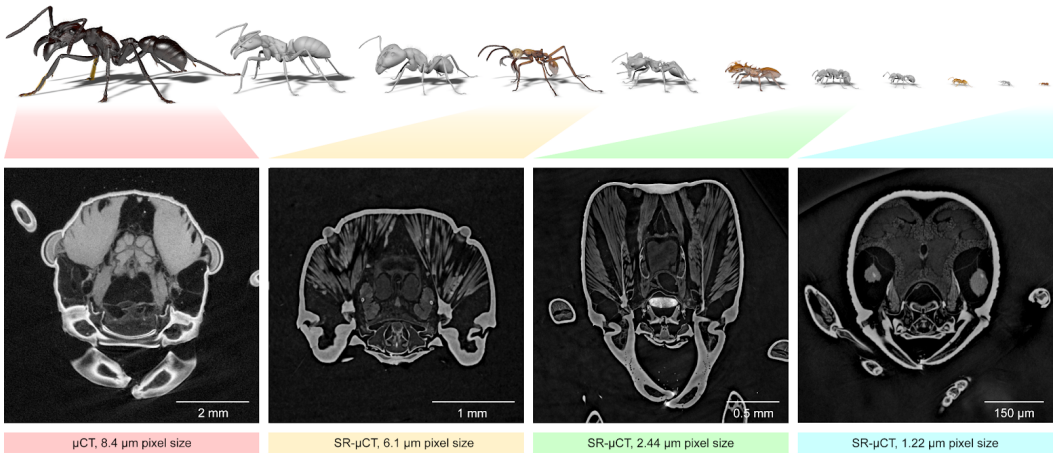

Figure 6.3.: Top row: rendering of ant CT data. Bottom row: CT slices from selected specimen. The left (largest) specimen was scanned in the laboratory setup. The smaller ones where scanned with SR-μCT. (Visualization done by Thomas van de Kamp)

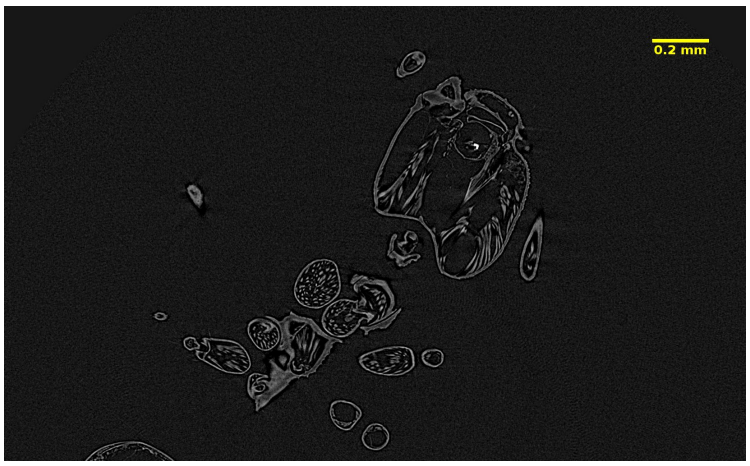

(a) CT slice of the specimen.

(b) Volume rendering of the specimen. The view is cut to show the inner parts of the specimen.

(c) Volume rendering of the specimen from the top.

Figure 6.4.: High resolution CT of an ant. This specimen was dried, resulting in less inner features.

Figure 6.5.: Volume Rendering of two salamander skulls. Both specimens where scanned side by side in one acquisition.

6.2.2. Study on a Large Amount of Salamanders

Requirements

Modular detector, sample and source modules

Summary

In order to measure a large amount of samples (over 200) with the aim to show the bone structure of salamanders, the setup has been optimized for speed while maintaining the required contrast and quality.

Therefore, I optimized the spectrum, the tube power, the magnification and the field of view. This resulted in the possibility to measure multiple samples at the same time in quite short scanning times. Volume renderings of two skulls are shown in figure 6.5.

Results

The resulting data enabled a detailed statistical study about the bone geometry of salamander skulls published under [Pog+20; Pog+21].

6.2.3. Red River Softshell Turtle

Summary

The scans of a large Red River Softshell Turtle *Rafetus swinhoei*[Gra73; Far92] were performed together with the University Bonn.

Since the specimens dimension where approximately 45 cm in length, and 35 cm in diameter, it would not fit in typical micro CT scanners, which mostly limited to sample sizes of approximately 25 cm. With a medial human CT scanner, the sample could be measured, however, the voxel sized are typically in the range of 1 mm down to 250 µm. Thus, the CL/CT-Laboratories capabilities for enlarged field of view with resolution better then 100 µm were perfectly suited for the sample geometry.

Requirements

Special sample environment (large housing to keep the sample in a safe environment), large field of view, possibility to acquire images that can be stitched the large projections.

Experiment description

In the CL/CT-Laboratory a micro CT scan was possible with a voxel size of 88.6 µm, covering the whole specimen. Therefore, a total of nine CT scans where performed to cover the whole sample. For sampling the whole specimen, the detector was shifted horizontally to three different positions (−20 cm, 0 cm and 20 cm) to enlarge the width of the field of view. These three projection sets where afterwards stitched with the stitching algorithm [PST09] to wide projection images. Out of these projections volumes where reconstructed. This was then repeated for three different height positions of the sample (the detector and the source where shifted, since the height of the sample can not be changed in the setup). The resulting three volumes where later stitched to one large volume using Amira.

The resulting volume (already cropped to the sample dimensions), was a volume of 1904 x 3585 x 5403 pixels with a voxel size of 88.6 µm, resulting in a volume of 16.87 cm 37.77 cm 47.87 cm.

Results

This work has already been published in [Hir+18, p. 66-68].

A resulting CT slice is shown in figure 6.6a. Volume renderings, showing different ranges of reconstructed attenuation coefficients, are shown in the figures 6.6b and 6.6c. The small, weakly absorbing parts around the sample are parts of the styrofoam that was used to fixate the specimen within the scan.

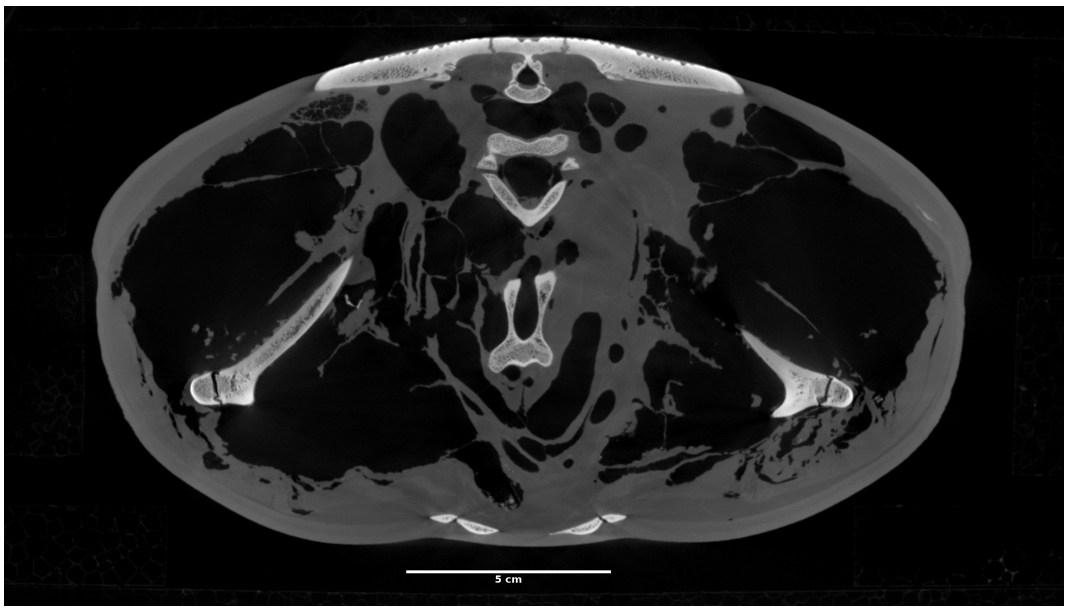

(a) CT slice of the specimen.

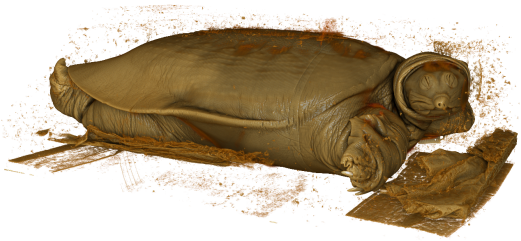

(b) Volume rendering of the specimen showing the weak absorbing parts.

(c) Volume rendering of the specimen showing the high absorbing parts.

Figure 6.6.: Figures of the red river soft shell turtle.

6.2.4. Model Organisms: Medaka

Summary

At IPS a large project aims to do correlations between morphological features of medaka (*Oryzias latipes*, Japanese rice fish) with its genome. Therefore, large amounts of these fishes are scanned with synchrotron micro CT. Since the availability of measurement times at a synchrotron are quite limited, the laboratory gives a great possibility for optimizations in the sample preparation. For the synchrotron experiments the samples needed to be stained with a contrast agent. The protocols for staining feature many possibilities for optimization. The laboratory allowed performing CT scans on a lot of fish with different types of staining. The setup could be optimized to match the contrast of the synchrotron scans as good as possible (see figure 6.7). While it is possible to get 3D images similar to synchrotron CT (in means of resolution and contrast) but with a lot longer scanning times, here it was chosen to run the scans with less quality and with short acquisition times but with a similar contrast, by optimizing the X-ray tube spectrum to match the synchrotron contrast formation.

The possibility to scan the height of the tube and the detector, allowed stacking multiple samples and to automatically run multiple CT scans without the need of a person to exchange the samples.

Sample description

The medaka is a small fish (up to 35 mm when fully grown). These fish can be inbred, allowing to produce large numbers of fish that feature almost identical DNA[3]. This makes them interesting for the correlation of DNA with morphological features. The fishes (especially the young ones) feature quite low contrast in absorption CT. Therefore, a staining, to enhance the contrast was introduced.

Requirements

Adjustable tube spectrum, movable source and detector (to scan multiple samples without user-intervention)

Collaboration

KIT Institute of Biological and Chemical Systems, Biological Information Processing, Centre for Organismal Studies University of Heidelberg

Results

With the use of the laboratory the staining method could be optimized to prepare measurement campaigns at the synchrotron where hundreds of medaka where scanned with the here optimized method. The results enabled the studies in [Bre21]. In figure 6.8 it is demonstrated, that these experiments can also be carried out completely in the laboratory. However, resulting in much longer scanning times (approximately 16 h per specimen, compared with 15 min at the synchrotron).

[3] Animal husbandry and experimental procedures were performed in accordance with EU directive 2010/63/EU guidelines as well as with German animal protection regulations (Tierschutzgesetz §11, Abs. 1, no. 1; Regierungspräsidium Karlsruhe, Germany; husbandry permits AZ35-9185.64/BH KIT). The facility is under the supervision of the Regierungspräsidium Karlsruhe, who approved the experimental procedures.

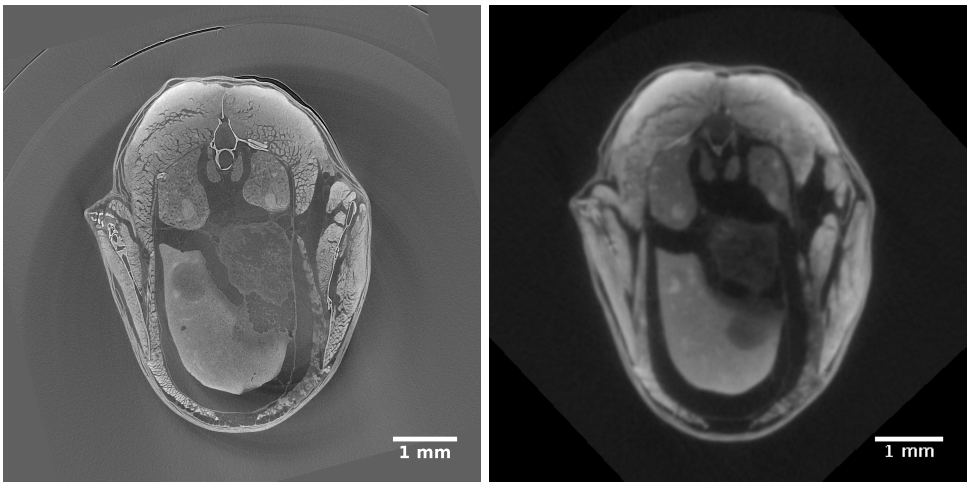

Figure 6.7.: CT slice of a stained medaka. Left: Measured at the synchrotron, right: measured at the laboratory setup with low resolution to visualize the contrast formation. In figure 6.8 a high resolution scan of a medaka in the laboratory is shown.

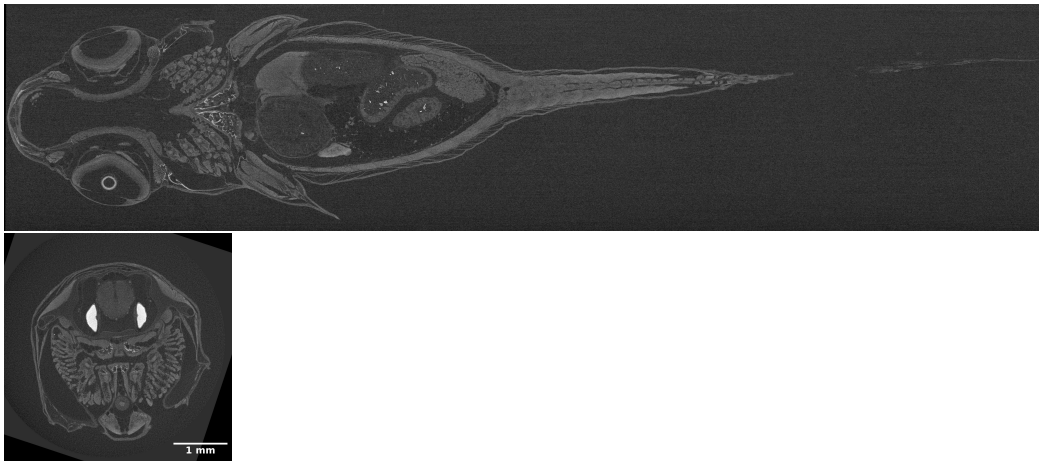

Figure 6.8.: CT slices of a stained medaka, scanned in the laboratory with high resolution.

6.3. Cultural Heritage

Collaboration

Staatliche Schlösser und Gärten Baden-Württemberg

Sample description

The Necessaire consists of wood and metal fittings. The approximate size is 45 cm × 25 cm × 30 cm (width, height, depth). For the scan, the items, that are usually stored within where removed.

Summary

A large wooden Necessaire, produced around 1820, that features many hidden compartments was examined. Since a restoration in 2005 it was assumed, that an additional hidden compartment was present, but no opening mechanism could be found. The aim was to understand this mechanism with the use of X-ray radiography and tomography. A large sample size and a comparable high spatial resolution was required. To fulfill both requirements multiple CT scans were needed and were stitched together afterwards. In total six scans where performed.

Requirements

Large field of view, high energy (due to the presence of metal parts), movable detector (for stitching).

Experiment description

The detector was shifted horizontally to different positions to enlarge the width of the field of view. This was done at two positions (−20 cm and 20 cm). The projections where stitched afterwards. In addition, the whole scan was performed at three different height positions, also extending the height of the field of view.

The distance between source and sample was set to 1316 mm and the detector was placed 1710 mm away from the source. The detectors native pixel pitch was 200 µm (PerkinElmer XRD 1621 CN14 ES), resulting in an effective magnified pixel size of 151 µm.

Each stitched projection (of the three different height scans) resulted in an image with 3048 × 2048 pixels. In total 4096 projections, equally distributed over 360° where measured.

After stitching the three reconstructed volumes and cropping the images to the dimensions of the sample, the total volume resulted in 2293 × 1608 × 3426 voxels.

The scan was optimized to show the metal parts. Therefore, beam hardening artefacts are visible, when looking on the wooden structure, since the gray levels of the wood parts are much smaller than the metal parts.

Results

With the resulting large CT datasets and some additional projections an unknown hidden compartment was discovered and the corresponding opening mechanism was understood. In the now accessible compartment even a marking of the manufacturer and the exact manufacturer date was noted. In figure 6.9 volume renderings of the sample are shown. The resulting insights are published in [Rie+19].

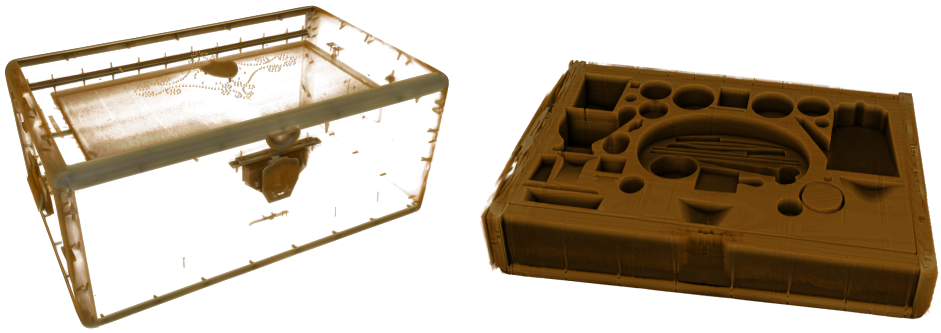

Figure 6.9.: Volume renderings of the specimen. Left: adjusted attenuation values to illustrate the metal parts. Right: Adjusted attenuation values range to illustrate the wooden inner structure.

6.4. Food Processing

Summary

Drying of fruits and vegetables is a common method for preservation. Many methods are existing with different level of complexity (and costs) that yield results with different quality. In these experiments samples of apples, strawberries and carrots were dried with different methods (freeze-drying, hot-air drying and microwave-vacuum drying) for different periods to evaluate these methods. Since the drying processes where stopped at certain drying times, it was required that the samples could be kept in an environment, that does not change the samples state during the measurements. Sample containers, that featured cooling, could be integrated onto the sample stage of the laboratory. Many experiments were carried out to evaluate different drying processes and their combinations.

Collaboration

KIT Institute of Process Engineering in Life Sciences Section I: Food Process Engineering

Requirements

Adoptable CT scans, modular sample environments

Experimental description

Standard CT scans with an effective pixel size of 14 µm where carried out. This magnification was selected to match the required scanning times, field of view and required resolution. Depending on the drying method a special sample environment was introduced on top of the sample stage (e.g. with dry ice for the cooling of the sample).

Results

With these experiments the complete 3D structure of apples, strawberry and carrot discs at different states of the drying process could be determined. A CT slice of a partially dried apple is shown in figure 6.10. Out of the 3D structure the time-dependent drying front, the wall (or crust) thickness and other parameters like

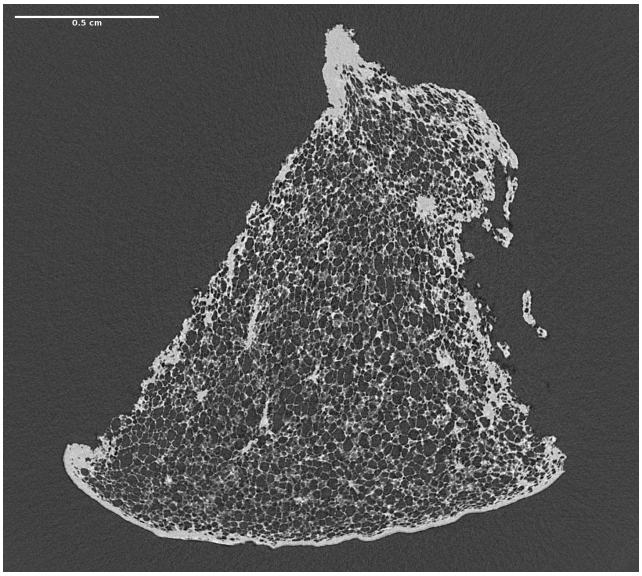

Figure 6.10.: CT slice of a dried apple slice. It can be observed, that some cells are already dried and some are still water-filled.

.

porosity and shrinkage could be extracted. With these results from the CT scans ideal combinations of drying techniques could be derived, allowing combinations of drying techniques that are easier, cheaper but resulting in similar results.

The results are published in [Sie+20; Sie+19a; Sie+19b] and also resulted in an operando/in situ freeze-drying experiment using synchrotron radiation [SZ19].

6.5. Rheology of Cement Paste

Summary

Cement is the main building material but also contributing strongly to greenhouse gases. Therefore, a reduction of the amount of used cement can have a great environmental impact. By a deeper understanding of the material properties and here especially the formation of air bubbles and the possible venting of them can lead to an optimized use of this material. In cement paste the air bubble distribution and their travel path, when exiting, has a strong influence on the resulting stability of the resulting cement part. Therefore, a sample environment, that can hold liquid cement paste and can introduce air bubbles with a defined volume was constructed and included in the laboratory setup.

Requirements

Modular sample environments, simple possibility to include sample environment control into the laboratory control system

Experimental description

The setup was optimized for high flux, energy and high frame rates. Therefore, the X-ray tube was operated at the highest possible energy and power (220 kV and

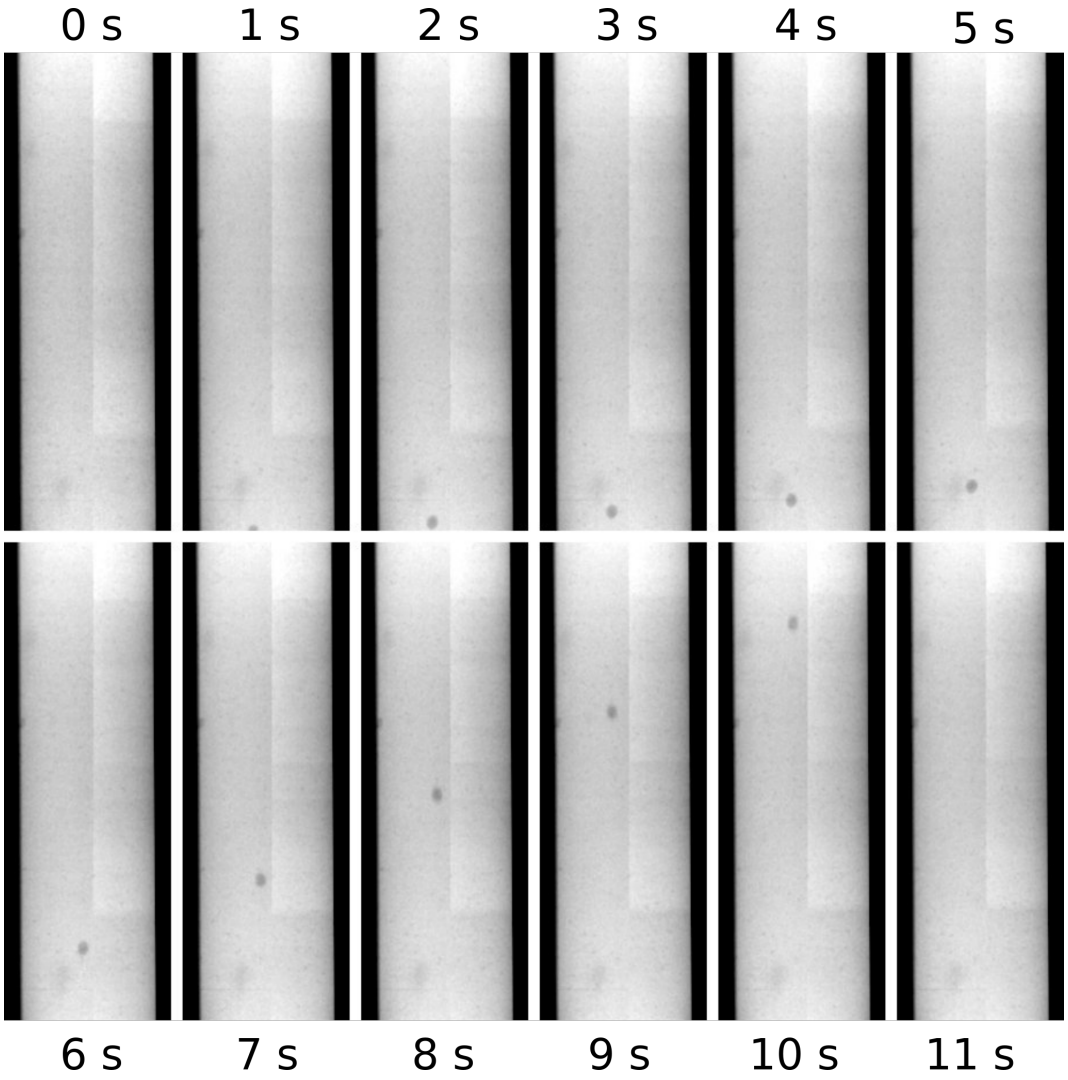

Figure 6.11.: Fast radiography of cement paste with a traveling air bubble. One of 30 frames is shown (with a spacing of 1 s)

250 W). The X-ray detector (PerkinElmer XRD 1621 CN14 ES) was operated with 30 Hz frame rate. To achieve the high frame rate, the detector pixels were binned 2×2 to a pixel size of 400 µm.

Collaboration

Karlsruhe Institute of Technology, Institute for Concrete Structures and Building Materials

Results

It was possible to track the motion of air bubbles in cement paste with 30 Hz in a projection geometry. The understanding of the bubble motion can be included in optimization of material properties of the cement paste. A projection images (recorded with 30 Hz) are shown in figure 6.11.

6.6. Characterization of X-Ray Optics (Gratings)

The size of X-ray gratings is currently limited to approximately 10 cm. By two methods, developed at the IMT at KIT, the size of the gratings can be increased. In the first method a special LIGA process [Sai+08] is employed to increase the size of the grating[Sch+17a]. In the second method, a large grating is composed of several smaller gratings, that are aligned with each other[Sch+17a]. With the unique features of the CL/CT-Laboratory I was able to implement the new grating types in the existing Talbot-Lau interferometer setup to perform detailed characterizations of the performance of the gratings. The prototype gratings produced by these methods where characterized with the laboratory setup.

Requirements

Modular optic modules, modular (and extendable) control system

Summary

The flexibility of the grating mounts allowed it to examine the quality of different types of gratings for grating based phase contrast as well as to test new grating concepts like tiled gratings and large gratings done by dynamic exposure. These experiments were carried out in collaboration with the IMT. For normal characterizations of the well established gratings on 10 cm wafers, the implemented grating based phase contrast projection experiment script could be used, directly yielding the visibility distribution of the grating. This was used to examine the quality of different grating types in [Tri+15].

Results

For larger gratings special holders could be added to the optical holders. With these larger gratings could be used and characterized. IMT was able to produce a 4x4 tiled analyzer grating (resulting in 200 mm in width and height) and a 2x2 phase grating. The resulting grating characterizations and comparisons to other grating types were published in [Sch+17b]. A phase contrast radiograph of a full bell pepper with this grating type is shown in 6.13 demonstrating the possibility to employ such a grating in the laboratory setup. This is one of the largest grating ever employed, resulting in a large grating interferometry image acquired without stitching of the sample. The different experiments allowed a deeper examination of the quality of the single gratings as well as the alignment of the sub-gratings with respect to each other.

The visible Moiré pattern is due to slight misalignment between the different tiles and mechanical instabilities of the large grating. The second can be optimized, but was not in the scope of these tests.

Another possibility for the production of larger gratings is dynamic exposure. This results in a long but not wider grating. Exemplary images of a text marker are shown in figure 6.12 to demonstrate the size and image quality with the three contrasts of grating interferometry. The production process and the characterization is shown in [Sch+17a]. These gratings where not stitched, but featured a large field of view and high magnification, but can only feature one dimensional structures.

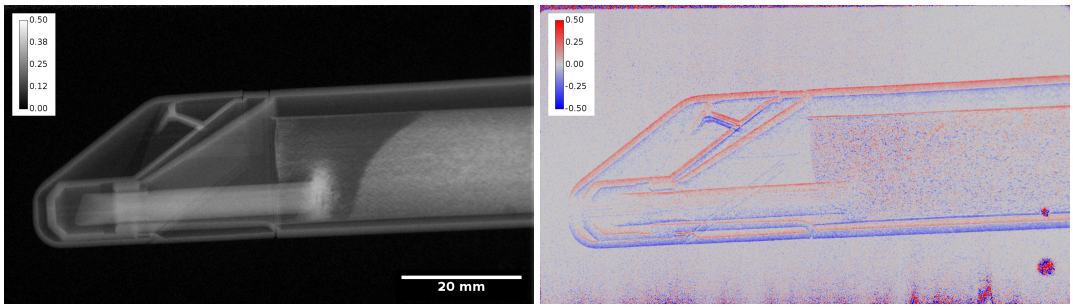

(a) Absorption contrast $-\log \mathrm{I}/\mathrm{I}_0$.

(b) Differential phase. Units in π.

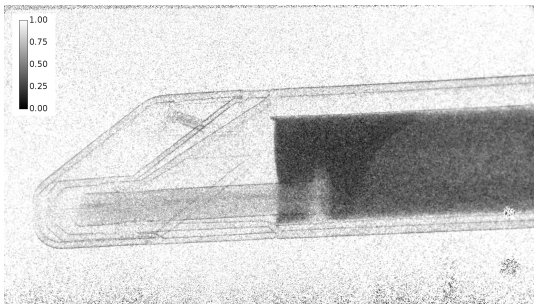

(c) Visibility contrast $\mathrm{Vis}/\mathrm{Vis}_0$.

Figure 6.12.: Grating based phase contrast projection of a text marker in high magnification and large field of view to demonstrate a dynamical exposed grating. The implemented grating interferometry setup allowed to measure the quality of the grating prototypes.

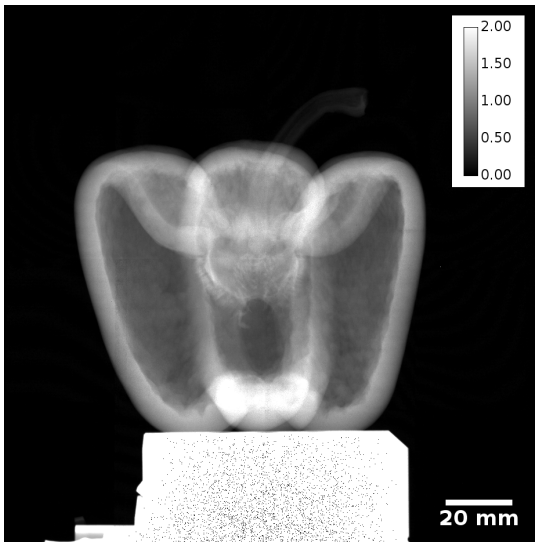

(a) Absorption contrast $-\log \mathrm{I}/\mathrm{I}_0$.

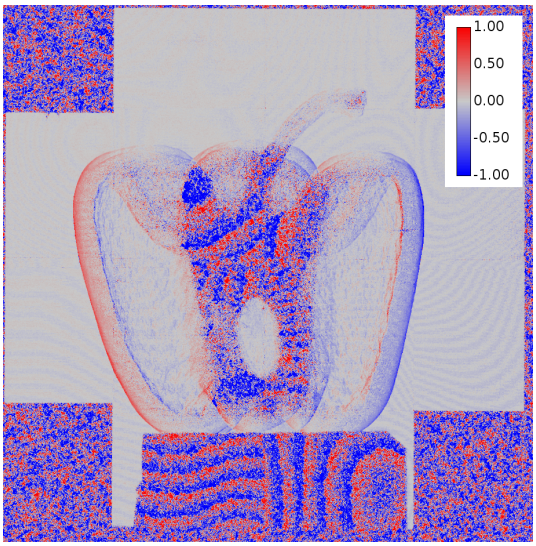

(b) Differential phase. Units in π.

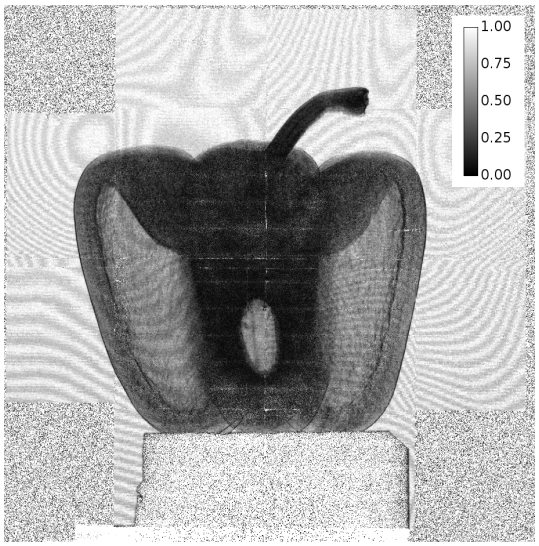

(c) Visibility contrast $\mathrm{Vis}/\mathrm{Vis}_0$.

Figure 6.13.: Grating based phase contrast projection of a bell pepper to demonstrate a stitched grating. The fringes are due to mechanical instabilities and displacements within the gratings. The examinations lead allowed to examine the quality of the sub-gratings as well as their alignment with respect to each other.

7. Conclusions and Outlook

Within this work I successfully commissioned the new X-ray imaging laboratory at the Institute for Photon Science and Synchrotron Radiation (CL/CT-Laboratory).

The laboratory implementation was done in a flexible and modular way in hard and software, allowing to easily exchange sources, detectors and include new components in the control system. The control system has been chosen to be open source, allowing collaboration partners to adapt interfaces if detectors or other components (like sample environment control etc.) is needed to be included in the control system. The laboratory is designed to be as broad in its parameter space as possible, allowing to test and verify different components and methods.

Spectroscopic X-ray imaging detectors from the Medipix family where characterized with a focus on the applicability in spectroscopic X-ray imaging. These detectors are complex systems and can be optimized in many ways. The characterizations of the different aspects can be used to optimize the performance of the detectors for a specific task. The employed detectors are under a constant development, giving a good insight in the theoretical possibilities of this technology, but are still limited in stability, size and availability. They can mostly be employed in highly specialized applications and the future applications are promising. Many findings in this work also contributed to the development of the next detector generation.

I discussed the image formation from the X-ray physics and the detector part including the wave properties of the X-rays and the resulting phase contrast and interference. For X-ray grating interferometry the influences of different imaging system components onto the contrast formation where examined. It was shown, that the common contrasts are not only a function of the specimen, but are highly dependent on characteristics of the imaging system like detector resolution and source size. This makes it challenging to compare results generated in different laboratories.

After a short introduction in the projection based imaging I describe established methods for 3D imaging and implemented them in the CL/CT-Laboratory. Starting from those, I use the unique features from the system to develop a new method (augmented laminography) combining advantages of from existing methods (computed tomography and computed laminography).

With the use of the spectroscopic photon counting detectors I implemented a method for material specific computed tomography. This method can be employed to get material specific images of samples featuring different contrast agents.

By the means of multiple application examples I demonstrate that the unique features of the CL/CT-Laboratory can be used in multiple scientific fields. This demonstrates, how the CL/CT-Laboratory has been successfully established within this work to be a fully functional imaging system enabling characterizations of X-ray imaging components, the development of new methods and to apply these methods.

Outlook: The spectroscopic single photon counting detectors are showing a strong potential for X-ray imaging. The upcoming developments in this field could enable many new application possibilities with these detectors.

Within this work I discovered grating interferometry to be highly dependent on spatial resolution. Further analysis, that could be carried out within the framework of the CL/CT-Laboratory could allow developing new imaging methods, that could take the systems parameters in account that the results are more comparable between different imaging modalities.

Bibliography

[Gra73] J. E. Gray. "XXII.—Notes on Chinese Mud-Tortoises (Trionychidæ), with the descripton of a new species sent to the British Museum by Mr. Swinhoe, and observations on the male organ of this family". In: *Journal of Natural History* 12.68 (1873), pp. 156–161.

[Rön95] W. C. Röntgen. "Über eine neue Art von Strahlen. Vorläufige Mittheilung". In: *Sonderabdruck aus den Sitzungsberichten der Würzburger Physik.-medic. Gesellschaft 1895* (1895).

[Gra72] D. G. Grant. "TOMOSYNTHESIS: A Three-Dimensional Radiographic Imaging Technique". In: *IEEE Transactions on Biomedical Engineering* BME-19.1 (Jan. 1972), pp. 20–28.

[Bla82] J. S. Blakemore. "Semiconducting and other major properties of gallium arsenide". In: *Journal of Applied Physics* 53.10 (1982), R123–R181.

[FDK84] L. A. Feldkamp, L. C. Davis, and J. W. Kress. "Practical cone-beam algorithm". In: *Journal of the Optical Society of America A* 1.6 (June 1, 1984), p. 612.

[Far92] B. L. Farkas. "Wiederentdeckung eines Exemplars von Rafetus swinhoei (Gray, 1873) im Naturhistorischen Museum Wien". In: *Salamandra (Frankfurt am Main)* 28.2 (1992), pp. 145–152.

[Boo94] J. M. Boone. "An analytical edge spread function model for computer fitting and subsequent calculation of the LSF and MTF". In: *Med. Phys.* 21.10 (1994), p. 1541.

[Sul97] T. J. Suleski. "Generation of Lohmann images from binary-phase Talbot array illuminators". In: *Applied optics* 36.20 (1997), pp. 4686–4691.

[KS01] A. C. Kak and M. Slaney. *Principles of Computerized Tomographic Imaging*. Society for Industrial Mathematics, 2001.

[Pag+02] D. Paganin, S. C. Mayo, T. E. Gureyev, P. R. Miller, and S. W. Wilkins. "Simultaneous phase and amplitude extraction from a single defocused image of a homogeneous object". In: *Journal of Microscopy* 206.1 (2002), pp. 33–40.

[SB02] W. Schlegel and J. Bille. *Medizinische Strahlenphysik*. Berlin ; Heidelberg: Springer, 2002. XXII, 548 S.

[Mom+03] A. Momose, S. Kawamoto, I. Koyama, Y. Hamaishi, K. Takai, and Y. Suzuki. "Demonstration of X-Ray Talbot Interferometry". In: *Japanese Journal of Applied Physics* 42.7B (July 2003), p. L866.

[KRW04] I. Kawrakow, D. W. O. Rogers, and B. R. B. Walters. "Large efficiency improvements in BEAMnrc using directional bremsstrahlung splitting". In: *Med. Phys.* 31 (2004), p. 2883.

[Hel+05] L. Helfen, T. Baumbach, P. Mikulík, D. Kiel, P. Pernot, P. Cloetens, and J. Baruchel. "High-resolution three-dimensional imaging of flat objects by synchrotron-radiation computed laminography". In: *Appl. Phys. Lett.* 86.7 (Feb. 2005), p. 071915.

[Jäh05] B. Jähne. *Digital image processing*. 6. rev. and extended ed. Berlin; Heidelberg; New York: Springer, 2005. XIII, 607 S.

[LKJ05] A. W. Lohmann, H. Knuppertz, and J. Jahns. "Fractional Montgomery effect: a self-imaging phenomenon". In: *JOSA A* 22.8 (2005), pp. 1500–1508.

[Mic+06] T. Michel, G. Anton, M. Böhnel, J. Durst, M. Firsching, A. Korn, B. Kreisler, A. Loehr, F. Nachtrab, and D. Niederlöhner. "A fundamental method to determine the signal-to-noise ratio (SNR) and detective quantum efficiency (DQE) for a photon counting pixel detector". In: *Nucl. Instr. and Meth. A* 568.2 (2006), pp. 799–802.

[Pag06] D. Paganin. *Coherent X-Ray Optics*. Oxford University Press, Jan. 2006.

[Spi06] H. Spieler. *Semiconductor Detector Systems*. Oxford University Press, 2006.

[Bal+07] R. Ballabriga, M. Campbell, E. H. M. Heijne, X. Llopart, and L. Tlustos. "The Medipix3 prototype, a pixel readout chip working in single photon counting mode with improved spectrometric performance". In: vol. 6. 2007, pp. 3557–3561.

[DAM07] J. Durst, G. Anton, and T. Michel. "Discriminator threshold dependency of the zero-frequency DQE of photon-counting pixel detectors". In: *Nucl. Instr. and Meth. A* 576.1 (June 11, 2007), pp. 235–238.

[Llo+07] X. Llopart, R. Ballabriga, M. Campbell, L. Tlustos, and W. Wong. "Timepix, a 65k programmable pixel readout chip for arrival time, energy and/or photon counting measurements". In: *Nucl. Instr. and Meth. A* 581.1 (2007), pp. 485–494.

[Sai+08] V. Saile, U. Wallrabe, O. Tabata, and J. G. Korvink, eds. *LIGA and its Applications*. en. Advanced Micro and Nanosystems. Weinheim, Germany: Wiley-VCH Verlag, Nov. 2008.

[But+09] A. Butler, N. Anderson, M. Hurrell, N. Cook, N. Scott, and P. Butler. "Multiple contrast agent imaging using MARS-CT, a spectroscopic (multi-energy) photon counting microCT scanner". In: *Proc. RSNA* 29 (2009).

[HTF09] T. Hastie, R. Tibshirani, and J. Friedman. *The Elements of Statistical Learning: Data Mining, Inference, and Prediction, Second Edition*. 2nd ed. 2009. Corr. 3rd printing 5th Printing. Springer, Feb. 9, 2009. 768 pp.

[KH09] A. Kirsch and F. Hettlich. "The mathematical theory of Maxwell's equations". In: *Lecture notes* (2009).

[PST09] S. Preibisch, S. Saalfeld, and P. Tomancak. "Globally optimal stitching of tiled 3D microscopic image acquisitions". In: *Bioinformatics* 25.11 (2009), pp. 1463–1465.

[AM11] J. Als-Nielsen and D. McMorrow. *Elements of Modern X-ray Physics*. Wiley, Mar. 2011.

[Koe+11a] T. Koenig, M. Zuber, A. Zwerger, P. Schuenke, S. Nill, A. Fauler, M. Fiederle, and U. Oelfke. "A comparison of various strategies to equalize the lower energy thresholds of a CdTe Medipix2 hexa detector for X-ray imaging applications". In: *J. Inst.* 6.1 (Jan. 2011), p. C01074.

[Koe+11b] T. Koenig, A. Zwerger, M. Zuber, P. Schuenke, S. Nill, E. Guni, A. Fauler, M. Fiederle, and U. Oelfke. "On the energy response function of a CdTe Medipix2 Hexa detector". In: *Nucl. Instr. and Meth. A* 648, Supplement 1 (Aug. 21, 2011), S265–S268.

[Kon+12] A. C. Konstantinidis, M. B. Szafraniec, R. D. Speller, and A. Olivo. "The Dexela 2923 CMOS X-ray detector: A flat panel detector based on CMOS active pixel sensors for medical imaging applications". In: *Nuclear Instruments and Methods in Physics Research Section A: Accelerators, Spectrometers, Detectors and Associated Equipment* 689 (2012), pp. 12–21.

[Bal+13] R. Ballabriga, J. Alozy, G. Blaj, M. Campbell, M. Fiederle, E. Frojdh, E. H. M. Heijne, X. Llopart, M. Pichotka, S. Procz, L. Tlustos, and W. Wong. "The Medipix3RX: a high resolution, zero dead-time pixel detector readout chip allowing spectroscopic imaging". In: *J. Inst.* 8.2 (Feb. 1, 2013), p. C02016.

[Pro+13] S. Procz, K.-A. Wartig, A. Fauler, A. Zwerger, J. Luebke, R. Ballabriga, G. Blaj, M. Campbell, M. Mix, and M. Fiederle. "Medipix3 CT for material sciences". In: *Journal of Instrumentation* 8.01 (2013), p. C01025.

[Fro+14] E. Frojdh, R. Ballabriga, M. Campbell, M. Fiederle, E. Hamann, T. Koenig, X. Llopart, D. d. P. Magalhaes, and M. Zuber. "Count rate linearity and spectral response of the Medipix3RX chip coupled to a 300 µm silicon sensor under high flux conditions". In: *J. Inst.* 9.4 (Apr. 22, 2014), pp. C04028–C04028.

[Ham+14] E. Hamann, T. Koenig, M. Zuber, A. Cecilia, A. Tyazhev, O. Tolbanov, S. Procz, A. Fauler, T. Baumbach, and M. Fiederle. "Performance of a Medipix3RX Spectroscopic Pixel Detector with a High Resistivity Gallium Arsenide Sensor". In: *IEEE Trans. Med. Imag.* PP.99 (2014), pp. 1–1.

[Koe+14a] T. Koenig, M. Zuber, E. Hamann, A. Cecilia, R. Ballabriga, M. Campbell, M. Ruat, L. Tlustos, A. Fauler, M. Fiederle, and T. Baumbach. "How spectroscopic x-ray imaging benefits from inter-pixel communication". In: *Phys. Med. Biol.* 59.20 (Oct. 21, 2014), p. 6195.

[Koe+14b] T. Koenig, M. Zuber, E. Hamann, A. Runz, M. Fiederle, and T. Baumbach. "Pooling optimal combinations of energy thresholds in spectroscopic CT". In: *SPIE Medical Imaging*. Vol. 9033. 2014, 90331A–90331A–12.

[Poi+14] T. Poikela, J. Plosila, T. Westerlund, M. Campbell, M. D. Gaspari, X. Llopart, V. Gromov, R. Kluit, M. van Beuzekom, F. Zappon, V. Zivkovic, C. Brezina, K. Desch, Y. Fu, and A. Kruth. "Timepix3: a 65K channel hybrid pixel readout chip with simultaneous ToA/ToT and sparse readout". In: *Journal of Instrumentation* 9.05 (May 2014), p. C05013.

[Zub+14] M. Zuber, T. Koenig, E. Hamann, A. Cecilia, M. Fiederle, and T. Baumbach. "Characterization of a 2x3 Timepix assembly with a 500 µm thick silicon sensor". In: *J. Inst.* 9.5 (2014), p. C05037.

[Ham+15] E. Hamann, T. Koenig, M. Zuber, A. Cecilia, A. Tyazhev, O. Tolbanov, S. Procz, A. Fauler, M. Fiederle, and T. Baumbach. "Investigation of GaAs: Cr Timepix assemblies under high flux irradiation". In: *J. Inst.* 10.1 (2015), p. C01047.

[HS15] J. H. Hubbell and S. M. Seltzer. "Tables of X-Ray Mass Attenuation Coefficients and Mass Energy-Absorption Coefficients". In: (2015).

[Tri+15] B. Trimborn, P. Meyer, D. Kunka, M. Zuber, F. Albrecht, S. Kreuer, T. Volk, T. Baumbach, and T. Koenig. "Imaging properties of high aspect ratio absorption gratings for use in preclinical x-ray grating interferometry". In: *Physics in Medicine & Biology* 61.2 (2015), p. 527.

[Zub+15] M. Zuber, E. Hamann, R. Ballabriga, M. Campbell, M. Fiederle, T. Baumbach, and T. Koenig. "An investigation into the temporal stability of CdTe-based photon counting detectors during spectral micro-CT acquisitions". In: *Biomedical Physics & Engineering Express* 1.2 (2015), p. 025205.

[Bal+16] R. Ballabriga, J. Alozy, M. Campbell, E. Frojdh, E. Heijne, T. Koenig, X. Llopart, J. Marchal, D. Pennicard, T. Poikela, L. Tlustos, P. Valerio, W. Wong, and M. Zuber. "Review of hybrid pixel detector readout ASICs for spectroscopic X-ray imaging". In: *Journal of Instrumentation* 11.01 (2016), P01007.

[Bir+16] L. Birnbacher, M. Willner, A. Velroyen, M. Marschner, A. Hipp, J. Meiser, F. Koch, T. Schröter, D. Kunka, J. Mohr, et al. "Experimental realisation of high-sensitivity laboratory X-ray grating-based phase-contrast computed tomography". In: *Scientific reports* 6 (2016), p. 24022.

[Koe+16] T. Koenig, M. Zuber, B. Trimborn, T. Farago, P. Meyer, D. Kunka, F. Albrecht, S. Kreuer, T. Volk, M. Fiederle, et al. "On the origin and nature of the grating interferometric dark-field contrast obtained with low-brilliance x-ray sources". In: *Physics in medicine and biology* 61.9 (2016), p. 3427.

[Sch+17a] T. J. Schröter, F. Koch, P. Meyer, M. Baumann, D. Münch, D. Kunka, S. Engelhardt, M. Zuber, T. Baumbach, and J. Mohr. "Large area gratings by x-ray LIGA dynamic exposure for x-ray phase-contrast imaging". In: *Journal of Micro/Nanolithography, MEMS, and MOEMS* 16.1 (2017), p. 013501.

[Sch+17b] T. J. Schröter, F. J. Koch, D. Kunka, P. Meyer, S. Tietze, S. Engelhardt, M. Zuber, T. Baumbach, K. Willer, L. Birnbacher, et al. "Large-area full field x-ray differential phase-contrast imaging using 2D tiled gratings". In: *Journal of Physics D: Applied Physics* 50.22 (2017), p. 225401.

[Zub+17] M. Zuber, M. Laaß, E. Hamann, S. Kretschmer, N. Hauschke, T. Van De Kamp, T. Baumbach, and T. Koenig. "Augmented laminography, a correlative 3D imaging method for revealing the inner structure of compressed fossils". In: *Scientific reports* 7.1 (2017), pp. 1–11.

[Hir+18] R. Hirayama, S. Kuratani, A. Takahashi, Y. Nakajima, T. Sonoda, Y. Nishioka, and M. Yoshida. "Turtle Evolution Symposium 2018 Japan". en. In: (2018).

[Man19] R. Mandel. *Nonlinear Helmholtz Equations and Systems*. 2019.

[Rie+19] K. Riemann, D. Hänschke, M. Zuber, and E. Hamann. "Mit Röntgenblick auf Geheimnissuche". In: *Schlösser Baden-Württemberg* 03/2019 (2019), pp. 28–30.

[SZ19] T. Siebert and M. Zuber. "In-situ micro-CT scan of a carrot disc during freeze-drying". In: (2019).

[Sie+19a] T. Siebert, M. Zuber, S. Engelhardt, T. Baumbach, H. P. Karbstein, and V. Gaukel. "Visualization of crust formation during hot-air-drying via micro-CT". In: *Drying Technology* 37.15 (2019), pp. 1881–1890.

[Sie+19b] T. Siebert, M. Zuber, E. Hamann, T. Baumbach, H. P. Karbstein, and V. Gaukel. "Micro-CT visualization of structure development during freeze-drying processes". In: *Drying Technology* (2019).

[DPS20] M. Danielsson, M. Persson, and M. Sjölin. "Photon-counting x-ray detectors for CT". In: *Physics in Medicine & Biology* (2020).

[Pog+20] P. Pogoda, M. Zuber, T. Baumbach, R. R. Schoch, and A. Kupfer. "Cranial shape evolution of extant and fossil crocodile newts and its relation to reproduction and ecology". In: *Journal of Anatomy* (2020).

[Sie+20] T. Siebert, A. Becker, M. Bunzel, M. Zuber, E. Hamann, T. Baumbach, H. P. Karbstein, and V. Gaukel. "Evaluation of the usefulness of serial combination processes for drying of apples". In: *Drying Technology* 38.10 (2020), pp. 1274–1290.

[Acr21] L. Acrorad Co. *Comparison of Typical Semiconductor Detector*. 2021. URL: `https://www.acrorad.co.jp/index_en/products_en/technology/basic.html` (visited on 08/24/2021).

[Bre21] S. U. Bremer. "High-throughput 3D x-ray imaging of small vertebrate model organisms on the example of medaka". en. In: (2021).

[Pog+21] P. Pogoda, M. Zuber, T. Baumbach, and A. Kupfer. "Clasp and dance: Mating mode promotes variable sexual size and shape dimorphism trajectories in crocodile newts (Caudata: Salamandridae)". In: *Authorea Preprints* (2021).

[Far+22] T. Faragó, S. Gasilov, I. Emslie, M. Zuber, L. Helfen, M. Vogelgesang, and T. Baumbach. "Tofu: a fast, versatile and user-friendly image processing toolkit for computed tomography". In: *Journal of Synchrotron Radiation* 29.3 (2022).

[Llo+22] X. Llopart, J. Alozy, R. Ballabriga, M. Campbell, R. Casanova, V. Gromov, E. Heijne, T. Poikela, E. Santin, V. Sriskaran, L. Tlustos, and A. Vitkovskiy. "Timepix4, a large area pixel detector readout chip which can be tiled on 4 sides providing sub-200 ps timestamp binning". In: *Journal of Instrumentation* 17.01 (Jan. 2022), p. C01044.

[XXLCT] *Hochenergie- oder XXL-Computertomographie*. URL: `https://www.iis.fraunhofer.de/de/ff/zfp/tech/hochenergie-computertomographie.html` (visited on 11/03/2020).

[SKY] *SKYSCAN 1272*. URL: `https://www.bruker.com/products/microtomography/micro-ct-for-sample-scanning/skyscan-1272/overview.html` (visited on 11/03/2020).

[US] N. US Department of Commerce. *NIST: X-Ray Mass Attenuation Coefficients*. NIST: X-Ray Mass Attenuation Coefficients. URL: `http://www.nist.gov/pml/data/xraycoef/index.cfm` (visited on 09/02/2012).

A. Acknowledgmenets

This whole work was supported by the help of many people. First, I would like to thank my supervisor, Prof. Dr. Tilo Baumbach, for his support during my work. I would also like to thank my co-supervison, Prof. Dr. Michael Fiederle, for his support and the possibility to work with all the different detector systems.

The planing and setup of the laboratory was supported by many of the IPSs imaging group members, especially Thomas König, Elias Hamann, Tomy dos Santos Rolo, Sabine Bremer, Barbara Trimborn, Tomáš Faragó, Daniel Hänschke, Lukas Helfen and Jochen Butzer.

Thomas van de Kamp helped me with many suggestions and also established so many fruitfully collaborations with biologists and paleontologists.

Thomas König was one my greatest supporters and was always a great source of inspiration.

The whole IPS imaging and scattering group was always very helpful and supportive.

Many discussions within the Medipix group, especially with Rafael Ballabriga, were very helpful.

I would like to thank the MARS Bioimaging group, especially Phil Butler and Anthony Butler, for the provision of the CZT based Medipix3RX detector.

Also, I would like to thank all the people in the many collaborations for carrying out so many interesting experiments together and giving me the insights into their scientific field.

Finally, I would like to thank my complete family, especially my wife and my kids, for their support during my work.